# Septins Enable T Cells Adaptive Circumnavigation and Migration-Transmigration Transition Within Structurally Complex Microenvironments

Alexander S. Zhovmer [1,✉], Alexis Manning [1,#], Chynna Smith [2,#], Yashavantha L. Vishweshwaraiah [3], Jian Wang [3], Pablo J. Sáez [4], Xuefei Ma [1], Denis Tsygankov [5], Alexander X. Cartagena-Rivera [2], Rakesh K. Singh [6], Nikolay V. Dokholyan [3,7,✉], Erdem D. Tabdanov [3,✉]

**Affiliations:**

1. Center for Biologics Evaluation & Research, U.S. Food and Drug Administration, Silver Spring, MD, USA
2. Section on Mechanobiology, National Institute of Biomedical Imaging and Bioengineering, National Institutes of Health, Bethesda, MD, USA
3. Departments of Pharmacology, Penn State College of Medicine, Pennsylvania State University Hershey-Hummelstown, PA, USA
4. Cell Communication and Migration Laboratory, Institute of Biochemistry and Molecular Cell Biology, Center for Experimental Medicine, University Medical Center Hamburg-Eppendorff
5. Wallace H. Coulter Department of Biomedical Engineering, Georgia Institute of Technology and Emory University, Atlanta, GA, USA
6. Department of Obstetrics & Gynecology, University of Rochester Medical Center, Rochester, NY, USA
7. Department of Biochemistry & Molecular Biology, Penn State College of Medicine, Hershey, PA, USA

# - These authors contributed equally

**Running Title:** Septins Reprogram T Cell Mechanobiology

✉ - **Correspondence authors:**

Alexander S. Zhovmer, Tel: 1-301-402-1606: alexander.zhovmer@fda.hhs.gov
Nikolay V. Dokholyan, dokh@psu.edu
**(Lead contact):**
Erdem D. Tabdanov, Tel: 1-717-531-0003 Ext: 4430: ekt5171@psu.edu

## AUTHORS CONTRIBUTIONS

E.D.T. and A.S.Z. conceived the project. E.D.T. formulated and theoretically conceptualized the problem, E.D.T. coordinated the project. E.D.T. and A.S.Z. developed the experimental framework of this study, A.M., A.S.Z. and E.D.T. carried out the principal mechanobiology, cell biology, and microscopy studies. R.K.S. designed, synthesized, purified, chemically tested and verified mammalian septins inhibitor UR214-9. N.V.D., J.W. and Y.V. performed *in silico* modeling of septin molecular dynamics and UR214-9 docking to the key mammalian septin isoforms. Y.V. made practical contributions to the biochemical studies. E.D.T. and A.S.Z. designed and microfabricated mechanobiological platforms. A.M., C.S., and A.X.C.R. made a practical contribution with live T cell AFM analysis. E.D.T., A.S.Z., A.M., C.S., Y.V., X.M., and A.X.C.R. performed experimental data analysis and interpretation. P.J.S. and D.T. conducted an automated visual data processing and interpretation, image deconvolution, quantification, and wrote scripts to analyze cell migration. E.D.T. and A.S.Z. wrote and edited all versions of the manuscript. All authors read and contributed comments to the final manuscript. E.D.T. oversaw all aspects of this study.

## ABSTRACT

T cell all-terrain migration through healthy, inflamed or diseased tissues results from the dynamic balance between various migration modes. Here we report that septins mechanobiologically coordinate and balance amoeboid *vs.* mesenchymal-like migratory modes in T cells. Specifically, septins enable the assembly of circumferential cortical F-actin rings at the sites of cortex-indenting collisions with the extracellular matrix (ECM). Thus, septin rings compartmentalize the actomyosin cortex into a peristaltic chain of segments, spatially conformed to the ECM. Rings between adjacent spherical segments form 'hourglass'-shaped furrows that sterically lock onto cortex-indenting collagen fibers, forming fulcrums for peristaltic treadmilling cytosolic content between cell compartments. Septins' inactivation abruptly shifts T cells towards mesenchymal-like migration, characterized by the loss of amoeboid cortex compartmentalization, ineffective 3D circumnavigation, and distinct 2D contact guidance. We determine that mesenchymal-like lymphocyte migration is driven by dynein-based contractility within MAP4-, SEPT9-, HDAC6-enhanced microtubular cables for effective and structurally coherent motility and transmigration.

**Keywords:** septin, immune, migration, amoeboid, mesenchymal, mechanobiology

## GLOSSARY

1. Steric interactions - interactions by the means of their spatial collision dependent on objects' shapes.
2. Steric guidance - cell navigation within crowded 3D environments, determined by the available passages around and between steric hindrances.
3. Peristaltic treadmilling - locomotion mode by the means of a repeated sequence of polarized cell cortex extension, stabilization, and retraction, accompanied by translocation of nucleus and cytoplasm *via* circumferential cortex contractility.
4. Dynein contractility - contractile forces generated by dynein motor proteins within a system of non-stretchable, force-transmitting microtubules.

## INTRODUCTION

The mechanobiology of lymphocyte migration is a long-standing field of research since inadequate trafficking of immune cells in tissues contributes to formation of the anti-immune sanctuaries, cancer progression, and autoimmune, allergic and neurodegenerative disorders (Hammond et al., 2019; Islam and Luster, 2012; Lanitis et al., 2017; Wiendl et al., 2021). One of the focal points of mechanobiology of lymphocyte migration is the ability of immune cells to sense tissue microenvironments and adaptively remodel cytoskeleton for optimization of cell motility. Such cytoskeletal plasticity allows lymphocytes to use simultaneously or quickly alternate between a variety of migration modes (Krummel et al., 2014, 2016; Tabdanov et al., 2021). For instance, a non-adhesive amoeboid (Renkawitz and Sixt, 2010; Tooley et al., 2009) and an adhesive mesenchymal-like (Renkawitz et al., 2019; Tabdanov et al., 2021) migration modes are combined into a 'random-walk' motility (Krummel et al., 2014; Tabdanov et al., 2021). The 'random-walk' motility can be accompanied by a 3D 'paddling' in fluids (Aoun et al., 2020). The immune cells dynamically balance these migration modes as they transition across various microenvironments (Krummel et al., 2016; Renkawitz et al., 2009). For example, using GEF-H1→RhoA signaling axis, lymphocytes readjust the amoeboid and mesenchymal-like migration modes in response to the mechanical and architectural properties of the microenvironment (Tabdanov et al., 2021). Despite the significant clinical interest and multiple studies of mechanisms that control lymphocyte tissue entry and migration, *e.g.* entry and surveillance of the solid tumors or pathological invasion into the brain, it is still largely unknown how immune cells dynamically adapt their mechano-structural properties during transition across various and often extreme environments, while maintaining efficient motility and structural integrity. Specifically, little is known about lymphocytes reorganization of their major cytoskeletal components, such as actomyosin and microtubules, for optimal cell motility. Particularly, due to the extreme structural and signaling entanglement between cytoskeleton components, the following question arises: Which component generates the propulsion forces and which provides the structural integrity? This query is particularly important for surveilling lymphocytes that undergo rapid series of extreme deformations within structurally diverse, highly confining and sterically interactive tissue microenvironments.

The rapid non-adhesive propulsion of T cells in sterically interactive microenvironments, such as the 3D collagen matrix, is best described as amoeboid motility, although its mechanistic principles remain undeciphered (Wolf et al., 2003). However, it is known that amoeboid motility of T cells does not require specific biochemical or structural modifications to the surrounding collagen matrix. Instead, T cells rely on the active changing of cell shape, and steric (*i.e.* non-adhesive) interactions with collagen matrix which allows them to circumnavigate, *i.e*. steer around the collagen fibers, while finding available lumens for passage (Sadjadi et al., 2020; Wolf et al., 2003). The efficiency of amoeboid motility is proportional to the contractility of cortical actomyosin and inversely proportional to the cell-microenvironment adhesive interactions across all sterically interactive environments, such as nano-topographic surfaces, 3D collagen matrices, and cancer tumor tissue samples, (Krummel et al., 2014; Tabdanov et al., 2021; Takesono et al., 2010). To explain these experimental observations, the current model of amoeboid motility suggests that contractility of cortical actomyosin stimulates formation of cell blebs, which serve as precursors for cell extension (Charras and Paluch, 2008). Specifically, the actomyosin cortex and plasma membrane serve both as a locomotion substrate for blebs formation and as a primary generator of cytoplasmic hydrostatic pressure, which causes repeating events of destabilization and transient ruptures of binding interactions between the underlying cortex and plasma membrane (Charras et al., 2005, 2006; Fritzsche et al., 2013). However, the blebbing model does not incorporate alternative mechanisms of non-adhesive locomotion described for immune cells, *e.g.* cell sliding by the retrograde cortex treadmilling in the 'leading bleb' (Adams et al., 2018; Renkawitz et al., 2009), and the motility by the active cortical deformation (Reversat et al., 2020). Moreover, the blebbing model does not explain the spatiotemporally coordinated 3D extension of

the cell cortex required for an effective directional propulsion of immune cells within a structurally discrete microenvironment.

It is hypothesized that amoeboid T cells use elements of integrin-dependent mesenchymal-like migration to guide directional propulsion within a structurally discrete microenvironment (Krummel et al., 2016) and during transmigration (Filippi, 2016). Indeed, cascades of integrin-dependent phenotype switching events and corresponding cytoskeletal reorganizations are required for directional transmigration of immune cells between the bloodstream and organs (Ley et al., 2007; Vestweber, 2015). Multiple direct observations in a variety of immune cells amount to the conclusion that mechanobiology of transmigratory cells differs from that of amoeboid cells (Balzer et al., 2012; Carey et al., 2015; Raman et al., 2013), including the activation of distinct signaling pathways for mesenchymal-like migration (Balzer et al., 2012; Hung et al., 2013; Paul et al., 2017; Rolli et al., 2010; Stroka et al., 2014). Briefly, transitioning through the highly confining blood vessel wall is initiated by integrin-dependent adhesion and downstream intracellular signaling cascades which initiate mesenchymal-like cell spreading and lateral migration on the luminal 2D surface. The activation of mesenchymal-like cell spreading and migration by adhesion molecules, such as intercellular adhesion molecule 1 (ICAM1), relies on suppression of the actomyosin contractility. The loss of actomyosin contractility causes an overall structural and mechanical “fluidization” of cell cortex, which facilitates cell deformability for passage through the extremely confining spaces. Due to the extreme “fluidization”, transmigrating cells acquire a discrete elongated morphology, which requires currently uncharacterized rupture-resistant organization of the cytoskeleton to support structural integrity in cells passing the narrow pores. For example*,* in highly confining microchannels (3 μm-wide), migrating T cells do not depend on the actomyosin contractility, regardless of the specific adhesion to the surrounding microchannel (Krummel et al., 2014). Instead, these cells rely on the microtubule system (Balzer et al., 2012; Kopf et al., 2020). These studies demonstrate a mechanobiological plasticity of cytoskeletal organization in motile T cells that provides seamless switching between actomyosin-dependent amoeboid and microtubule-based mesenchymal-like cell migration modes upon sensing of a specific microenvironment. However, the mechanisms that coordinate mechanobiological plasticity of actomyosin and microtubule systems during migration of immune cells remain largely unknown.

Septins are GTP-binding proteins that work in conjunction with actomyosin and microtubules. Similarly to actomyosin and microtubules, septins regulate the motility of immune cells. For example, the knockdown of selected septin isoforms improves transmigration of T cells through confining pores, whereas native septins enable amoeboid motility of T lymphocytes *via* an unknown mechanism (Tooley et al., 2009). Mechanistically, septins participate in circumferential constriction of the actomyosin cell cortex, *i.e.* constriction of a contractile actomyosin ring during cytokinesis, which is considered as a possible link between septins and the amoeboid mode of T cell migration (Gilden et al., 2012; Tooley et al., 2009). Thus, septins’ GTPase activity (Spiliotis, 2018; Woods and Gladfelter, 2021) drives assembly of four major septin isoforms (*i.e.* SEPT2, SEPT6, SEPT7, and SEPT9) into non-polar filaments that are involved in the stabilization of contractile actomyosin structures, such as stress-fibers (Dolat et al., 2014; Schmidt and Nichols, 2004; Spiliotis and Nakos, 2021) or contractile cortical bands (Founounou et al., 2013; Kinoshita et al., 2002; Mostowy and Cossart, 2012). The current paradigm suggests that septins-based stabilization of actomyosin structures ensures the accumulation of substantial contractile energy (Dolat et al., 2014; Schmidt and Nichols, 2004). The contractile energy is required for dynamics of the amoeboid cortex in T cells (Gilden et al., 2012; Tooley et al., 2009) or the cortex-driven cytokinesis (Estey et al., 2010). However, septins also participate in the microtubule abscission and microtubule-driven cytokinesis (Estey et al., 2010; Kim et al., 2011). For example, septin-9’s translocation from the actomyosin-associated polymerized septin filaments, followed by its binding to microtubules, causes a suppression of microtubules plus-end instability and leads to the enhancement of the microtubular apparatus (Nakos et al., 2019). Moreover, a recently found MAP-like motif in SEPT9_i1 isoform (Kuzmić et al., 2021) suggests a dual role for septins

which act as actomyosin supporting components and as regulating factors of microtubule-associated signaling, *e.g.* by shuttling of septin-9 between actomyosin and microtubules (Kuzmić et al., 2021). Notably, a loss of septin-9 (SEPT9$^{-/-}$) leads to a partial loss of fibroblast transmigration efficiency, highlighting a possible causative link between T cell transmigration, septins activity (Füchtbauer et al., 2011), and microtubule system (Kopf and Kiermaier, 2021; Kopf et al., 2020). Similarly to septin-9, a SEPT7 isoform is reported as the MAP4 binding factor that prevents MAP4 binding to microtubules and, thus, MAP4-mediated microtubules stabilization (Kremer et al., 2005; Permana et al., 2005).

Based on these observations, we suggest that septins regulate balance of actomyosin-based amoeboid and microtubule-based mesenchymal-like migration in primary human T cells during mechanobiological sensing of microenvironment. Specifically, we demonstrate that septins are required for extracellular matrix-guided assembly of cortical F-actin rings in migrating amoeboid T cells. These rings partition the actomyosin cortex of an amoeboid T cell into peristaltically treadmilling 'ball-chain' of contractile spheroid segments. The lined-up cell segments feature 'hourglass' topography and discrete actomyosin contractility that facilitates steric interactions with obstacles and obstacle-evasive peristaltic propulsion of cytosolic content between the cell segments. Subsequently, we show that acute inhibition of septins' GTPase activity causes an abrupt loss of cell segmentation and 3D circumnavigation. Additionally, acute inhibition of septins triggers transitioning of T cells from amoeboid towards mesenchymal-like migration which is characterized by a microtubule- and dynein-based motility and distinct contact guidance. In summary, our results indicate that septins provide mechanobiological plasticity of cytoskeletal organization during amoeboid and mesenchymal-like migration of T cells, coordinating coherent cell propulsion by actomyosin- and dynein-based force producing systems. Additionally, we show that the amoeboid motility of immune cells is a non-stochastic 3D circumnavigation guided by the structure of a crowding microenvironment.

## RESULTS AND DISCUSSION

### Septin-rich F-actin rings compartmentalize actomyosin cortex in migrating T cells

Our principal observation indicates that primary human T cell (*e.g.* human CD4+ T cell, hCD4+) compartmentalizes its actomyosin cortex during amoeboid migration within 3D collagen matrices, transforming from a singular cell spheroid into a system of discrete and interconnected spheroid segments **(Figure 1a-b)**. Spheroid segments are separated by cortex-indenting circumferential furrows identified as F-actin dense cortical rings **(Figure 1a**, *F-actin, arrows***)**. The repetitive distribution of cortical rings reshapes cell cortex into a 'ball-chain'-like multi-segmented cortical tube, which visually conforms to available lumens within the surrounding collagen matrix, and constricts the translocating nucleus **(Figure 1a**, *nucleus, arrows***)**. The 'ball chain' morphology of migrating T cells, *i.e.* the lined-up cell segments separated by discrete F-actin rings **(Figure 1b)**, reminisces the septin-stabilized membranous and/or cortical rings, reported in the dividing yeasts (Oh and Bi, 2011) and some mammalian cells (Bridges and Gladfelter, 2015; Founounou et al., 2013). Notably, we identify septins as a principal component of the leading F-actin ring **(***e.g.* septin-7, **Figure 1c-d**, **+DMSO)** in migrating T cells.

The identification of septin-positive cortical F-actin rings in primary human T cells suggests a mechanism explaining previously reported correlation between septins expression (*e.g.* septin-7) and amoeboid behavior of T cells (Tooley et al., 2009). Specifically, we propose that septins cross-linking activity within the actomyosin cortex restructures the T cell into a hydrostatically unified system of the expanding, static and contracting cortical segments, which provides continuous shape-changing dynamics and amoeboid motility. Thus, we suggest that the spatiotemporally regulated cortex cross-linking governs the cortex shape and forces dynamics, that in turn drives the amoeboid cell motility. This conjecture is based on the observation of amoeboid sliding motility in non-immune melanoma cells, where an excessive cross-linking of contractile cortical F-actin (*e.g.* by filamin-A and/or fascin), combined with the cells sterical confinement,

results with cortex reorganization into a continuous system of coaxial circumferential fibers, forming an elongated cylindrical cortex of a leading bleb (Adams et al., 2021). We suggest that the reported filamin-A and/or fascin-rich circumferential cortical structures in melanoma cells and the observed discrete septin-positive cortical rings in human T cells are both analogous to the linear stress-fibers from the perspective of the actomyosin organization and condensation dynamics, yet in a circular form, locking onto themselves within the cortex, rather than onto the adhesive focal adhesions (Adams et al., 2018; Liu et al., 2015). Consequently, the sustained gradient of cross-linking density within the leading bleb's cortex generates its actomyosin contractility gradient that drives cortex' continuous treadmilling - a process that powers the friction-based cell sliding between two non-adhesive, confining parallel flat surfaces (Adams et al., 2021).

Although the described process is considered as a particular example of the wide and poorly characterized variety of amoeboid motility mechanisms, the 'cortex sliding' locomotion is based on the elevated mechanical friction between a cell and its confining microenvironment, which seems mechanically suboptimal and energetically wasteful. Moreover, the leading bleb-driven motility has only been observed within the structurally simplified artificial environments, *i.e.* - lumens between the parallel flat surfaces (Adams et al., 2018; Liu et al., 2015). Therefore, we question whether compartmentalization of T cell's actomyosin cortex into the multiple segments, separated with discrete septin rings, enables a more optimized migration mechanism inherent to immune cells. Thus, to dissect the role of septins and septin-based cortical structures during T cell morphological and migratory response to the structurally complex microenvironments we proceed to inhibit septins in T cells, migrating through the 3D collagen matrix. Indeed, acute chemical perturbation of septins in migrating hCD4+ T cells with the novel mammalian septins' GTPase activity inhibitor, UR214-9 **(+UR214-9**, 40 μM**)** (Kim et al., 2020; Zhovmer et al., 2021), results with the loss of T cell cortical rings and segmentation **(Figure 1c-d**, **+UR214-9)** and the visual arrest of T cell motility. Instead, T cells acquire a non-migratory morphology, characterized by the passive cell shape conformity to the surrounding collagen matrix in the form of multiple elongated protrusions. Notably, since the loss of T cell segmentation **(Figure 1e)** marks the transitioning between the migratory **(+DMSO)** and non-migratory phenotypes **(+UR214-9)**, we propose that the 'hourglass'-shaped cell surface formed by a cortex-indenting septin circumferential furrows (*i.e.* rings) between adjacent spheroid compartments actively participates in the amoeboid motility by creating a transient steric lock (*i.e.* non-adhesive mechanical fulcrum) between the lymphocyte and confining collagen fibers **(Figure 1e**, **+DMSO)**.

The selected strategy of acute pharmacological inhibition of septins decreases a probability of causing complex, non-linear, and poorly decipherable cumulative downstream effects as compared to available alternatives, such as long-term perturbation of septins activity by genetic knockout. The selective septin inhibitor UR214-9 is a fluoride-derived analogue of the fungal (*i.e.* yeast) septin inhibitor forchlorfenuron (FCF) (Hu et al., 2008), which provides an abrupt and detectable loss of septin-actomyosin interactions (Cheffings et al., 2016; Dolat et al., 2014; Founounou et al., 2013; Salameh et al., 2021; Schmidt and Nichols, 2004), linked to the septin-mediated amoeboid cell behavior (Gilden et al., 2012; Tooley et al., 2009). However, unlike FCF, the UR214-9 displays a negligible cytotoxicity towards mammalian cells that is suitable for the acute 'high dose-short term' cell treatments (Kim et al., 2020; Singh et al., 2020; Zhovmer et al., 2021). To test whether the UR214-9 displays competitive septin-docking energies compared to GTP, GDP and FCF at the septin molecules' GTPase sites, we first aim for an *in silico* molecular modeling for septin-inhibitor and septin-GTP/GDP docking and energy of interactions. The calculated docking energies for all docking interactions between septin molecules and GTP, GDP, UR214-9, and FCF molecules display the competitive and comparable interactions energies for all listed molecules, while UR214-9 also displays more optimal docking energies than that of FCF for human septin-2, -6, -7 and -9 **(Figure SI1a)** in both

pocket 1 (septin-7, **Figure SI1b-1**) and pocket 2 (septin-7, **Figure SI1b-2**). See **Figure SI2** for a detailed view of all docking configurations for all filamentous septin isoforms.

To challenge and test the hypothesis that the UR214-9 acts like FCF, *i.e.* causes loss of septin-actomyosin interactions, we choose the mesenchymal triple negative adenocarcinoma MDA-MB-231 cell line. Compared to T cells, MDA-MB-231 cells have distinct contractile actomyosin structures, *i.e.* stress-fibers. We show that acute inhibition of septins GTPase activity **(+UR214-9)** results in rapid translocation of septins (*e.g.* innate septin-9, immunofluorescent analysis) from the stress-fibers to the cytosol **(Figure SI1c**, **+DMSO** *vs.* **+UR214-9)**. Rapid translocation of septins is accompanied by the structural dissolution of stress-fibers that results in partial cell retraction and detachment **(Figure SI1c**, **+UR214-9**, 1 hour**)**. A prolonged UR214-9 treatment results in complete retraction of cells and translocation of septin-9 onto the microtubules, which in turn reorganize into the cell-deforming circumferential microtubule (MT) bands **(Figure SI1c**, **+UR214-9**, 4 hours**)** (Zhovmer et al., 2021). Similarly, the collapse and disintegration of septin-9-positive filaments network into the curled fragments **(Figure SI3a**, **+DMSO**, **+UR214-9**, 1 hour**)** occurs during the first hour after the addition of UR214-9 to the live cells transfected with GFP-septin-9 (*i.e.* septin-9-overexpressing cells). Extended treatment with UR214-9, beyond 1 hour, drives translocation and accumulation of GFP-septin-9 onto the microtubular rings in the retracted cells **(Figure SI3c**, **+UR214-9**, 4 hours**).** Additionally, the suppression of actomyosin contractility by targeted myosin II inhibition with Blebbistatin results in a collapse of the stress-fibers decorated with septin-9, as shown by fragmentation of GFP-septin-9 filaments distribution in MDA-MB-231 cells, no longer associated with actomyosin fibers **(Figure SI3b**, **+Blebbistatin**, 50 μM, 1 hour**)**. These results indicate that active septins preferentially colocalize with the tensile F-actin structures, and rapidly dissociate from the actomyosin upon its acute mechanical relaxation **(+Blebbistatin)**. Septins' localization bias towards the mechanically stressed actomyosin is also demonstrated by acute septin's inhibition **(+UR214-9)** which results in a translocation of septins away from the tensile actomyosin (stress-fibers), and is similarly accompanied by the rapid disassembly of stress fibers. These results indicate that UR214-9 acts like FCF and causes the loss of septin-actomyosin interactions. Moreover, we show that septins and contractile actomyosin structures are mutually interdependent, *i.e.* septins stabilize the tensile actomyosin, while loss of myosin-driven F-actin contractility destabilizes the associated septin structures. Our results support previously reported findings showing that homozygous loss of septin-9 in mouse embryonic fibroblasts causes a loss of stress fibers and associated septin filaments (Füchtbauer et al., 2011).

To further confirm the observed bias in subcellular distribution of septins (*e.g.* septin-9) towards tensile actomyosin structures, we present the MDA-MB-231 cells to the biomimetic collagen 'fibers' (*i.e.* collagen type-1 orthogonal grid: 1 μm-wide micro-lanes, spaced with 15 μm pitch, G'=50 kPa) which enhance the mechanical and spatial anisotropy of tensile actomyosin. Briefly, the 'fibrous' biomimetic surrogate of an extracellular matrix induces biaxial spreading of mesenchymal cells (Tabdanov et al., 2018a; Zhovmer et al., 2021), which in contractile mesenchymal cells results with their polygonal spreading and configurations featuring linearly stressed arching free cell edges **(Figure SI3c)**. These cell edges display linear organization of actomyosin with linear tension that subsequently reinforce the buildup of tensile stress-fibers *via* positive mechanosensory feedback **(Figure SI3c**, **+DMSO**, *arrows***)** (Tabdanov et al., 2018a; Théry et al., 2006). Immunofluorescence analysis of actomyosin in polygonal cells shows that a major fraction of actomyosin filaments, that experience the highest linear mechanical tension (McEvoy et al., 2017; Théry et al., 2006), assembles at the peripheral free cell edges (*i.e.* arcs). Septin distribution in the polygonal MDA-MB-231 cells shows that septin-9 replicates spatial distribution of the tensile actomyosin. Specifically, our observations indicate that septin filamentous structures display a strong spatial and structural affinity towards the arching free cell edges **(Figure SI3c**, **+DMSO,** single cell view, *arrows*; **Figure SI4**, **+DMSO**, population-wide view, *arrows***)**. Inhibition of septins GTPase activity with UR214-9 abrogates the accumulation of septin-9 within free cell edges and drives septins translocation

onto the microtubules **(Figure SI3c**, **+UR214-9**, single cell view, *arrows*; **Figure SI4**, **+UR214-9**, population-wide view, *arrows***)**. We note that translocation of septin-9 onto the microtubules in the fully spread polygonal MDA-MB-231 cells increases microtubule density **(Figure SI3c**, **+DMSO** *vs.* **+UR214-9)** and induces microtubule curling into the rings in ~80% of the cell population **(Figure SI4**, **+UR214-9**, *arrows***)**, complementing our previous report on septin-9-mediated microtubule reorganization in mesenchymal cells (Zhovmer et al., 2021). We suggest that accumulation of UR214-9-inactivated septin-9 on microtubules may occur either *via* shuttling of septin-9 between: (i) filamentous pool within tensile septin-actomyosin cytoskeleton, (ii) septin-9 deposited on microtubules, and (iii) cytosolic septin-9, which adds to the 7-6-2-2-6-7 septin hexamers resulting in the formation of the 9-7-6-2-2-6-7-9 octamers (Bai et al., 2016; Kim et al., 2011; Neubauer and Zieger, 2017), or directly, via a recently identified for the SEPT9_i1 (*i.e.* septin-9, isoform 1) MAP-like motif, which facilitates SEPT9_i1 binding to the MTs (Kuzmić et al., 2021).

In summary, the structural and migration signature of septins in immune cells have been previously studied only in 2D locomotion systems, with no specific role for septins in motility of lymphocytes suggested to date (Gilden et al., 2012; Tooley et al., 2009). For example, only a punctuated pattern of septin striation has been observed in the T cells crawling on the flat surfaces during their 2D 'random-walk', while a knockdown of septin-7 resulted in a T cell uropod elongation and a loss of 'random-walk' efficiency (Tooley et al., 2009). We show that primary human CD4+ T cells compartmentalize their actomyosin cortex during amoeboid migration in the 3D collagen matrix, as demonstrated by the formation of multiple septin-positive cortical F-actin rings. Moreover, we show that inhibition of the septins GTPase activity causes the abrupt loss of T cell segmentation and transitioning to the non-migratory morphology. We also demonstrate that septins act as mechanosensitive F-actin cross-linkers, which preferentially bind and stabilize tensile actomyosin structures, as demonstrated by rapid dissociation of stress fibers and translocation of septins from actomyosin onto microtubules upon acute inhibition of either actomyosin contractility or septins GTPase activity. Therefore, our data suggest that septins are directly involved in the actomyosin-based amoeboid migration of immune cells.

**Septin-templated cell segmentation by cortex-indenting obstacles provides adaptive circumnavigation**

We note that the septin-templated cortical rings always colocalize with the T cell-surrounding, cortex-indenting collagen fibers **(Figure 2a-b**, *arrows***)**. Specifically, septin rings in control hCD4+ T cells assemble exclusively at the cell surface sites indented by collagen fibers **(Figure 2a**, *arrows***)**. A detailed analysis shows that control T cells **(+DMSO)** feature an average of 1 to 2 rings per cell **(Figure 2b**, *left***)**, and no cortical rings are observed without a cell surface-indenting contact with collagen fibers **(Figure 2b**, *right***).** From the mechanistic standpoint, collagen fibers provide no adhesion signals, but create abundant crowding interactions for the migrating T cells (Wolf et al., 2003). Additionally, septins are well-known sensors of the plasma membrane curvatures (*i.e.,* second order surface curves) that preferentially assemble into isotropic networks on the inside of spheroid (convex) surfaces, avoid concave surfaces, and self-organize into the macroscopic fibers along the spine of the indenting furrow on the inside (mixed, *i.e.* - saddle) surfaces of cell membrane (Beber et al., 2019). Based on these observations, we conclude that cortex-indenting collagen fibers are the appropriate and the only available triggers for the local assembly of septins fibers that will further template condensation of cortical F-actin rings **(Figures 1d** and **2a)**. Thus, for immune cells, the external topography of the collagen matrix surrounding an initially spheroid immune cell **(Figures 2c-1**, **2d-1)** spatially guides septin-driven compartmentalization of the cell cortex and ensures its morphological conformity to the surrounding matrix during migration **(Figures 2c-2**, **2d-2)**. Notably, our data suggests that the mechanism of ECM-guided cell compartmentalization is universal across various

types of immune cells. For example, natural killer NK-92 lymphocytes condense septin fibers as the precursors of the cortical rings along the collagen fibers-induced indentations **(Figure 2e**, *arrows***).**

For T cells, and other lymphocytes, ameboid motility *via* externally guided cell compartmentalization represents a previously uncharacterized steric mode of contact guidance. Specifically, septins sense the cortex-indenting mechanical collision of the cell cortex with surrounding obstacles and trigger the formation of F-actin-dense cortical rings. In turn, the cortical rings locally stabilize and constrict the expanding cell cortex against the applied external stimuli, hence, reducing its excessive pressure against the obstacles (*i.e.*, obstacles evasion). Subsequently, the event of obstacle evasion creates a sterically interactive furrow in the form of the septin rings between T cell segments, which facilitates transient steric lock with the obstacles **(Figure 3a)**. The typical topographic 'segment-ring-segment' unit of the steric lock represents a mechanical basis for adhesion-independent invasive amoeboid propulsion by peristaltic translocation of cytosolic content into the newly forming invading cell segment **(Figure 3b)**. The stepwise translocation of cytosolic content along the chain of 'segment-ring-segment' units suggests that septins spatiotemporally template contractility of the actomyosin cortex to coordinate cytosolic hydrostatic pressure and channel peristaltic translocation of cytosol and nucleus between cell segments (Dolat et al., 2014; Salameh et al., 2021). Indeed, the immunofluorescence analysis of segmented T cells reveals an uneven spatial distribution of activated phosphorylated (Ser19) myosin across adjacent cell cortical segments **(Figure 3c-1)**. Differential density of activated cortical actomyosin between individual cell segments **(Figure 3c-2)** indicates that each segment can feature an independent and different level of cortical contractility. Notably, the independent and different level of cortical contractility across cell segments is a principal condition required for the peristaltic dynamics of the entire cell cortex, enabling stepwise translocation of cytosolic content, *i.e.* cytoplasm and nucleus, along the chain of cell segments.

Moreover, our immunofluorescence data aligns with the experimentally observed peristaltic translocation of cytosol and nucleus across multiple segments during live 3D migration of T cells in collagen matrix **(Figure 1c-d**, **+DMSO**; **Movies 1**, **2** and **3**, **Figure SI5)**. Indeed, we observe that each locomotion cycle in a migrating cell includes cytosol/nucleus propulsion, and initiation of new cell segments. The 'old' or utilized cortical segments, which are located behind the nucleus, undergo gradual degradation, recycling, and compaction, which manifests as the rear-located cylindrically shaped uropod **(Figure 3d)**. Notably, we suggest that the newly formed segment 'neck' provides the cell with a temporary 'furrow-fiber' steric lock and allows peristaltic propulsion without friction-loaded displacement of the entire cell cortex. Thus, while migrating T cells peristaltically translocate their cytosolic content from the mature segments into the newly extended compartments, they retract the old segments, which results in a segment-wise lymphocyte treadmilling as the principal mechanism of the T cell amoeboid migration. Based on the existing model for the stochastic cortical instability as a driving force of amoeboid motility (Ruprecht et al., 2015), we formulate a model of a non-stochastic amoeboid migration, *i.e.* amoeboid migration driven by ECM structure. Particularly, we suggest that the mechanical collision between the expanding cell segment and the confining steric obstacles creates cortical indentations which trigger a septin-based condensation of a new cortical ring and separation of a new cell segment. The treadmilling of ECM-conformed cell segments provides lymphocytes with a mechanism for obstacle-avoiding peristaltic translocation of cytosol and nucleus between cell segments **(Figure 3e)**. For a sterically complex 3D environment, like collagen matrix, the resultant T cell's trajectory manifests as circumnavigation, *i.e.* obstacle-evasive zigzag-like trajectory of cells with a stepwise peristaltic translocation of nucleus along the chain of cell segments. Notably, live imaging of the multi-segmented hCD4+ T cells within the 3D collagen matrix shows that lymphocytes repeatedly form leading segments **(Figure 3f**, **Movie 1)**, which results in the zigzagging trajectory of migration between and around collagen fibers through the available lumens (*i.e.* circumnavigation). During the circumnavigation in the structurally crowded environment (*e.g.* 3D collagen matrix) T cells treadmill

discrete shrinking and newly-formed, expanding segments, formed in response to cell surface-indenting steric obstacles **(Figure 3g)**.

In summary, our data suggests a mechanism of amoeboid motility for immune cells that is alternative, yet complementary to the previously described mechanism of amoeboid motility in non-immune melanoma cells (Adams et al., 2021; Logue et al., 2015). Briefly, the basis of amoeboid cell motility in melanoma cells is a cortex treadmilling within the lasting leader bleb that powers friction-based cell sliding within an ideal "sandwich"-like microenvironment, *i.e.* between two parallel flat surfaces. Instead, the basis of amoeboid motility in immune cells is a continuous ECM-guided formation of cortical rings which provide transient subdivision of the whole cell into a series of relatively independent contractile segments. The stepwise treadmilling of cell segments results in the spatially adaptive (*i.e.* non-stochastic) peristaltic propulsion of amoeboid cells and their hindrance-evasive 3D circumnavigation that operates without friction-loaded displacement of the entire T cell cortex against a structurally crowded 3D microenvironment.

**Septins GTPase activity provides a molecular switch from amoeboid towards mesenchymal-like T cell migration**

To understand the mechanisms of septins' involvement (Gilden et al., 2012; Tooley et al., 2009) into the amoeboid migration of T cells (Wolf et al., 2003), we examine migration responses of human CD4+ (hCD4+) T cells - (1) in the 3D collagen matrix **(Figure 4a)** and (2) on 2D anisotropic adhesive contact guidance system, *i.e.* 1 μm-wide, 15 μm-pitched ICAM1 micro-lanes (**Figure 5a**), while perturbing septins' GTPase activity.

As described above, T cells actively migrate through the 3D collagen matrix in control conditions **(+DMSO)** while robustly segmenting their actomyosin cortex by septin-positive F-actin cortical rings **(Figure 1a, c-d**, **+DMSO)**. The motile T cells demonstrate robust treadmilling of cell segments **(Movie 1)** and an active segment-to-segment translocation of cytoplasm and nucleus passage through the cortical rings **(Figure 1c-d**, **+DMSO**; **Movies 2** and **3**, **Figure SI5)**. Notably, inhibition of septins' GTPase activity **(+UR214-9)** causes an abrupt loss of the amoeboid organization in hCD4+ T cells: **(1)** loss of cell segmentation, **(2)** loss of cortical rings, and **(3)** formation of multiple elongated protrusions **(Figure 1c-d)**. The septins inhibition also substantially reduces the speed of migrating T cells to the near arrest **(Figure 4b**, **+DMSO** *vs.* **+UR214-9)**, and substantially decreases their effective migratory displacement **(Figure 4c**, **+DMSO** *vs.* **+UR214-9)**. Since actomyosin contractility powers amoeboid dynamics in T cells (Tabdanov et al., 2021; Takesono et al., 2010), inhibition of the actomyosin contractility **(+Blebbistatin)** also reduces cell speed and displacement **(Figure 4b-c**, **+DMSO** *vs.* **+Blebbistatin)**, although with lower efficiency than UR214-9 **(Figure 4b-c**, **+UR214-9** *vs.* **+Blebbistatin)**. The dynamic enhancement of the actomyosin contractility *via* MT→GEF-H1→RhoA signaling axis, achieved by microtubule depolymerization **(+Nocodazole**, 5 μM**)** (Krendel et al., 2002; Tabdanov et al., 2021; Takesono et al., 2010), substantially increases migration speed **(Figure 4b**, **+Nocodazole**, 1 hour**)**, but not the effective 3D displacement **(Figure 4c**, **+Nocodazole)** due to the substantially reduced directionality persistence of cell migration **(Figure 4b-c**, **'*diffusion exponent*'** and **'*directional ratio*'**). On the contrary, non-dynamic overactivation of the actomyosin contractility *via* 'locking/freezing' the actomyosin in the hypercontractile state, which leads to a non-productive actomyosin contractility (*i.e.* high tension, low dynamics), collapses T cells into immotile spheroids **(Figure 4b-c**, **+Calyculin A**, 50 nM, <1 hour**)**. It has been also reported that dynein contractility within microtubular apparatus can play an important role in determining the cellular 2D/3D architectures, mechanical properties, alignment and migration along the microenvironment's guidance cues (Zhovmer et al., 2021). However, perturbation of dynein's activity in the T cells within collagen matrices induces no significant changes in amoeboid T cell speeds and spatial displacement during dynein inhibition with Dynapyrazole A **(Figure 4b-c**, **+Dynapyrazole A)**.

Unlike in the 3D microenvironment, amoeboid T cells are largely unresponsive to the guidance cues used in the flat 2D systems (Aoun et al., 2020; Tabdanov et al., 2021). For example, crawling T cells display a meandering 'random walk' in 2D systems despite the T cells' active adhesiveness to the ICAM1 *via* LFA1 integrin receptors (Aoun et al., 2020; Krummel et al., 2014). This cell behavior indicates that complex amoeboid shape-changing dynamics of the entire actomyosin cortex dominates over the reduced T cell's 2D adhesion 'footprint' (Krummel et al., 2014; Tabdanov et al., 2021), allowing T cells to redistribute cortical stresses regardless of the configuration of the underlying 2D adhesive guidance cues (Tabdanov et al., 2021; Takesono et al., 2010). However, the exact mechanism that allows the adhesion-free cortical dynamics to dominate over the 2D adhesion is unclear (Krummel et al., 2016). For example, shifting T cells away from the amoeboid phenotype with actomyosin contractility inhibitors does not enhance their contact guidance along the flat (2D) adhesion guidance cues, and poor 2D contact guidance remains largely indifferent to the modulation of microtubules→GEF-H1→RhoA signaling axis in T cells (Tabdanov et al., 2021). Based on our observation made for T cells in the 3D collagen matrix, we propose that an alternative mechanisms for suppression of actomyosin dynamics, *e.g.* by septins inhibition, can enhance T cells' conformity to 2D guidance cues and explain the observed instances of *in vivo* migratory compliance of T cells to the adhesion guidance cues (Overstreet et al., 2013). To test this hypothesis, we put T cells on a substrate designed to reveal cell shape and migration compliance in the form of their alignment to the 2D anisotropic adhesive contact guidance cues, *i.e.* 1 μm-wide, 15 μm-pitched ICAM1 micro-lanes **(Figure 5a)**. In the control conditions **(+DMSO)**, T cells display amoeboid, *i.e.* 'random walk' crawling dynamics, and display no detectable structural or migratory alignment to the ICAM1 micro-lanes **(Figure 5a-c**, **+DMSO**, **Movies 4**, **5** and **6)**. The detailed analysis of T cell migration on the ICAM1 micro-lanes shows that T cells display a random distribution of directionalities, as measured within 20 second-long timeframes **(Figure 5b, +DMSO)**, and highly meandering migration tracks of individual cells **(Figure 5c**, **+DMSO)**. Upon acute septins inhibition **(+UR214-9**, $t \ll 1$ hour**)**, T cells abruptly transition towards a mesenchymal-like alignment and elongation along the ICAM1 micro-lanes **(Figure 5a**, **+UR214-9)**, which is accompanied by a highly aligned and persistent migration along the ICAM1 micro-lanes **(Figure 5b-c**, **+UR214-9)**. The migration speed of amoeboid T cells **(Figure 5d**, **+DMSO**) is routinely higher (~22 μm/min) compared to the mesenchymal-like T cells (~7.5 μm/min, **Figure 5d**, **+UR214-9**), which reflects a higher rate of the amoeboid cortex dynamics, compared to the rate of cytoskeleton reorganization configured by the mesenchymal-like adhesion mechanisms (Krummel et al., 2014). Our results indicate that septins inhibition triggers mechanobiological reprogramming of T cells towards non-amoeboid motility. Specifically, septins inhibition suppresses the formation of cortical rings **(Figure 1c-d**, **+UR214-9)** and the amoeboid migration in 3D collagen gels **(Figure 2b-c**, **+UR214-9)**. Moreover, septins inhibition activates mesenchymal-like migration that manifests as directional alignment (*i.e.* contact guidance) of T cells along the adhesive ICAM1 micro-lanes **(Figure 5**, **+UR214-9)**.

We note that during amoeboid-to-mesenchymal-like phenotypic transition, induced by septins inhibition **(+UR214-9)**, cells increase microtubules' density and length **(Figures 5a**, **6a**, **Sl6a**, **+DMSO** *vs.* **+UR214-9)**. To confirm the UR214-9-induced enhancement of microtubules, we study microtubule density in control **(+DMSO)** and UR214-9-treated live hCD4+ and hCD8+ T cells **(Figure 6b-c)**, by flow cytometry using SiR-Tubulin stain (microtubule dye for live imaging). Our results show that hCD4+ and hCD8+ T cells display ~60% and 45% increase of microtubule network density, respectively, following septins inhibition **(+UR214-9**, 1 hour**)** as compared to the control **(+DMSO)** cells **(Figure 6b-c)**. We also confirm the UR214-9-induced growth of microtubules **(**see also **Figures 5a**, **6a** and **7c)** using atomic force microscopy analysis, which is similar to our previous experiments with the Taxol-mediated stabilization of microtubules and increase of passive rigidity of T cells (Tabdanov et al., 2021). Indeed, UR214-9-induced microtubule build-up demonstrates a substantial similarity between UR214-9- and Taxol-mediated effects with respect to the increase of T cell mechanical rigidity **(Figure 6d)**. Notably, addition of Blebbistatin to either UR214-9

or Taxol treatment conditions does not soften the T cells to the rigidities observed for a sole Blebbistatin treatment **(Figure 6d**, **±Blebbistatin** *vs.* **+UR214-9±Blebbistatin** *vs.* **+Taxol±Blebbistatin)** or for the control condition **(+DMSO**, baseline mechanical rigidity**)**. We have previously demonstrated that Nocodazole-induced T cell rigidification was completely reversed by the following Blebbistatin co-treatment (Tabdanov et al., 2021). Moreover, septins inhibition with UR214-9 is followed by septins release from actomyosin and relaxation of the amoeboid cortex (Dolat et al., 2014). Similarly, microtubules stabilization, *e.g.* induced by septins inhibition, cause an uptake of cytosolic GEF-H1 with a subsequent reduction of the RhoA→actomyosin contractility signaling axis (Tabdanov et al., 2021; Takesono et al., 2010). Therefore, the heightened T cell rigidities during **+UR214-9±Blebbistatin** or **+Taxol±Blebbistatin** treatments reflect the additional passive mechanical rigidity of stabilized microtubule apparatus. Based on our measurements, we conclude that enhanced microtubules compensate for the diminished mechanical contribution of actomyosin to the cell mechanics during the amoeboid-to-mesenchymal-like transition of T cells.

In summary, our results show that UR214-9-mediated septins inhibition induces mechanobiologically coherent and synergistic effects, *e.g.* - (1) activation of mesenchymal-like 2D motility, including the contact guidance along the adhesive ICAM1 micro-lanes, (2) loss of the amoeboid phenotype and 3D motility, and (3) enhancement of the microtubular network that supports mesenchymal-like phenotype (Vasiliev et al., 1970) and compensates for the diminished mechanical contribution of actomyosin. Together these results indicate that inhibition of septins GTPase activity provides a molecular switch from amoeboid towards mesenchymal-like T cell migration.

**Septin-mediated stabilization of microtubules and dynein activity enhance mesenchymal-like migration of T cells**

Mechanobiological plasticity of T cells migration, *i.e.* during septin-coordinated transition between actomyosin-dependent amoeboid and microtubule-based mesenchymal-like states, is linked to the mechanosensitivity of integrin receptors. For example, like other integrin receptors, ICAM1 receptor LFA1 is a mechanosensor (Chen et al., 2010; Hynes, 2002; Tabdanov et al., 2015). Therefore, the UR214-9-treated T cells, during contact guidance on ICAM1 adhesion cues, must generate sufficient tension within LFA1 β2 subunit clusters to activate and sustain cell adhesion, spreading and mesenchymal-like migration (Nordenfelt et al., 2016). Notably, for mesenchymal cells in a low actomyosin contractility state, stabilization and elongation of microtubules is critically important for development and maintaining the dendritic protrusions along the collagen type-1 contact guidance cues (Rhee et al., 2007; Shakiba et al., 2020; Tabdanov et al., 2018a, 2018b). Furthermore, microtubular network is mechanically integrated into the F-actin cytoskeleton *via* force-generating dyneins (Fokin et al., 2021; Jimenez et al., 2021), forming a singular microtubules/actomyosin force transmission system that shares common adhesion receptors to guide T cell spreading along extracellular cues. In our previous report, we showed that dyneins activity ('minus' end-directed microtubule motors) in mesenchymal cells regulates the spreading of dendritic cell protrusions, cell contractility, microtubule bundling and topography-mediated contact guidance (Zhovmer et al., 2021). Additionally, we demonstrated that dyneins actively pull the microtubules into the adhesion sites to facilitate cell-substrate steric interactions and cell alignment *via* the microtubule scaffolding effects (Tabdanov et al., 2018b), similarly to dyneins role in the fibroblast's migration upon suppression of the RhoA-dependent actomyosin contractility (Kim et al., 2012). These observations suggest that dynein-driven forces within the enhanced (*i.e.* dense and long) microtubules in UR214-9-treated T cells produce compensatory tension that is substantial for activation of LFA1 in the absence of sufficient actomyosin tension.

To test the proposed force generation mechanism, we analyze post-translational modifications of microtubules, since microtubule acetylation enhances dynein processivity (Alper et al., 2014; Badding and Dean, 2012) and microtubule detyrosination enhances uninterrupted dynein processivity along the microtubules (McKenney et al., 2016). Our results align with the possible mechanism of septins-mediated molecular switch from amoeboid towards mesenchymal-like T cell migration *via* gain of microtubules' density and length, as indicated by an increase of microtubule post-translational modifications, *i.e.* acetylation (~20%) and detyrosination (~25-40%) **(Figure 7a)**. These post-translational modifications rely on multiple synergized contours of the mechanobiological signaling that interconnect septins, microtubules and actomyosin signaling pathways **(Figure 7b)**. For example, intact septin-7 suppresses the microtubule-stabilizing protein (MAP) MAP4 (Kremer et al., 2005), while also sustaining the downstream HDAC6-mediated deacetylation of microtubules (Ageta-Ishihara et al., 2013). Thus, inhibition of septin-7 converges into stabilization of the microtubule network *via* both enhancement of microtubule acetylation **(Figures 7a** and **SI6b**, **+DMSO** *vs.* **+UR214-9)** and MAP4-MTs binding **(Figure SI6c-d)** that also causes MAP4-induced microtubule detyrosination in T cells (Bustos-Morán et al., 2017) **(Figure 7a)**. Additionally, SEPT9_i1 isoform binds to microtubules *via* its MAP-like motif (Bai et al., 2016; Kuzmić et al., 2021; Nakos et al., 2019) resulting in stabilization of the microtubular network by preventing the microtubule filaments growth catastrophes (Nakos et al., 2019) either indirectly or directly by intrinsic septin-9 MAP-like activity (Kuzmić et al., 2021). Thus, UR214-9-induced suppression of septins' GTPase activity causes a release of inactive septin-9 from actomyosin to cytosol, which subsequently translocates onto the microtubules *via* its intact MAP-like motif, resulting in the stabilization of microtubule apparatus, as GTPase activity is dispensable for septin-9's MAP-like microtubule-stabilizing activity, as shown in MDA-MB-231 cells (Zhovmer et al., 2021) **(Figures SI3c** and **SI4)**, and in hCD4+ T cells **(Figure SI6e)**. The suggested mechanism is supported by the observed septin-9→kinesin signaling pathway effects that cause kinesin-driven microtubules curling, looping and circularization into the microtubule rings **(Figures SI3** and **SI4**, **+UR214-9**, *arrows***)**, reported for various types of cells (Zhovmer et al., 2021). Furthermore, the homozygous loss of septin-9 (SEPT9 -/-) in fibroblasts also results in the loss of the transmigration efficiency, that complements the septin-dependent mechanism of microtubular apparatus stabilization required for cell transmigration (Füchtbauer et al., 2011).

To test the proposed mechanism of microtubule stabilization *via* MAP4 and downstream HDAC6-mediated pathway, we confirm that the UR214-9-induced T cell transition from the amoeboid 'random-walk' **(Figures 5a** and **5b**, **+DMSO**; **Movies 4** and **5**, **before UR214-9)** towards the mesenchymal-like migration and contact guidance along the ICAM1 micro-lanes pattern, *i.e.* guided cell elongation and alignment to the ICAM1 architecture **(Figure 5a**, **+UR214-9**, t=30 min; **Movies 4** and **5**, **after UR214-9**, **Movie 6)** extends to the more complex ICAM1-based 2D contact guidance cues such as orthogonal grids **(Figure 7c**, **+DMSO** *vs.* **UR214-9)**. Indeed, T cells in control conditions **(+DMSO)** display a non-spreading amoeboid morphology and meandering 'random walk' migration, regardless of the geometry of the ICAM1 grid **(Figure 7c**, **+DMSO**, **Movie 7)**. Septin inhibition with UR214-9 abruptly (bi-phasically) switches T cells to the 'dendritic' spreading along the ICAM1 grid within the first 30 minutes of treatment **(Figure 7c**, **+UR214-9**, t=30 min, **Movie 8)**. The 'dendritized' T cells acquire the extremely elongated multi-apical morphology after ~1 hour-long UR214-9 treatment **(Figure 7c**, **+UR214-9**, t≥1 hour**)**. UR214-9-induced dense and elongated microtubule bundles constitute the core of dendritic protrusions along the ICAM1 grid **(Figure 7c**, **+UR214-9**, microtubules view**)**. Next, we induce stabilization of microtubules in hCD4+ T cells by hyperacetylation through a direct suppression of HDAC6 **(+Tubacin,** 25 μM,1 hour**)**. Tubacin-treated T cells partially replicate the UR214-9-induced mesenchymal-like mode transition, *i.e.* by phenocopying the 'dendritic' spreading along the ICAM1 grids **(Figure SI7a**, **+DMSO** vs. **+Tubacin)**. The 'dendritic' spreading of Tubacin-treated T cells is also accompanied by a significant enhancement of the microtubule acetylation that expands from the initially limited, MTOC-associated acetylated tubulin cluster **(Figure SI7b**, **+DMSO**,

*arrows*) to the dense and elongated acetylated microtubule network **(Figure SI7b**, **+Tubacin)**. Our analysis shows that microtubule acetylation **(Figure SI6b)** and MT detyrosination **(Figure 7a)** are both increased in response to the septins inhibition **(+UR214-9).** Moreover, the Blebbistatin treatment does not affect structural compliance and migrational guidance response of UR214-9-treated T cells to ICAM1 grids **(Movie 9)**, indicating that actomyosin contractility is both dispensable and diminished during septin inhibition-induced dendritic cell spreading. On the contrary, UR214-9-induced T cell 'dendritic' spreading and mesenchymal-like locomotion along the ICAM1 micropatterns are immediately abrogated upon addition of the dynein inhibitor, Dynapyrazole A, at the final concentration of 25 μM **(Movie 10**, **+UR214-9+Blebbistatin→+UR214-9+Blebbistatin+Dynapyrazole A)**. Alternatively, the retraction of dendritic protrusions in UR214-9-treated cells can be achieved directly, *i.e.* by adding Dynapyrazole A to UR214-9-treated T cells without presence of Blebbistatin **(Movie 11**, **+DMSO→+UR214-9→+UR214-9+Dynapyrazole A)**, highlighting the dispensability of actomyosin contractility during UR214-9-induced mesenchymal-like T cell adhesion and spreading. The subsequent washout experiment demonstrates the reversibility of the mesenchymal-like cytoskeleton dynamics, *i.e.* a recovery of the T cell amoeboid migration **(Movie 11**, **washout)**. Importantly, the separate treatment with either Blebbistatin or Dynapyrazole A alone does not show any change to the pre-existing T cell amoeboid migration mode **(Movie 12**, **+DMSO→+Blebbistatin**; **Movie 13**, **+DMSO→+Dynapyrazole A)**.

In summary, we demonstrate that the inhibition of septins GTPase activity induces rapid transition of T cells from the actomyosin-driven amoeboid crawling to the dynein-driven mesenchymal-like spreading on ICAM1 substrates. Based on our results, we suggest a model **(Figure 7d)** where pharmacological targeting of septins triggers mechanobiological transition of T cells between (1) actomyosin-driven amoeboid migration **(Figure 7d-1)**, and (2) dynein-driven mesenchymal-like migration **(Figure 7d-2)**. Mechanistically, the inactivation of septins reduces dynamics of the amoeboid cell cortex to the level that allows for migration compliance to the 2D adhesive guidance cues. In addition, inactivated septins stabilize the microtubular network *via* MAP4 and septin-9 MAP-like pathways, hence facilitating the microtubule-mediated uptake of GEF-H1 from the cytoplasm, and causing additional suppression of actomyosin contractility. Instead, the septins-mediated stabilization of microtubules enhances the processivity of dyneins within the microtubule cables, that compensates for the diminished actomyosin contractility during the adhesion-based LFA1 activation, *i.e.* in the absence of the stabilizing septin-actomyosin interactions (Dolat et al., 2014; Kremer et al., 2007; Salameh et al., 2021; Schmidt and Nichols, 2004).

**Actomyosin- and dynein-based force generation acts jointly during transmigration**

Transmigration of immune cells is a complex series of events to include an extreme cell body deformation, such as elongation and narrowing, for sliding through the confining spaces, *e.g.* between the endothelial or epithelial cells. The cell entrance and rapid passage through the confining spaces requires relaxation and "fluidization" of the actomyosin cortex, which facilitates structural compliance and deformability of immune cells **(Figure 8a)**. The mechanics of transmigration process draws a significant scientific and clinical interest, and has been extensively studied, however, the exact mechanobiological fundamentals that underpins cytoskeletal plasticity of lymphocytes' organization for migration under extreme deformation and confinement remains largely unknown. For example, it is evident that an active generation of mechanical force is required to power the transmigration process, but actomyosin contractility is often diminished or dispensable in transmigrating cells (Balzer et al., 2012; Hung et al., 2013; Paul et al., 2017; Rolli et al., 2010; Stroka et al., 2014). On the other hand, transmigrating lymphocytes require a rupture-resistant cytoskeletal organization to avoid danger of extreme overstretching and losing the cell integrity *via* cell rupture. Thus, an effective, long-distance force transmission system is necessary for a structurally and mechanically coherent transmigration of elongated cells through the narrow pores.

Our results indicate that dynein-generated mechanical forces can be transmitted at long distances along the microtubules that behave as non-stretchable cables, as demonstrated by UR214-9-treated T cells that use microtubules and dyneins to compensate for diminished actomyosin contractility in the “dendritic” mode of 2D adhesion and spreading **(Figure 7d)**. Complementary to our findings, it is reported that in extremely confining microchannels (≤ 4 μm-wide) T cells migration does not depend on the actomyosin contractility (Jacobelli et al., 2010; Krummel et al., 2014), but is critically dependent on the intact microtubular system (Balzer et al., 2012; Kopf et al., 2020). Together, these observations suggest that mechanobiological fundamentals of amoeboid and mesenchymal-like migrational plasticity of T cells in confinement is based on the coordinated reorganization of actomyosin and microtubule cytoskeletons.

In order to test the contribution of these two principal cytoskeletal components during transmigration (*i.e.* migration through confined spaces), we examine passage of primary hCD4+ and hCD8+ T cells through the ICAM1-coated 3 μm pores in ~10 μm-thick polycarbonate TransWell membranes **(Figure 8a)**. We aim to test a simple mechanistic model for T cell transmigration through the pores that includes: (1) the T cell adhesion and deformation-driven pore entrance, (2) confined cell passage, and (3) cell exit. In this model, the microtubule-based transmission of mechanical forces along the pore-confined portion of the cell body becomes critical for linking all parts of a T cell on both sides of the transmigration pore **(Figure 8b)**. In a more general mechanobiological model of T cell migration (low confinement, before entrance and after exit) and transmigration (high confinement, within a pore), the process should also include a combination of the (1) actomyosin-driven/septin-structured circumferential cortical contractility **(Figure 8c-1)**, and (2) axial contractility of the dynein motor proteins, mechanically transmitted along the T cell axis *via* the non-stretchable microtubules **(Figure 8c-2)**. First, we test that suppression of the septin-mediated amoeboid cortical dynamics affect transmigration of T cells. Our results show that either a direct inhibition of septin **(+UR214-9**, 25 μM**)** or a direct inhibition of actomyosin contractility **(+Blebbistatin**, 25 μM**)** results with a partial (≤50%) loss of hCD4+ and hCD8+ T cell transmigration efficiencies **(Figure 8d**, **+UR214-9**, **+Blebbistatin)**. Our observations complement a previous report showing that mouse embryonic fibroblasts with homozygous loss of septin-9 (SEPT9 -/-) substantially lose their transmigration efficiency through tested 8 μm pores (Füchtbauer et al., 2011). This data indicates that amoeboid 3D cortical dynamics is an important component of the T cell transmigration process. Indeed, as we suggested before, the amoeboid cortical dynamics enables T cell-microenvironment steric interactions that are required for pore engagement and entrance **(Figure 8a)**. We should note that the porous TransWell membrane is not a fully adequate transmigration system, as the membrane represents a dense array of adjacent pores that are capable of non-physiological simultaneous engagement of several alternative T cell protrusions **(Figure 8e)**. Therefore, while UR214-9-treatment may enhance dynein-driven T cell transmigration through a single pore, the stabilized and elongated microtubules lead to T cell entanglement and trapping between several adjacent pores **(Figure 8a**,**e)**. Moreover, since force transmission includes mechanical coupling of dyneins and F-actin (Fokin et al., 2021; Jimenez et al., 2021), the loss of cortical actomyosin contractility, caused by either UR214-9 or Blebbistatin treatments may compromise the transmission of dynein-generated forces to the T cell surrounding environment, causing overall loss of T cell transmigratory efficiency.

In agreement to our model’s prediction about the microtubule-based mechanical force transmission along the pore-confined portion of the cell **(Figure 8b)**, the suppression of the dynein motor activity **(+Dynapyrazole A**, 25 μM**)** leads to a substantial (≤40%) loss of the hCD4+ and hCD8+ T cell transmigration **(Figure 8d**, **+Dynapyrazole A)**. In contrast, amoeboid migration of T cells through fibrous (3D collagen) matrices displays no detectable response (*i.e.* migration speeds, displacement distances) to the acute dynein inhibition, as compared to the control cell group **(Figure 2b-c**, **+DMSO** *vs.* **+Dynapyrazole A)**. Thus, the dynein-MT-based contractility and force transmission are indispensable during transmigration in confined spaces **(Figure 8b)**, while amoeboid motility in low confinement, *i.e.*

within fibrous collagen gel, does not critically depend on dyneins and microtubules for force production and transmission.

The disassembly of the microtubules **(+Nocodazole**, 5 μM**)** should cause the loss of dynein-microtubule contractility and reduction of cell transmigration. However, Nocodazole treatment results with inconsistent and insignificant changes of the transmigration efficiency for hCD4+ and hCD8+ T cells **(Figure 8d**, **+Nocodazole)**. We attribute this data to mutually compensating effects of Nocodazole treatment. Indeed, we have previously determined that along with the direct and evident loss of the microtubule as a structural components of T cells, destabilization and loss of the microtubules also causes a substantial increase in T cell contractility and amoeboid behavior *via* microtubules→GEF-H1→RhoA signaling axis (Tabdanov et al., 2021). Thus, the loss of the dynein-driven contractility can be conversely compensated by an increase of actomyosin-driven contractility. This observation is supported by the recent seminal work reporting that in the confined migrating dendritic cells the local microtubules destabilization induces a gain of RhoA-dependent actomyosin contractility (Kopf et al., 2020). We suggest that for cells with dynamic (*i.e.* non-entangling) microtubules, enhanced actomyosin contractility would become a principal transmigration force. Therefore, we test a direct increase of actomyosin contractility with intact microtubules *via* G-switch **(+RhoA activator II**, 3 μg/mL**)**, which increases T cell amoeboid dynamics (Tabdanov et al., 2021). Our results demonstrate an increase of transmigration for both hCD4+ and hCD8+ T cells **(Figure 8d**, **+RhoA activator II)**, which is in line with conclusion that amoeboid and mesenchymal-like mechanisms of motility are mechanically synergized and compensating during transmigration.

Our model also predicts that disassembly of the microtubule network, if combined with inactivation of septins **(+Nocodazole+UR214-9)**, would lead to a substantial GEF-H1-mediated increase of the actomyosin contractility but without the septin-coordinated cortex compartmentalization, and without microtubular network enhancement. Such simplified actomyosin contractility and the absence of stretch-resistant microtubular cables are expected to lead to the extreme T cell transmigratory plasticity, albeit at the cost of substantial loss in cell structural stability (Kopf et al., 2020). Indeed, the transmigration efficiency of both hCD4+ and hCD8+ T cells during UR214-9+Nocodazole treatments display an increased rate of T cell transmigration **(Figure 8d**, **+Nocodazole+UR214-9)**. However, transmigrated T cells display decreased sizes of the nuclei **(Figure SI8a)**, as well as cell fragmentation and enucleation **(Figure SI8b)**, pointing towards a loss of cell integrity during passage through the array of 3 μm pores.

Finally, we find that combined targeting of septin with actin or microtubule motors, *i.e.* myosins and dyneins, leads to a more complete arrest of hCD4+ T cell transmigration (≥75%) **(Figure 8d**, **+UR214-9+Blebbistatin**, **+UR214-9+Dynapyrazole A**, **+Blebbistatin+Dynapyrazole A)**. Specifically, septin inhibition, combined with suppression of myosin contractility **(+UR214-9+Blebbistatin)** leads to the simultaneous relaxation of actomyosin cortex *via* Blebbistatin and enhancement of the microtubular apparatus *via* UR214-9, virtually halting T cell transmigration by ~95%. We attribute this effect to the combined inability of cells to perform deformation-driven pore entrance and enhanced entanglement between several pores. Since the suggested model of effective T cell migration and transmigration is based on a synergistic cooperation between septin-actomyosin and microtubules-dynein cytoskeletal subsystems, the suppression of contractility within either septin-actomyosin or microtubules-dynein subsystems leads to a partial loss of T cell transmigration **(Figure 8d**, **+UR214-9**, **+Blebbistatin**, or **+Dynapyrazole)**, whereas simultaneous inhibition of both subsystems **(***i.e.* **+UR214+Dynapyrazole A** or **+Blebbistatin+Dynapyrazole A)** leads to almost complete abrogation of T cell transmigration, in a compliance with the suggested model **(Figure 8c)**.

Together, our results indicate that T cell ability to sense physical niches and adaptively remodel cytoskeletal organization for optimization of cell motility is based on the septin-structured circumferential

contractility of cortical actomyosin and axial contractility of dyneins along the microtubules (**Figures 8c and 9**). If cell confinement is low, *e.g.* during migration within fibrous matrices, the mechanical fulcrum made of collagen fibers provides an adequate physical environment for cell segmentation and actomyosin-based peristaltic propulsion which does not require the microtubular component for cell motility (**Figure 9a**). Namely, septins provide the adaptive T cell 3D circumnavigation by arranging the peristaltic dynamics of actomyosin-derived forces to match the configuration of external physical cues that sterically guide translocation of cytosolic content in amoeboid cells. However, if cell confinement is high, *e.g.* during transmigration in narrow spaces, T cells require microtubule-based dynein contractility for motility since it powers coherent long-distance transmission of dynein-generated tensile forces along the principal axis of the entire cell body (**Figure 9b**). Our conclusions agree with previous reports (Niggli, 2003; Yadav et al., 2019), which indicate that microtubules do not contribute to the force-generating mechanisms required for amoeboid migration. We also complement findings showing that microtubules control cellular coherence of dendritic cells migrating in fibrous gels (Kopf et al., 2020), as we demonstrate that non-stretchable cable-like microtubules prevent T cells from rupturing during extreme deformation in confining spaces. Moreover, our results indicate that microtubules can effectively hinder transmigration by distributing pulling dynein forces between several cell protrusions. Specifically, non-stretchable microtubules can capture T cells in a 'tug-of-war' state if multiple adjacent pores are available.

## Conclusion

In summary, our results indicate that septins are required for amoeboid motility in T cells by the means of cortex partitioning and segment-wise lymphocyte treadmilling that explains the previously reported effects of amoeboid motility loss *via* septin-7 genetic knockdown (Gilden et al., 2012; Tooley et al., 2009). Particularly, we show that primary human CD4+ T cells dynamically compartmentalize their actomyosin cortex by septin-positive F-actin rings that are formed in response to cortical indentations within the 3D collagen matrix. The indenting collagen fibers trigger local septins assembly allowing contractile amoeboid T cell to adapt the shape (*i.e.* form segments) and configuration of cortical forces (*i.e.* individual contractility of cell segments) to the pre-existing spaces, lock on the confining collagen fibers, and exert forces sufficient enough for hindrance-evasive peristaltic propulsion of nucleus and cytoplasm through the series of narrow lumens in 3D microenvironments.

From mechanistic perspective of the septins role as mechanosensitive F-actin crosslinkers, we conclude that stress-fibers and cortical circumferential rings are both functionally and structurally analogous to each other, as the formation of either structure is dependent, at least in part, on the scaffolding and stabilizing effects of septins (Dolat et al., 2014; Kremer et al., 2007; Salameh et al., 2021). Specifically, an anisotropic (*i.e.* aligned) stress-fiber condenses from an isotropic actomyosin network, forming a load-resisting and force-generating actomyosin band between anchoring focal adhesions (Lehtimäki et al., 2021; Vignaud et al., 2021). In T cells, the septins facilitate condensation of F-actin-enriched cortical rings as a circularized (*i.e.* anchorless) form of the stress-fiber to resist the stretching forces (*e.g.* cortex-expanding hydrostatic pressure), while the loss of septins or actomyosin activity results in the loss of amoeboid motility. However, while mesenchymal cells use anchored stress-fibers to enable the mechanosensing of the adhesive microenvironments, the non-adhesive amoeboid cells utilize the anchorless septin-templated cortical rings for their amoeboid non-adhesive motility (Charras and Paluch, 2008; van der Gucht et al., 2005; Paluch et al., 2005; Reversat et al., 2020; Wolf et al., 2003).

Consequently, we demonstrate that the inhibition of septins' GTPase activity induces transition of T cells from actomyosin-driven amoeboid crawling to dynein-driven mesenchymal-like migration and spreading on ICAM1 substrates. Mechanistically, we suggest that inactivation of septins reduces the dynamics of the amoeboid cortex to the level that allows for contact guidance, *i.e.* migration compliance to the 2D adhesive

guidance cues. In addition, we show that inactivated septins stabilize the microtubular network *via* MAP4 and septin-9 MAP-like pathways, which facilitate the microtubule-mediated uptake of GEF-H1 from the cytoplasm for additional sequestration of actomyosin contractility. Instead, the coordinated stabilization and increased post-translational modifications of microtubules enhances the processivity of dyneins within the microtubule network, which compensate for the diminished actomyosin contractility during the adhesion-based LFA1 activation.

Our data demonstrate that actomyosin- and dynein-based force generating systems can act synergistically to propel T cells under different confinement conditions, *i.e.* during migration and transmigration. Particularly, we show that T cells can sense physical niches and adaptively remodel cytoskeletal organization for optimization of cell motility *via* septins' GTPase molecular switch and septin-based structuring of circumferential actomyosin contractility and axial dynein contractility. If cell confinement is low, cell segmentation and actomyosin-based peristaltic propulsion are sufficient for cell motility. If cell confinement is high, microtubule-based dynein contractility is required to power coherent long-distance transmission of tensile forces during transmigration. Together, the septins-driven cell segmentation, cortical peristaltism and dynein-generated forces within microtubular cables compose a mechanism for adaptive motility that allows T cells to move in nearly every tissue, regulating protective and pathological immune responses.

## STAR★METHODS

### Key resources table

| REAGENT or RESOURCE | SOURCE | IDENTIFIER |
|---|---|---|
| **Antibodies** | | |
| AffiniPure Fab Fragment Goat Anti-Human IgG, $Fc_{\gamma}$ fragment specific | Jackson ImmunoResearch Laboratories, Inc | Cat# 109-007-008; RRID:AB_2632440 |
| Anti-Tubulin antibody [YL1/2] | AbCam | Cat# ab6161; RRID:AB_305329 |
| Anti-Tubulin antibody [SAP.4G5] | Sigma-Aldrich | Cat# T7816, RRID:AB_261770 |
| Atto 647N goat anti-mouse IgG | Sigma-Aldrich | Cat# 50185, RRID:AB_1137661 |
| Monoclonal Anti-Tubulin, Acetylated antibody produced in mouse | Sigma-Aldrich | Cat# T6793 |
| Anti-Detyrosinated alpha Tubulin antibody - Microtubule Marker | AbCam | Cat# ab48389 |
| Anti-GAPDH Rabbit mAb [14C10] | Cell Signaling | Cat# 2118; RRID:AB_561053 |
| Purified Non-muscle Myosin Heavy Chain II-A Antibody (Previously Covance catalog# PRB-440P) | BioLegend | Cat# 909801 |
| β-actin rabbit monoclonal antibody | Cell Signaling | Cat# #8457 |
| Rabbit polyclonal anti-MAP4 antibody | AbCam | Cat#ab224543 |
| Alexa Fluor 488 donkey anti-rat IgG (H+L) | Thermo Fisher | Cat# a21208; RRID:AB_141709 |
| Anti-SEPT7 antibody produced in rabbit | Sigma-Aldrich | Cat# HPA023309 |
| Anti-SEPT9 antibody produced in rabbit | Sigma-Aldrich | Cat# HPA042564 |
| Phospho-Myosin Light Chain 2 (Ser19) Antibody | Cell Signaling | Cat# #3675 |
| Goat Anti-Mouse IgG Antibody, Peroxidase Conjugated | Sigma-Aldrich | Cat# AP124P |
| Goat anti-Rabbit IgG (H + L) Secondary Antibody, HRP conjugated | ThermoFisher Scientific | Cat# 31460 |
| **Chemicals, Peptides, and Recombinant Proteins** | | |
| HMS-31, (25-35% Methylhydrosiloxane)-Dimethylsiloxane Copolymer, Trimethylsiloxane Terminated | Gelest, Inc | Cat# HMS-301; CAS#68037-59-2 |
| VDT-731, (7.0-8.0% Vinylmethylsiloxane) - Dimethylsiloxane Copolymer, Trimethylsiloxy Terminated | Gelest, Inc | Cat# VDT-731; CAS#67762-94-1 |
| 2,4,6,8-Tetramethyl-2,4,6,8-tetravinylcyclotetrasiloxane | Sigma-Aldrich | Cat# 396281; CAS#2554-06-5 |

| | | |
|---|---|---|
| Platinum(0)-2,4,6,8-tetramethyl-2,4,6,8-tetravinylcyclotetrasiloxane complex solution | Sigma-Aldrich | Cat# 479543; CAS#68585-32-0 |
| SYLGARD 184 Silicone Elastomer Kit, 0.5 kg KIT | Dow Corning, Sigma-Aldrich | Cat# 4019862; CAS#68988-89-6 |
| 40% Acrylamide Solution, Electrophoresis purity reagent, 500 mL | BioRad | Cat# 161-0140 |
| 2% Bis Solution, 500 mL | BioRad | Cat# 161-0142 |
| Streptavidin Acrylamide, 1 mg | Thermo Fisher, Life Technologies | Cat# S21379 |
| TEMED | Thermo Scientific | Cat# 17919; CAS#110-18-9 |
| Ammonium Persulfate, BioUltra, for molecular biology | Fluka Analytical | Cat# 09913-100G; CAS#7727-54-0 |
| 3-(Trimethoxysilyl)propyl methacrylate | Sigma-Aldrich | Cat# 6514; CAS#2530-85-0 |
| Ethyl Alcohol 200 Proof, Absolute, Anhydrous ACS/USP Grade | Pharmco-Aaper | Cat# 111000200; CAS#64-17-5 |
| Collagen-1, rat | Corning, NY | Cat# 354249 |
| CellAdhere™ Type I Collagen, Bovine, Solution | STEMCELL Technologies, Inc., USA | Catalog # 07001 |
| Mineral Oil Light Oil (Neat), BioReagent, Suitable For Mouse Embryo | Sigma-Aldrich | Cat# M8410 |
| Fibronectin Bovine Protein, Plasma | Thermo Fisher, Life Technologies | Cat# 33010018 |
| Genemate LE Quick DIssolve Agarose | BioExpress | Cat# E-3120-500FG |
| ICAM1, Human Protein, Recombinant, hIgG1-Fc.His Tag, Active | Sino Biological, China | Cat# 10346-H03H-50 |
| Paraformaldehyde, reagent grade, crystalline | Sigma-Aldrich | Cat# P6148-500G; CAS#30525-89-4 |
| Triton X-100 | Sigma-Aldrich (Roche) | Cat# 11332481001 CAS#9002-93-1 |
| DMSO (Dimethyl sulfoxide) | Sigma-Aldrich | Cat# 472301-100ML; CAS#67-68-5 |
| (−)-Blebbistatin, 1-Phenyl-1,2,3,4-tetrahydro-4-hydroxypyrrolo[2.3-b]-7-methylquinolin-4-one | Sigma-Aldrich | Cat# 203391; CAS#856925-71-8 |
| Nocodazole, Microtubule Inhibitor | AbCam | Cat# ab120630; CAS#31430-18-9 |
| Paclitaxel (Taxol) | Sigma-Aldrich | Cat# T7402; CAS#33069-62-4 |
| Dynapyrazole A | Sigma-Aldrich | Cat# SML2127 |
| UR214-9 | Dr. Rakesh Singh | Custom synthesis |
| Calyculin A | Sigma-Aldrich | Cat# 208851 |
| Tubacin | Sigma-Aldrich | Cat# SML0065 |
| Latrunculin A | Thermo Fisher | Cat # L12370 |

| | | |
|---|---|---|
| 0.25% Trypsin, 2.21 mM EDTA, 1× [-] sodium bicarbonate | Corning | Cat# 25-053-CI |
| Plasmocin | Fisher Scientific | Cat# NC9698402 |
| Penicillin Streptomycin Solution, 100X | Corning | Cat# 30-002-CI |
| Fetal Bovine Serum | HyClone | Cat# SH30910.03 |
| Acetic Acid, Glacial | Fisher Chemical | Cat# BP2401-500; CAS#64-19-7 |
| Silanization solution-I | Sigma-Aldrich | Cat# 85126; CAS#75-78-5 |
| 6.5 mm Transwell® with 3.0 µm Pore Polycarbonate Membrane Insert, Sterile | Corning | Cat# 3415 |
| 35 mm NanoSurface Dish | NanoSurface Biomedical, Seattle, WA | Cat# ANFS-0001 |
| 25 mm NanoSurface Coverglass | NanoSurface Biomedical, Seattle, WA | Cat# ANFS-CS25 |
| 35 mm Dish \| No. 1.0 Coverslip \| 20 mm Glass Diameter \| Uncoated | MatTek Corporation | Cat# P35G-1.0-20-C |
| WillCo-dish Glass Bottom Dish \| No. 1.5H Coverglass thickness \| 40 mm Glass Diameter \| Uncoated | WillCo Wells B.V. | Cat# HBST-5040 |
| Cover Glasses, FisherFinest Rectangles, 25×60-1, Thickness 0.13-0.17 mm | Fisher Scientific | Cat# 24X60-1 |
| Cover Glasses, Circles, 15 mm, Thickness 0.13-0.17 mm | Carolina Biological Supply Company | Cat# 633031 |
| SiR Actin, Spirochrome Kit | Cytoskeleton Inc. | Cat# CY-SC001 |
| SiR Tubulin, Spirochrome Kit | Cytoskeleton Inc. | Cat# CY-SC002 |
| Phalloidin-Atto 488 | Sigma-Aldrich | Cat# 49409 |
| Phalloidin-iFluor 647 Reagent - CytoPainter | AbCam | Cat# ab176759 |
| Bovine Serum Albumin (BSA), fatty acid-free powder | Fisher Bioreagents | Cat# BP9704-100; CAS#9048-46-8 |
| (+)-Biotin N-hydroxysuccinimide ester | Sigma-Aldrich | Cat# H1759; CAS#35013-72-0 |
| Alexa Fluor 568 carboxic acid, succinimidyl ester | Molecular Probes | Cat# A20003 |
| Alexa Fluor 488 carboxic acid, succinimidyl ester | Molecular Probes | Cat# A20000 |
| Atto 647 NHS ester | Sigma-Aldrich | Cat# 07376 |
| Hoechst 33342, Fluorescent Dye for labeling DNA | Tocris | Cat# 5117; CAS#23491-52-3 |
| Slide-A-Lyzer MINI Dialysis Device, 7K MWCO, 0.1 mL | Thermo Fisher | Cat# 69560 |

| | | |
|---|---|---|
| Rho Activator II | Cytoskeleton, Inc. | Cat# CN03-A |
| Soybean Trypsin Inhibitor | ATCC | Cat# 30-2104 |
| Hepes (1M) | Thermo Fisher Scientific | Cat# 15630080 |
| Phosphate Buffered Saline (PBS) pH 7.4 (1×) | Thermo Fisher Scientific | Cat# 10010023 |
| Penicillin Streptomycin Solution, 100X | Corning | Cat# 30-002-CI |
| DMEM, 1× (Dulbecco's Modification of Eagle's Medium) with4.5 g/L glucose, L-glutamine & sodium pyruvate | Corning | Cat# 10-013-CV |
| HyClone Cosmic Calf Serum, US Origin, 500 mL, Heat-inactivated | Cytiva | Cat# SH30087.03HI |
| RPMI 1640 with L-glutamine | Corning | Cat# 10-040-CV |
| EasySep Human CD4+ T Cell Isolation Kit | STEMCELL Technologies, Inc., USA | Cat# 17952 |
| EasySep Mouse CD8+ T Cell Isolation Kit | STEMCELL Technologies, Inc., USA | Cat# 19853 |
| ImmunoCult Human CD3/CD28/CD2 T Cell Activator | STEMCELL Technologies Inc., USA | Cat# 10970 |
| Dynabeads Mouse T-Activator CD3/CD28 | Thermo Fisher Scientific | Cat# 11456D |
| "The Big Easy" EasySep Magnet | STEMCELL Technologies, Inc., USA | Cat# 18001 |
| MojoSort Human CD4 Nanobeads | BioLegend | Cat# 480014 |
| GE Healthcare Ficoll-Paque PLUS Media | Thermo Fisher Scientific | Cat# 45-001-750 |
| Ammonium-Chloride-Potassium (ACK) Lysing Buffer | VWR International | Cat# 118-156-101 |
| Dynabeads Human T-Activator CD3/CD28 for T Cell Expansion and Activation | Gibco | Cat# 11132D |
| CTS Immune Cell SR | Gibco | Cat# A2596101 |
| Recombinant Human IL-2 (rhIL-2) | PeproTech | Cat# 200-02 |
| Recombinant human IL-7 (rhIL-7) | PeproTech | Cat# 200-07 |
| Recombinant human IL-15 (rhIL-15) | STEMCELL Technologies, Inc., USA | Cat# 78031 |
| CTS OpTmizer T Cell Expansion SFM | Gibco | Cat# A1048501 |
| L-glutamine (200mM) | Gibco | Cat# 25-030-081 |

| | | |
|---|---|---|
| EmbryoMax Penicillin-Streptomycin Solution, 100X | Sigma-Aldrich | Cat# TMS-AB2-C |
| ImmunoCult-XF T Cell Expansion Medium | STEMCELL Technologies, Inc., USA | Cat# 10981 |
| ImmunoCult Human CD3/CD28/CD2 T Cell Activator | STEMCELL Technologies, Inc., USA | Cat# 10990 |
| Human Recombinant IL-2, ACF | STEMCELL Technologies, Inc., USA | Cat# 78145.1 |
| 0.01% poly-L-lysine | Sigma-Aldrich | Cat# P4707; CAS#25104-18-1 |
| **Experimental Models: Cell Lines** | | |
| Human CD4+ T cells (derived from commercially supplied human whole peripheral blood). | STEMCELL Technologies, Inc., USA | Cat#70507.1 |
| Human CD8+ T cells (derived from commercially supplied human whole peripheral blood). | STEMCELL Technologies, Inc., USA | Cat#70507.1 |
| NK-92 cells | ATCC, USA | CRL-2407 |
| Human MDA-MB231 cells | ATCC, USA | HTB-26 |
| **DNA constructs** | | |
| pEGFP-C2_SEPT9 i1 | Addgene | Cat# 71609 |
| **Software and Algorithms** | | |
| KaleidaGraph 5 for MacOS | http://www.synergy.com/ | RRID:SCR_014980 |
| GraphPad Prism 7b | https://www.graphpad.com/ | RRID:SCR_002798 |
| PlotsOfData | https://huygens.science.uva.nl | N/A |
| Adobe Illustrator CC, 21.0.0. | Adobe Systems, Inc. | RRID:SCR_010279 |
| NanoScope Analysis 1.7 | Bruker | |
| MATLAB R2019a | The MathWorks | |
| LAS X | Leica Microsystems | |
| Fiji | https://imagej.net/software/fiji/ | |
| MedusaDock | https://dokhlab.med.psu.edu/cpi | N/A |
| Chiron | https://dokhlab.med.psu.edu/chiron | N/A |
| **Other** | | |
| AFM Tipless Probe | MikroMasch (µMasch), Germany | Cat# HQ:CSC38/tipless/Cr-Au, HQ:CSC38/tipless/Al BS |
| Instant Structured Illumination (iSIM) microscopy system | VisiTech Intl., Sunderland, UK | |

| | | |
|---|---|---|
| Leica SP8 laser scanning confocal microscopy imaging system | Leica Microsystems https://www.leica-microsystems.com/ | |
| TokaiHit Stage Top Incubator, Model STXG-GSI2X-SET | Tokai Hit, Fujinomiya, Japan | |
| Leica DMi8 system | Leica Microsystems https://www.leica-microsystems.com/ | |
| Bruker Bioscope Catalyst Atomic Force Microscope System | Bruker https://www.bruker.com/en/meta/search.html?q0=resolve | |

**Cell experiments**

We maintained human MDA-MB-231 cells (ATCC® HTB-26™) in DMEM with 4.5 g/L D-glucose, L-glutamine,110 mg/L sodium pyruvate (Corning Cellgro®, Cat# 10013CV) and 10% heat-inactivated FBS (HyClone®, Cat# SH30071.03H) at 37ºC in 5% CO2.

Primary human CD4+ and CD8+ T cells were isolated from commercially available whole human blood (STEMCELL Technologies Inc., USA, Cat# 70507.1) with EasySep Human CD4+ or CD8+ T Cell Isolation Kits (STEMCELL Technologies Inc., USA). Unless otherwise indicated, cells were cultured, activated and expanded in ImmunoCult-XF T Cell Expansion Medium (STEMCELL Technologies Inc., USA) with the addition of ImmunoCult Human CD3/CD28/CD2 T Cell Activator and Human Recombinant Interleukin 2 (IL-2, STEMCELL Technologies Inc., USA) as per STEMCELL Technologies Inc. commercial protocol, at 37ºC in 5% CO2.

NK-92 (ATCC®, CRL-2407™) were cultured in the ImmunoCult-XF T Cell Expansion Medium (STEMCELL Technologies Inc., USA) with the addition of Human Recombinant Interleukin 2 (IL-2, STEMCELL Technologies Inc., USA).

Cells were treated either in 6.5 mm Transwell® plates with 3.0 µm pore polycarbonate membrane inserts (Corning, Cat# 3415) or in glass-bottom 35 mm Petri dishes (MatTek Corp., Cat# P35G-1.5-14-C) using dimethyl sulfoxide (Sigma, Cat# 472301), (-)-Blebbistatin enantiomer (Sigma, Cat# 203391), Dynapyrazole A (Sigma, Cat# SML2127), Paclitaxel (Sigma, Cat# T7402), Calyculin A (Sigma-Aldrich, Cat# 208851), Tubacin (Sigma-Aldrich, Cat# SML0065), and septin inhibitor UR214-9 (synthesized by Dr. Rakesh K. Singh) as indicated in the main text.

Transfection of MDA-MB-231 cells with pEGFP-C2_SEPT9 i1 (Addgene Cat# 71609) was performed in Opti-MEM (Gibco, Cat# 31985-070) using SuperFect reagent (Qiagen, Cat# 301307) according to the manufacturer's protocol.

**High precision micropatterning**

An instructive and detailed protocol for indirect, high-definition, submicron-scale polyacrylamide gels micropatterning with various proteins is described in the original report (Tabdanov et al., 2020). Briefly, collagen type-1 micropatterning at the micron- and submicron scale spatial precision is technically complicated by the capillary and van-der-waals effects that routinely induce a collapse of the microstamp bas-reliefs, made of conventional soft regular PDMS (rPDMS, polydimethylsiloxane), onto the printed glass surface. In order to preclude the microstamps from undesirable collapsing we replaced rPDMS stamping

bas-relief with a 0.5-0.8 mm-thick veneering microprinting surface, *i.e.* - hard PDMS (hPDMS) (Schmid and Michel, 2000; Tabdanov et al., 2018b), mounted on the 5-8 mm-thick cushioning rPDMS blocks. To cast the micro-printing surfaces from the commercially fabricated and passivated molding matrix of desirable design (Minnesota Nano Center, University of Minnesota), we coated molds with 0.5-0.8 mm-thick layer of hPDMS either manually with a soft paraffin spatula or on a spin coating device. The submillimeter hPDMS layer on the silicone molding matrix was then cured in a heat chamber (70ºC, 30 minutes). Next, an ~8 mm-thick layer of bubble-free rPDMS was cured atop of the hPDMS layer (rPDMS; 1:5 curing agent/base ratio, Sylgard-184, Dow Corning, 70ºC for ~1 hour). The cured micro-stamping composite was then peeled off the mold and cut into 1×1 cm pieces for the further use.

In order to assemble the elastic ICAM1 or collagen type-1 micro-patterns, we first microprinted α-Fc FAB antibody fragment (Jackson Immunoresearch, USA, Cat# 109-007-008, RRID:AB_2632440) or α-collagen-1 rabbit pAb (AbCam, Cambridge, UK, Cat# ab34710; RRID:AB_731684) on clean "intermediate" glass surface, stripped from organic impurities by the prolonged thermal treatment (FisherFinest™ Premium Cover Glass; #1, Cat# 12-548-5 P; 450ºC, baked 20 hours in the furnace). For that, the cognate antibody for collagen-1 or an antibody fragment for ICAM-1-hFc were covalently conjugated with biotin, ((+)-biotin *N*-hydroxysuccinimide ester, Sigma-Aldrich, Cat# H1759; as per the manufacturer's protocol) and a fluorescent Alexa Fluor tag (Alexa Fluor® succinimidyl esters, Invitrogen™, Molecular Probes®, Cat# A20000, Cat# A20003; as per commercial protocol). For that, the micro-stamps were coated with the 0.2 mg/mL α-collagen-1 antibody (or anti-Human Fc FAB) PBS solution for 40 min at 37ºC in a dark humid chamber, then gently rinsed in deionized water, and dried under a jet of argon or nitrogen immediately prior to the micro-contact soft lithography procedure. Second, glass-bottom 35 mm cell culture dishes (MatTek Corp., Ashland, MA, Cat# P35G-1.0-20-C) were activated with 3-(trimethoxysilyl)propyl methacrylate (Sigma-Aldrich, Cat# 6514, as per commercial protocol) to ensure the covalent crosslinking between the glass surface and PAA gels. Third, 5 µL of PAA premix (polyacrylamide, see the "PAA elastic gel premix" section) of the projected rigidity G' = 50 kPa(Plotnikov et al., 2014a) with the addition of the 5% streptavidin-acrylamide (ThermoFisher, Cat# S21379) were, avoiding any air bubbles formation, carefully 'sandwiched' between the activated glass surface and the micropatterned intermediate glass surface promptly after adding a curing catalyst (aminopropyltriethoxysilane, APS). The resulting 'sandwiches' with cured PAA were then incubated in deionized water (1 h, 20ºC) for hypotonic PAA swelling that ensures gentle coverglass release from PAA gel. The resulting dish-bound PAA gels were checked for quality of the transferred fluorescent micropatterns on an epifluorescent microscope. Lastly, the anti-Human Fc FAB patterns on PAA were incubated with 10 µg/mL ICAM1-hFc solution (Sino Biological, Cat# 10346-H03H-50) and α-collagen-1 Ab micropatterns on PAA gels were incubated with 1 mg/mL rat monomeric collagen-1 (Corning, NY, Cat# 354249) in cold PBS (4 °C, 12 hours), then rinsed three times with cold PBS, and utilized for experiments.

**hPDMS formulation**

To prepare the hPDMS mixture we used 3.4 g of VDT-731 (Gelest, Inc., Cat# VDT-731), 18 µL of Pt catalyst (Platinum(0)-2,4,6,8-tetramethyl-2,4,6,8-tetravinylcyclotetrasiloxane complex solution) (Sigma-Aldrich, Cat# 479543), and one drop of cross-linking modulator 2,4,6,8-Tetramethyl-2,4,6,8 -tetravinylcyclotetrasiloxane (Sigma-Aldrich, Cat# 396281). All components were thoroughly mixed in a 50 mL conical bottom centrifuge tube on the vortex mixer for at least 30 sec. Before use, we added 1 g of HMS-301 (Gelest, Inc., Cat# HMS-301) to the mixture, promptly mixed it for 30 sec on a vortex mixer, degassed in a high-speed centrifuge (3 minutes, 3000 rpm), and immediately used it for the mold coating. The detailed protocol is described elsewhere (Odom et al., 2002; Schmid and Michel, 2000).

### PAA elastic gel premix

For PAA premixes, we utilized 40% acrylamide (40% AA) base (BioRad, Cat# 161–0140) and 2% bis-AA (BioRad, Cat# 161–0142) cross-linker as described elsewhere.(Fischer et al., 2012; Plotnikov et al., 2014b) Additionally, streptavidin-acrylamide (Thermo Fisher, Cat# S21379) was added to the final concentration of 0.133 mg/mL to enable PAA gels cross-linking with biotinylated proteins of interest for the micropatterns transfer from the intermediate glass surface to the cured PAA gels. Briefly, for preparation of 50 µL of G' = 50 kPa PAA gel premix, the components were mixed as follows: 40% AA - 15 µL; 2% bis-AA - 14.40 µL; 2 mg/mL streptavidin-acrylamide - 3.33 µL; 10X PBS - 5 µL; deionized milli-Q water - 11.17 µL; TEMED - 0.1 µL. The premix solutions were degassed and stored at 4ºC before use. To initiate curing, 1 µL of 10% APS was added to 50 µL of PAA premix immediately before the PAA gel casting procedure.

### Polymerization of prestained collagen gels

To prepare 3 mg/ml collagen-I gel, we assembled a gel premix on ice in a prechilled Eppendorf tube. To 1 volume of CellAdhere™ type I bovine, 6mg/mL (STEMCELL Technologies Inc., USA) we added 8/10 volume of DMEM, 1/10 volume of 10x PBS, 1/20 volume of 1M HEPES, and 1/20 volume of 1M Atto 647 NHS Ester (Sigma-Aldrich). A drop of premixed gel (~50ul) was spread immediately on a glass surface of a plasma-treated glass-bottom 35 mm Petri dish (MatTek Corp., Cat# P35G-1.5-14-C) with a pipette tip. During polymerization (room temperature, for overnight), gels were covered with 1mL of mineral oil (Sigma-Aldrich, Cat# M8410) to prevent evaporation of water. Before adding T cells, polymerized gels were rinsed with PBS to remove the unpolymerized gel components.

### Transwell assay

We coated plasma-treated polycarbonate membranes (Corning, Cat# 3415) with 100 µl of 10 µg/mL ICAM1 PBS solution (Sino Biological, Cat# 10346-H03H-50) overnight at 4ºC. Before loading cells (100 µl, 10^5 cells), we rinsed inserts twice with PBS. During the transwell assay, T cells on the upper surface of a permeable membrane of a cell culture insert migrate across pores to the collecting bottom chamber (600 µl). Following an incubation period (6 hours), we fixed cells by adding 600 µl of ice-cold (4ºC) DMEM containing 4% paraformaldehyde (Sigma-Aldrich, Cat# P6148) and 1:1000 Hoechst (Tocris, Cat# 5117) overnight, and counted the cells that migrated through the membrane. We do not use any additional chemoattractant gradient, similarly to prior work(Tooley et al., 2009), since the chemoattractant concentration quickly equalizes between the compartment below the membrane and the compartment above the membrane due to the pore size.

### Synthesis of UR214-9

Equimolar mixture of 3-amino-2-fluorobenzotrifluoride (Combi-Blocks, Cat#QA-4188) and 2,6-dichloro-4-isocyanatopyridine (Toronto Research Chemicals, cat#159178-03-7) were stirred and heated in anhydrous Toluene at 85ºC overnight. The separated UR214-9 was filtered and dried under vacuum in a dessicator. A portion of UR214-9 was detected in the Toluene layer, which was concentrated and purified by thin-layer chromatography using ethyl acetate and hexane as eluents. The pure product band was scrapped off the glass plate and UR214-9 was stripped from the silica gel using DCM+MeOH through a sintered funnel. The solvent was evaporated using a Buchi rotary evaporator to obtain UR214-9 as an off-white powder. The structure was confirmed by X-ray crystallography.

### Super- and high-resolution and confocal imaging

Cells were fixed with ice-cold (4ºC) DMEM containing 4% paraformaldehyde (Sigma-Aldrich, Cat# P6148) for 20 minutes. PFA-fixed samples were rinsed in 1% BSA in PBS two or three times (5 minutes for each

cycle), followed by 30 minute-long blocking-permeabilization treatment in 0.1% Triton X-100 (Sigma-Aldrich, Cat# T8787) solution with 10% BSA (Fisher, Cat# BP9704) in PBS (Thermo Fisher, Cat# 10010023). For immunofluorescence sample staining, we utilized primary antibodies diluted in 1% BSA PBS (all catalog numbers of antibodies are listed in Key Resources Table). The duration of the incubation with any of the listed primary antibody solutions was 1 hour at room temperature. Similarly, labelings with Alexa-Fluor-conjugated secondary antibodies (Thermo Fisher) were performed at their final concentration of 5 μg/mL for the duration of 1 hour in 1% BSA PBS at room temperature. After washing out the excess secondary antibodies, F-actin was stained either with fluorescent phalloidin or SIR-Actin for the duration of 1 hour. Chromatin was labeled with 1:1000 Hoechst solution (Tocris, Cat# 5117) added to the mounting 90% Glycerol (Sigma, Cat# G5516) in PBS media.

High-resolution 3D and 2D imaging for cell morphometric analysis were performed on a Leica TCS SP8 laser scanning confocal microscope with LIAchroic Lightning system and LAS X Lightning Expert super-resolution capacity, 405, 488, 552 and 638 nm excitation diode lasers, with 40×/1.3 oil immersion objective (Leica, Germany). The scanning settings were optimized with Nyquist LAS X function with HyD2.0-SMD excitation sensors, at the regular pinhole size of 0.85 AU, and the scanning frequency at 100 Hz. Each frequency channel was scanned in sequence in order to avoid the signal bleeding between the channels. Additionally, live cell imaging microscopy experiments were performed on epifluorescent Leica DMi8 microscope (Leica, Germany) equipped with a temperature (37ºC), $CO_2$ (5%), and humidity-controlled chamber at 20×, 40X and 63X magnifications. Brightfield and fluorescence time-lapse images were obtained using LAS X software (Leica, Germany).

Super-resolution 3D and 2D imaging was performed using an Instant structured illumination microscopy (iSIM). The custom built instant structured illumination microscope system (VisiTech Intl, Sunderland, UK) was equipped with an Olympus UPLAPO-HR ×100/1.5 NA objective, two Flash-4 scientific CMOS cameras (Hamamatsu, Corp., Tokyo, Japan), an iSIM scan head (VisiTech Intl, Sunderland, UK), and a Nano-Drive piezo Z stage (Mad City Labs, Madison, WI). The iSIM scan head included the VT-Ingwaz optical de-striping unit. Image acquisition and system control was done using MetaMorph Premiere software (Molecular Devices, LLC, San Jose, CA). Images were deconvolved with an iSIM-specific commercial plugin from Microvolution (Cupertino, CA) in FIJI.

All analyses were performed automatically and/or manually utilizing Leica LAS X software (Leica, Germany) and the ImageJ/FIJI. Figures were composed using unmodified LAS X -generated TIFF images with Adobe Illustrator CC 2021 (Adobe).

**Atomic Force Microscopy**

Depending on the pharmacological drug treatment, immune cells were incubated in Immunocult-XF culture media with the respective drug concentration (Blebbistatin: 50 μM, UR2149: 50 μM, Taxol: 1 μM, Latrunculin A: 100 nM) for the given treatment condition for total times between ~15 min to 75 min. The cells were incubated in Eppendorf tubes with their respective drug concentrations, followed by plating on a glass-bottom dish (WillCo Wells) precoated with 0.01% poly-L-lysine (Sigma-Aldrich). Plating was done ~15 minutes before imaging to allow cells to weakly adhere to the glass-bottom dish surface and the drug to take maximum effect. AFM force spectroscopy experiments were performed using a Bruker BioScope Catalyst AFM system (Bruker) mounted on an inverted Axiovert 200M microscope (Zeiss) equipped with a confocal laser scanning microscope 510 Meta (Zeiss) and a 40x objective lens (0.95 NA, Plan-Apochromat, Zeiss). The combined microscope instrument was placed on an acoustic isolation table (Kinetic Systems). During AFM experiments, cells were maintained at physiologically relevant temperature 37°C using a heated stage (Bruker). A soft silicon nitride tipless AFM probe (HQ:CSC38/tipless/Cr-Au,

HQ:CSC38/tipless/Cr-AlBS, MikroMasch) was used for gentle compression of spherical weakly-adherent cells. The AFM microcantilevers were pre-calibrated using the standard thermal noise fluctuations method, with estimated spring constants for microcantilevers used between 0.04–0.12 N/m. Immediately after probe pre-calibration, the AFM tipless probe was moved on top of a spherical cell. Five to ten successive force curves were performed on each cell. The deflection setpoint was set between 4-12 nm yielding applied forces between 0.16 to 1.44 nN.

All AFM force-distance curves measurements were analyzed using a custom-written MATLAB (The MathWorks) code to calculate the cellular surface cortical tension. For curve fitting, indentation depths between 0-600 nm were relatively consistent in yielding good fits (R2>0.75). Curves with poor fits R2<0.75 were discarded from the analysis. Additionally, we discarded noisy force curves and/or curves that presented jumps possibly due to cantilever and plasma membrane adhesion, slippage, or very weakly adhered moving cells.

Spherical cell cellular surface cortical tension (*T*; pN/μm) was calculated by fitting each recorded force-distance curve using the cortical tension method previously described that defines the force balance relating the applied cantilever force with the pressure excess inside the rounded cells and the corresponding actin cortex tension; $T = \frac{k_c}{\pi}\left(\frac{1}{(z/d)-1}\right)$, where *T* is the cellular surface tension, $k_c$ is the AFM cantilever spring constant, *z* is the Z-piezo extension, and d is the cantilever mean deflection.(Cartagena-Rivera et al., 2016)

### *In silico* UR214-9-Septin docking energy simulation

Swiss-Model (Schwede et al., 2003), a homology modeling based protein structure prediction tool, was used to model the structures of Septin 2, 6, 7, and 9. Since these septins have crystal structures, Swiss-Model was mainly used to complete the missing residues and atoms. Particularly, Septin 2, 6, 7, and 9 were modeled by using 6UPA, 6UPR, 6N0B, and 5CYO as the templates for homology modeling. The dimer structure of each of the septins is built by aligning two monomer structures to the corresponding positions in 2QAG, which is a septin oligomer structure. Next, the dimer structures were optimized by using Chiron (Ramachandran et al., 2011). Two pockets were identified according to the positions of the ligands in 2QAG. The two pockets are at the dimerization interface of the dimer structures. MedusaDock (Ding et al., 2010; Wang and Dokholyan, 2019) was used to dock GTP, GDP, UR214-9, and FCF to the dimer structures of the septins. Docking poses were evaluated by MedusaScore, (Yin et al., 2008) a scoring function based on a custom physics-based force field. 1000 docking attempts were performed for each of the protein-ligand pairs, and the resulting docking poses were clustered by MedusaDock to select the centroid as the final candidate.

### Automated detection and tracking of cells in collagen matrix

The detection of individual cells in phase-contrast time-lapse images was performed with the following steps. First, the variation of the background illumination across each image was corrected by subtracting the image smoothed by the Gaussian filter (with a standard deviation of 10 pixels) from the original image. Second, the resulting background-corrected images were processed with the local standard deviation (STD) filter (with the 9x9-pixel neighborhood matrix) to highlight cell edge regions. Third, the resulting STD maps were smoothed by the Gaussian filter (with a standard deviation of 5) to obtain gray-scale representation of cells. Next, the resulting images were re-scaled with log function and masked with a threshold value of 6.4. To identify individual cells, the resulting binary masks were overlaid with the smoothed STD maps and subjected to our in-house watershed segmentation routine (using an algorithm

that includes 'draining' criteria allowing to avoid over-segmentation (Hladyshau et al., 2021), which is typical for the traditional watershed approaches). Centroids of all 8-connected objects in the segmented images were recorded for tracking.

The tracking of cell centroids was performed based on minimal distance matching in the consecutive time frames (within the radius of 40 pixels). The tracking pipeline includes the following steps. If two or more trajectories meet (e.g., one of the cells moves over or under another cell in the 3D matrix), the new position is added to the longest up to the time point track while the other one(s) ends. If a trajectory splits (e.g., another cell moves into the focus plane from above or below the tracked cell in the 3D matrix), the nearest new position is added to the current track, while the other new position starts a new track. Because cells move in the 3D environment, it is possible for cells to come in and out of the focus plane, which leads to recording several shorter tracks of the same cell. Since we do not use trajectory length as a phenotype characteristic, the occasional fragmentation of trajectories does not affect our analysis. However, it is also possible that a cell migrates at the border of the focus plane, repeatedly coming in and out of focus (i.e., flickering) and creating multiple ultra-short tracks. To reduce such disruptions of individual cell tracks, we apply a 'flickering correction' algorithm (Tsygankov et al., 2014) that detects co-localization of the end of one trajectory ($x_e$,$y_e$) at time $t$ and the beginning of another trajectory ($x_b$,$y_b$) at time $t$+2 and merge these trajectories into one by assigning cell position at $((x_e+x_b)/2,(y_e+y_b)/2)$ at time $t$+1. Because we track cells with complex (ball-chain) shapes, it is possible for our detection algorithm to identify more than one compartment of the same cell as separate cells. As a result, a single cell may produce several nearly co-localized trajectories. To avoid a potential bias due to such double counting, we apply a 'cloning correction' algorithm that detects each trajectory remaining in the vicinity of another longer trajectory for the whole duration of this shorter track and removes such tracks from the record. Finally, we remove all the 'tracks' of immobilized debris in the image by disregarding trajectories that remain within the detection radius (40 pixels) for the entire track duration.

### Statistical analysis

Only pairwise comparisons as one-sided $t$ tests between a control group and all other conditions are utilized to analyze the data, as well as between paired -Blebbistatin and +Blebbistatin co-treatment groups. Statistical analysis is performed using either KaleidaGraph 5 for MacOS (Synergy Software) or Prism 7b (GraphPad Software, Inc). The exact p values are indicated on the plots, unless the $p<0.0001$, *i.e.* below the cut-off lower limit for Kaleidagraph and Prism software. Sample size n for each comparison is reported in the corresponding plots (*i.e.* n reflects the number of measured individual cells). Number of replicates is 3, unless specified otherwise. Data are shown as box and whiskers diagrams: first quartile, median, third quartile, and 95% percent confidence interval.

## CONFLICTS OF INTEREST

There are no conflicts of interest to declare.

## DATA AVAILABILITY STATEMENT

The authors declare that the data supporting the findings of this study are available within the paper, the supplementary information, and any data can be made further available upon reasonable request.

## ACKNOWLEDGEMENTS

E.D.T. and this work were supported by the Department of Pharmacology, Penn State College of Medicine *via* the startup funds. N.V.D. is supported by the NIH grant R35GM134864 and the Passan Foundation.

D.T. is supported by the National Science Foundation (CMMI 1942561) and the National Institutes of Health (R01GM136892). A.S.Z., X.M., and A.M. were supported by the FDA Intramural Research Program of the Center for Biologics Evaluation and Research. A.X.C.R. and C.S. were supported by the National Institutes of Health (NIH) Intramural Research Program in the National Institute of Biomedical Imaging and Bioengineering (NIH grant # ZIA EB000094) and by the NIH Distinguished Scholars Program. P.J.S received the support of Human Frontier Science Program (HFSP) RGP0032-2022 and Forschungszentrum Medizintechnik Hamburg (FMTHH, grant 04fmthh2021). We thank Christian Combs and Daniela Malide for the Light Microscopy Core support at the National Heart, Lung, and Blood Institute, NIH.

**MOVIES LEGENDS**

**Movie 1.** Brightfield live video-microscopy sequence of hCD4+ T cell migrating through 3D collagen type I matrix.

**Movie 2.** Fluorescent visualization of the hCD4+ T cell's nucleus passage (Hoechst, cyan) through the cytoskeletal ring (SiR-actin, yellow) that constitutes a key peristaltic translocation event during T cell's amoeboid locomotion within 3D collagen matrix (magenta).

**Movie 3.** F-actin-dense rings (side views, seen as bands, SiR-actin live staining, yellow) form a cortical tube that peristaltically channels the nucleus (blue) *via* amoeboid passage as seen in hCD4+ T cells.

**Movie 4.** Wide-field view of hCD4+ T cell migration on 2D (flat) ICAM1 parallel lanes micropattern during their transitioning from predominantly amoeboid 'random walk' towards a mesenchymal-like contact guidance mode after the addition of UR214-9 septin inhibitor.

**Movie 5.** Detailed zoom-in view of hCD4+ T cell mesenchymal-like contact guidance along ICAM1 micro-lanes.

**Movie 6.** Wide-field view of the hCD4+ T cells' contact guidance along ICAM1 micro-lanes during prolonged **+UR214-9** treatment (t > 1 hour).

**Movie 7.** hCD4+ T cells predominantly amoeboid 'random walk' meandering on the flat 2D ICAM1 grids.

**Movie 8.** UR214-9-induced hCD4+ T cells mesenchymal-like spreading and dendritization along the ICAM1 grid.

**Movie 9.** Non-responsiveness of UR214-9-induced mesenchymal-like hCD4+ T cell dendritic adhesion, spreading, and contact guidance dynamics to Blebbistatin-mediated suppression of actomyosin contractility.

**Movie 10.** Dynein contractility inhibition with Dynapyrazole A abrogates UR214-9-induced hCD4+ T cells mesenchymal-like adhesion, spreading, and migration along ICAM1 grids. *Note that the tested T cells are co-treated with UR214-9 and Blebbistatin to demonstrate dispensable status of actomyosin contractility during mesenchymal-like T cell contact guidance mode under UR214-9 treatment.*

**Movie 11.** Abrogation of hCD4+ T cell's UR214-9-induced mesenchymal-like adhesion, spreading, and migration with Dynapyrazole A-induced dynein inhibition (no Blebbistatin co-treatment). Following washout demonstrates partial reversibility of treatment effects.

**Movie 12.** Inhibition of the actomyosin contractility **(+Blebbistatin)**, unlike UR214-9 treatment, does not induce mesenchymal-like ‘dendritic’ cell spreading.

**Movie 13.** Sole inhibition of the dynein contractility **(+Dynapyrazole A)** does not change hCD4+ T cell predominantly amoeboid migratory behavior on ICAM1 grids.

# FIGURES

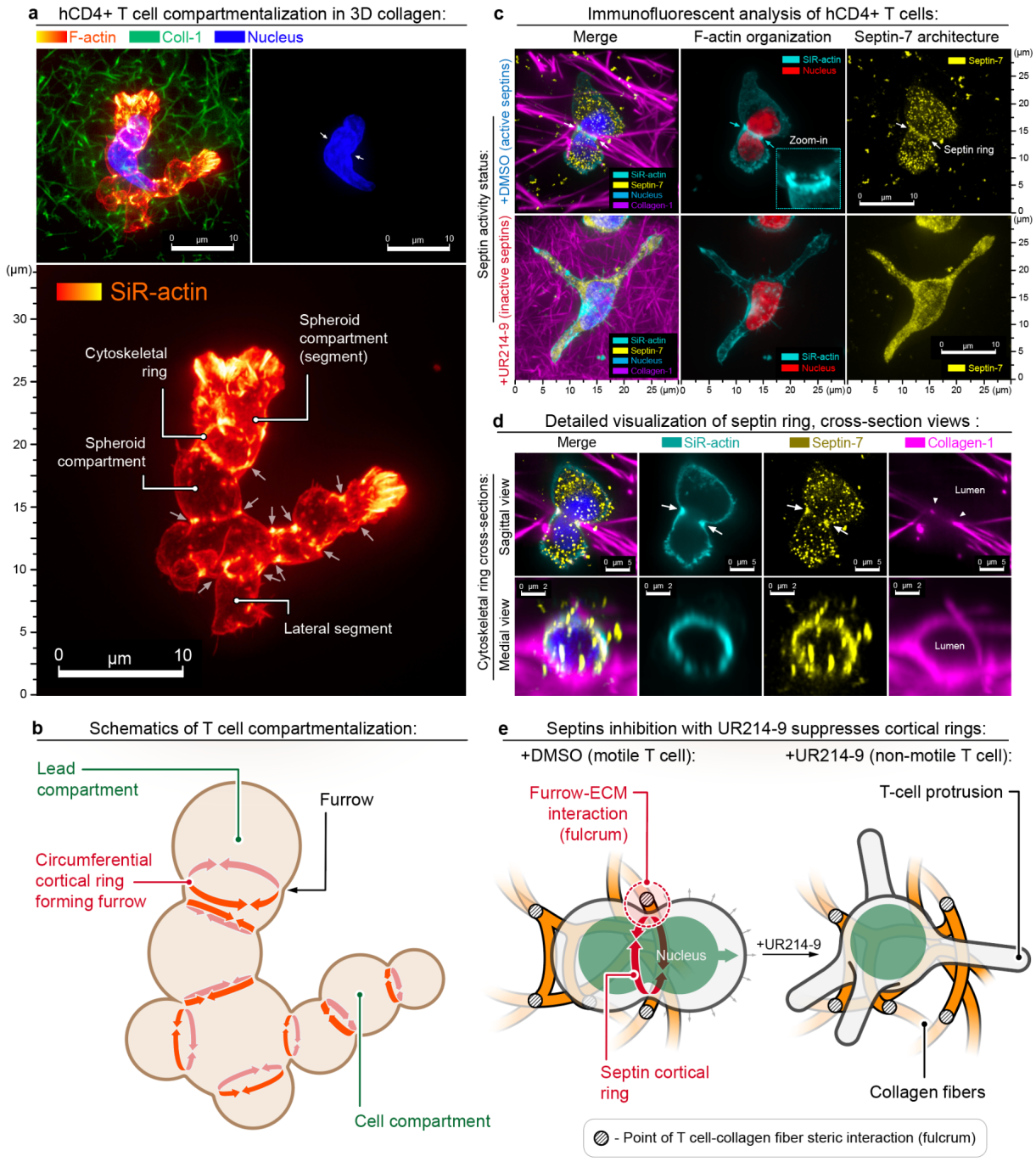


**Figure 1. Septins institute compartmentalization of the T-cell cortex during amoeboid migration.**

**(a)** Compartmentalization of the human CD4+ (hCD4+) T cell cortex into multiple spheroid segments during amoeboid migration through 3D collagen matrix (type I). Spheroid segments are separated by F-actin-enriched circumferential rings (SiR-actin staining for F-actin) that shape cortex (*arrows*) with the multiple circumferential furrows and indent a passing-through nucleus (*arrows*).

**(b)** Schematics of T cell compartmentalization. Newly formed cortical F-actin ring (circumferential furrow) separates an expanding cell segment (leading compartment) from the previously formed segments within the trailing 'ball chain'-shaped cell body.

**(c)** Immunofluorescence analysis of T cell migration in 3D collagen matrix:

*Top* - An hCD4+ T cell actively migrates in control conditions **(+DMSO)**, while displaying amoeboid compartmentalization with a septin-positive F-actin ring (Septin-7 immunofluorescence and SiR-actin staining, *arrows*). The migrating amoeboid T cell translocates its deformable nucleus through the cortical ring (*arrows*). *Note that in control T cells, immunofluorescence staining shows septin-7-enriched cytosolic vesicles.*

*Bottom* - upon septin inhibition **(+UR214-9)**, a migrating hCD4+ T cell loses amoeboid segmentation and the septin-positive cortical F-actin rings. Instead, the T cell acquires a non-migratory cell morphology, which is characterized by the formation of multiple elongated linear protrusions. *Note that UR214-9 also causes the loss of septin-enriched cytosolic vesicles (as shown by a diffuse septin-7 immunofluorescence staining).*

**(d)** Detailed transverse and sagittal cross-section views of the septin-enriched (septin-7 immunofluorescence) cortical rings in the migrating T cell (see **c**, *top*). *Note that the septin-positive cortical F-actin ring forms inside the confining collagen lumen (arrows).*

**(e)** Schematic representation of how an amoeboid T cell transitions to the non-migratory phenotype.

*Left* - An amoeboid T cell in the sterically complex microenvironments, *e.g.*, collagen matrix, forms a cortical ring (sterically interactive furrow) between the adjacent spheroid compartments of larger diameters **(+DMSO)**. During the amoeboid propulsion in 3D collagen, spatial configuration of adjacent segments provides a transient steric lock (fulcrum) between the cell and confining collagen fibers. The fulcrum mechanically supports peristaltic translocation of cytoplasm and nucleus without friction-loaded displacement of the entire T cell cortex.

*Right* - A T cell loses the amoeboid migration and cortical response (cortical F-actin ring) to the sterically complex microenvironment upon chemical suppression of septins' GTPase activity with UR214-9.

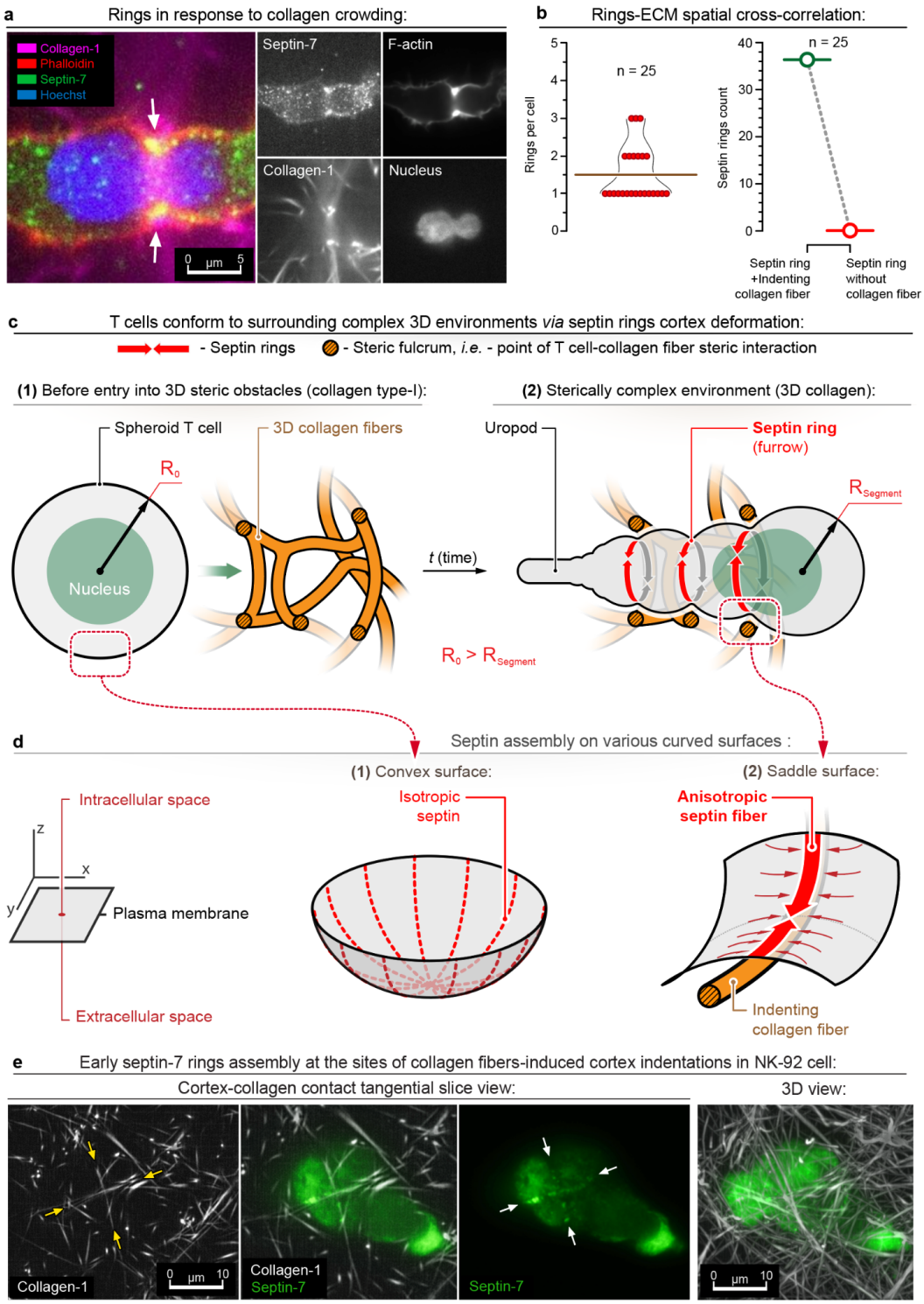


**Figure 2. 3D structure of the extracellular matrix guides the formation of septin-positive cortical rings.**

**(a)** Sagittal cross-section views of the amoeboid T cell migrating through the 3D collagen matrix. *Note that the septin-positive (septin-7) cortical ring forms at the site of the T-cell mechanical interaction (cell surface-indenting) with the collagen fibers (arrows).* The formation of the cortical ring at the indentation sites allows for cell compartmentalization and conformational adaptation to the complex configuration of the surrounding obstacles, as well as for the peristaltic translocation of the cytoplasm and nucleus along the sequence series of the resulting cell segments. *Note that the nucleus conforms to the surrounding cortical ring and collagen fibers.*

**(b)** Immunofluorescent analysis of spatial colocalization and cross-correlation for the cortical rings and cell surface-indenting collagen fibers.

*Left* - Distribution of the rings-per-cell counts (mean value ~1.5 ring/cell).

*Right* - Cortical rings are linked to the presence of cell surface-indenting ECM (collagen) fibers. *Note that rings are always associated with the adjacent collagen fiber (ring+collagen), while there is no identified T cell ring without a presence of a T-cell-indenting collagen fiber.*

**(c)** Schematic representation of the ECM-induced T cell transitioning from the non-migratory spheroid to the migratory compartmentalized architecture during its amoeboid migration through the sterically interactive 3D collagen gel. External 3D topography of collagen fibers meshwork surrounding an initially spheroid T cell **(1)** provides a guiding spatial configuration of the steric and mechanical pressure stimuli, to initiate a series of septin-driven T-cell compartmentalization events (**2**) required for amoeboid migration. Note that the resulting T cell's segment radii ($R_{Segment}$) are smaller than the radius ($R_0$) of the spheroid T cell.

**(d)** Schematic representation of septins assembly on the inner side of the T-cell plasma membrane surfaces with various curvatures. (**1**) - isotropic assembly of septin filaments on convex surface, *e.g.* in a spheroid cell. (**2**) - anisotropic assembly of septins on the saddle surface formed by a cell surface-indenting collagen fiber, *e.g.* initiation of the assembly of the compartmentalizing septin rings in a migrating T cell in response to the external obstacles.

**(e)** Tangential slice views of the amoeboid NK cell (NK-92 cell line) migrating through the collagen matrix. Early stage of septin-7 assembly (Septin-7 immunofluorescence, *green*) into the cortical ring starts at the sites of T cell surface indentation, caused by the T cell pressure against the collagen fibers *(arrows)*.

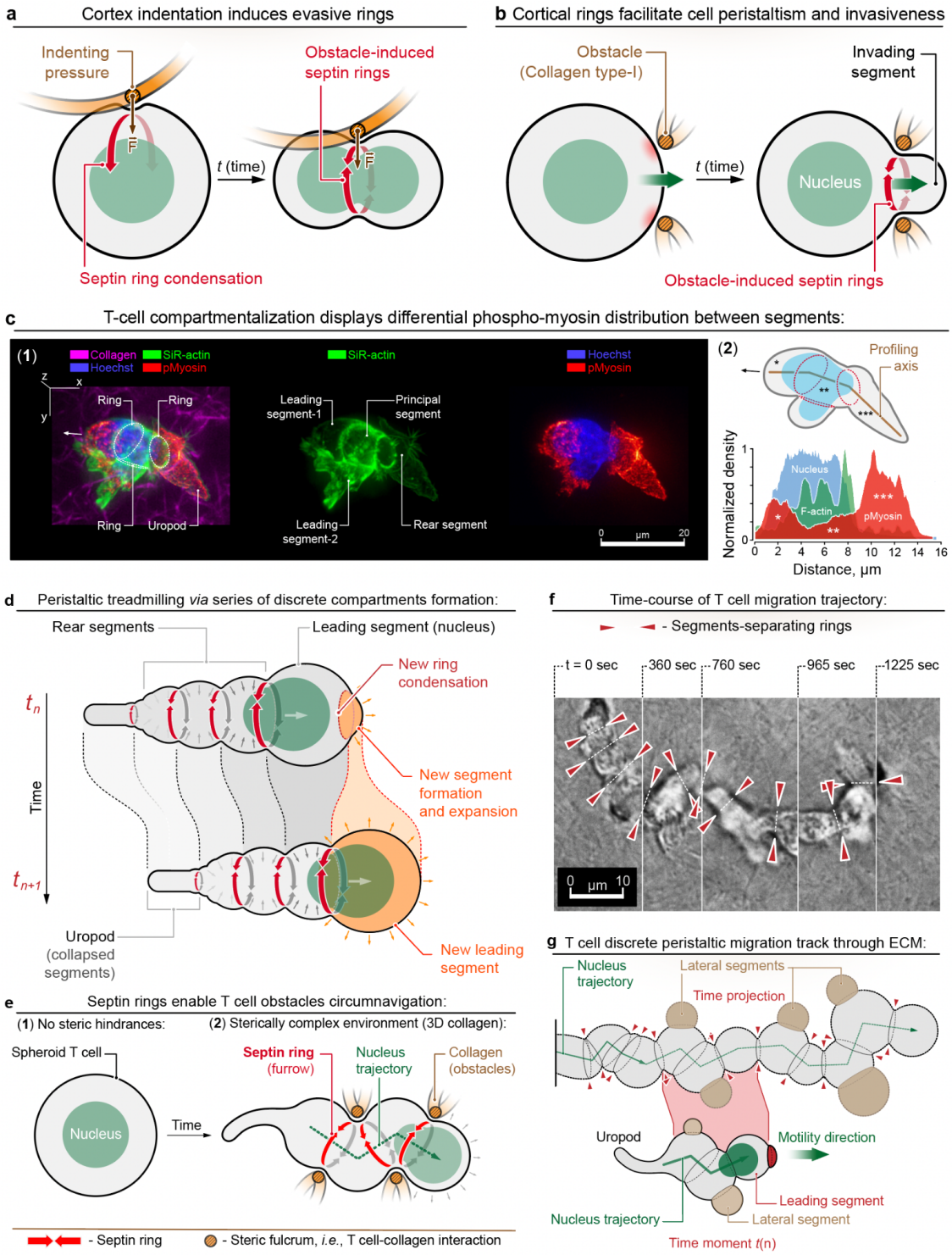


**Figure 3. Actomyosin cortex compartmentalization by localized formation of the septin rings in response to the external obstacles enables T cell peristaltic circumnavigation within complex 3D microenvironments.**

**(a)** Schematic representation of evasive cortex deformation, *i.e.* cortical ring, initiated by a cell surface-indenting collagen fibers. The spatial configuration of the resulting furrow forms a transient steric lock, *i.e.* fulcrum, onto indenting collagen fibers by virtue of cortical ring-induced 'hourglass' cell topography.

**(b)** Schematic representation of adhesion-independent invasive amoeboid propulsion. Collagen-induced cell partitioning initiates a stepwise peristaltic translocation of cytosolic content into the invading cell segment without friction-loaded displacement of the entire T cell cortex.

**(c)** (**1**) - 3D micrographic view of the hCD4+ T cell **(+DMSO)** in the collagen matrix. The T cell forms multiple rings and discrete contractile cell segments. *Note that the cortex in adjacent segments displays a differential density of phospho-myosin (phospho-myosin light chain 2 (Ser19) immunofluorescence), indicating that each individual cell segment may feature a different level of cortical contractility.* (**2**) - Cumulative density profiling for phospho-myosin light chain 2, F-actin and chromatin along the T cell's main axis, *i.e.* - across the principal segments. *Note that phospho-myosin peaks in the leading and the rear segments, but is depleted in the main (middle) nucleus-containing cell segment.*

**(d)** Schematic representation of amoeboid T cell migration by peristaltic treadmilling of discrete cell segments. Series of the new compartments formation at the leading front of the cell is accompanied by the nucleus and cytosol translocation **(Movies 1, 2 and 3)**.

**(e)** Schematic representation of T cell circumnavigation during amoeboid migration. Collagen fibers-induced septin rings deform the T cell cortex to conform to the surrounding obstacles. Treadmilling of the compartments and cytosol/nucleus peristaltic propulsion throughout the series of the obstacles-evading cortical rings allows T cells to efficiently circumnavigate around and between the structurally complex collagen matrix.

**(f)** Time course collage of the single hCD4+ T cell along its migration track within the 3D collagen matrix. Note the T cell forms multiple segments (chambers), separated by the rings (arrowheads) along the track of its migration. The T cell trajectory is a zigzag track between the chambers that are formed during the migration.

**(g)** Schematic representation of the spatiotemporal superposition of the migrating T cell - motility is driven by peristaltic translocation of the nucleus between segments, separated by the cortical rings (highlighted by arrowheads). Nucleus translocation forms the main zigzag track that reflects the directionality of the new leading segment formation, guided by the surrounding microenvironment steric configuration and topography. *Note that T cells also develop side branching pseudopods (lateral segments) that do not accommodate the nucleus and therefore do not become the leading segments.*

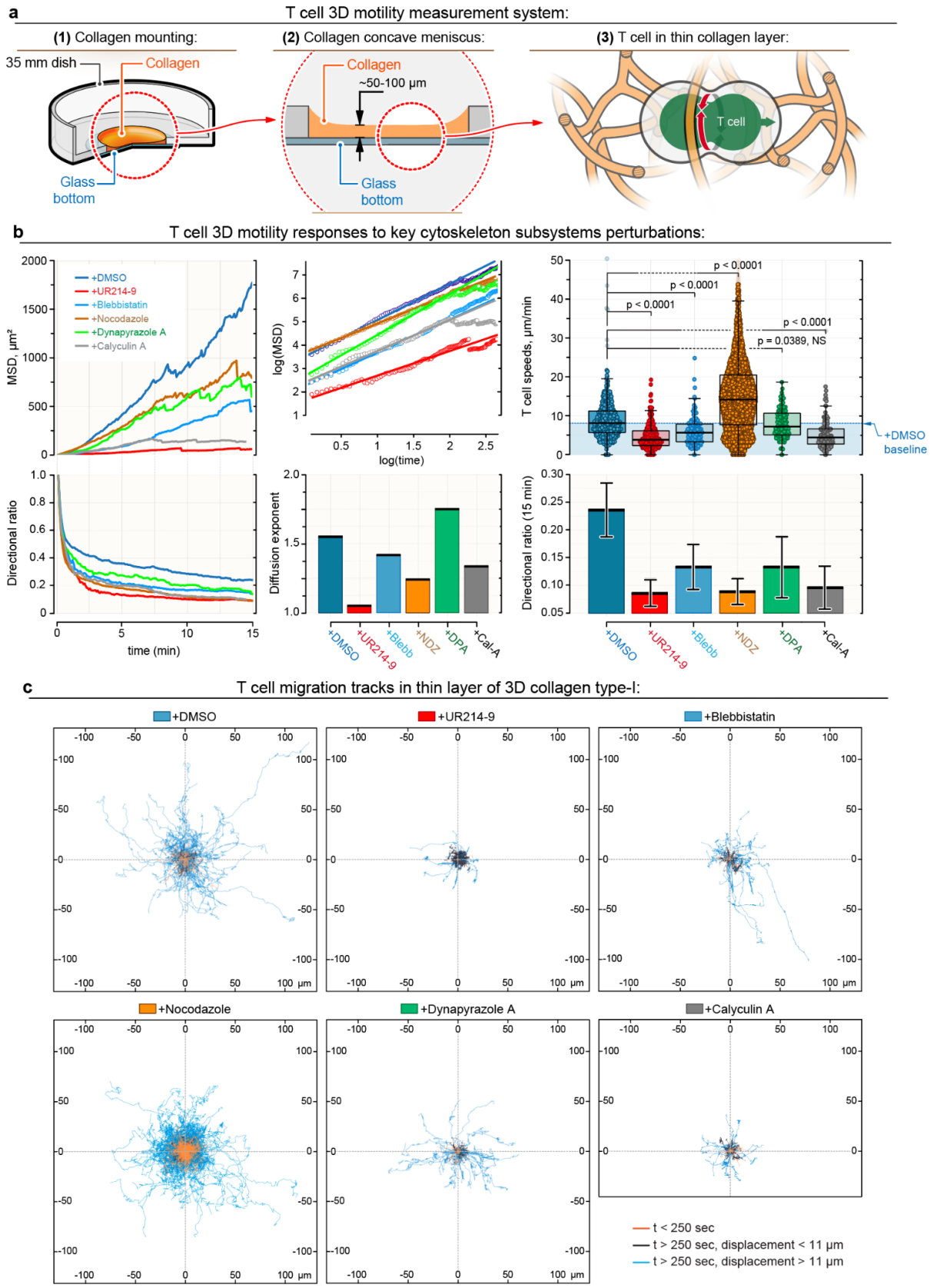
a
T cell 3D motility measurement system:
(1) Collagen mounting:
35 mm dish
Collagen
Glass bottom
(2) Collagen concave meniscus:
Collagen
~50-100 µm
Glass bottom
(3) T cell in thin collagen layer:
T cell
b
T cell 3D motility responses to key cytoskeleton subsystems perturbations:
+DMSO
+UR214-9
+Blebbistatin
+Nocodazole
+Dynapyrazole A
+Calyculin A
MSD, µm²
log(MSD)
log(time)
T cell speeds, µm/min
p < 0.0001
p = 0.0389, NS
+DMSO baseline
Directional ratio
time (min)
Diffusion exponent
Directional ratio (15 min)
+DMSO
+UR214-9
+Blebb
+NDZ
+DPA
+Cal-A
c
T cell migration tracks in thin layer of 3D collagen type-I:
+DMSO
+UR214-9
+Blebbistatin
+Nocodazole
+Dynapyrazole A
+Calyculin A
100 µm
t < 250 sec
t > 250 sec, displacement < 11 µm
t > 250 sec, displacement > 11 µm

**Figure 4. Perturbation of septins' GTPase activity arrests amoeboid migration of T cells within the 3D microenvironment.**

**(a)** Schematic representation of live cell imaging platform (**1**) used to measure motility of human CD4+ T cells in the 3D collagen matrix. Migrating T cells are imaged within a thin layer of collagen gel (**2**) and visualized in the planes positioned away from the glass (**3**).

**(b)** Responses of the characteristic motility parameters for human CD4+ T cells migrating within a 3D collagen matrix during perturbation of the key cytoskeletal subsystems: septins **(+UR214-9)**, microtubules **(+Nocodazole**, *i.e.* +NDZ**)**, non-muscle myosin contractility **(+Blebbistatin**, *i.e.* +Blebb, and **+Calyculin A**, *i.e.* +Cal-A**)**, and dynein contractility **(+Dynapyrazole A**, *i.e.* +DPA**)**. *Note that mean velocity values of automatically detected and tracked T cells do not reach zero due to the lack of sufficient T cells-collagen adhesion. Insufficient adhesion enables lymphocytes' passive oscillations (e.g. Brownian motion) within a 3D collagen matrix, which includes completely arrested T cells (e.g.* ***+UR214-9*** *or* ***+Calyculin A*** *treatments). Passive T cell oscillations do not result in the lymphocyte's persistent displacement within the collagen matrix.*

MSD - Mean Square Displacement is the population-wide average of the squared values of the linear distance between the T cell position at time $t$ and its initial position on the track ($t$ = 0). Displacement ratio is the population-wide average value of the ratios of the linear distance between the T cell position at time $t$ and its initial position on the track to the distance that T cell has traveled along its curved track up to time $t$. Note that a cell moving strictly along a line would have the Displacement ratio of one, while a cell wandering around its initial location would have the Displacement ratio close to zero. Thus, Displacement ratio is a metric of directional persistence. Diffusion exponent is the slope of the linear fit to MSD in log-log scale. Note that for a particle undergoing Brownian motion in 3D, MSD = $6Dt$, where $D$ is the diffusion constant. More generally, MSD can be approximated as MSD~$t^a$, so that in log-log scale, we have approximately linear dependence: log(MSD) = $a$ log($t$) + constant, where $a$ is the Diffusion Exponent. Thus, the Diffusion Exponent is a metric of the deviation of cell trajectories from the normal Brownian motion (superdiffusion/active transport for $a$>1 and subdiffusion for $a$<1).

**(c)** 2D projections of the human CD4+ T cell migration tracks within a thin layer of 3D collagen matrix during perturbation of the key cytoskeletal subsystems. *Note that both* ***+UR214-9*** *and* ***+Calyculin A*** *treatments induce potent arrest of T cell displacement, due to the complete loss of amoeboid cortical dynamics.*

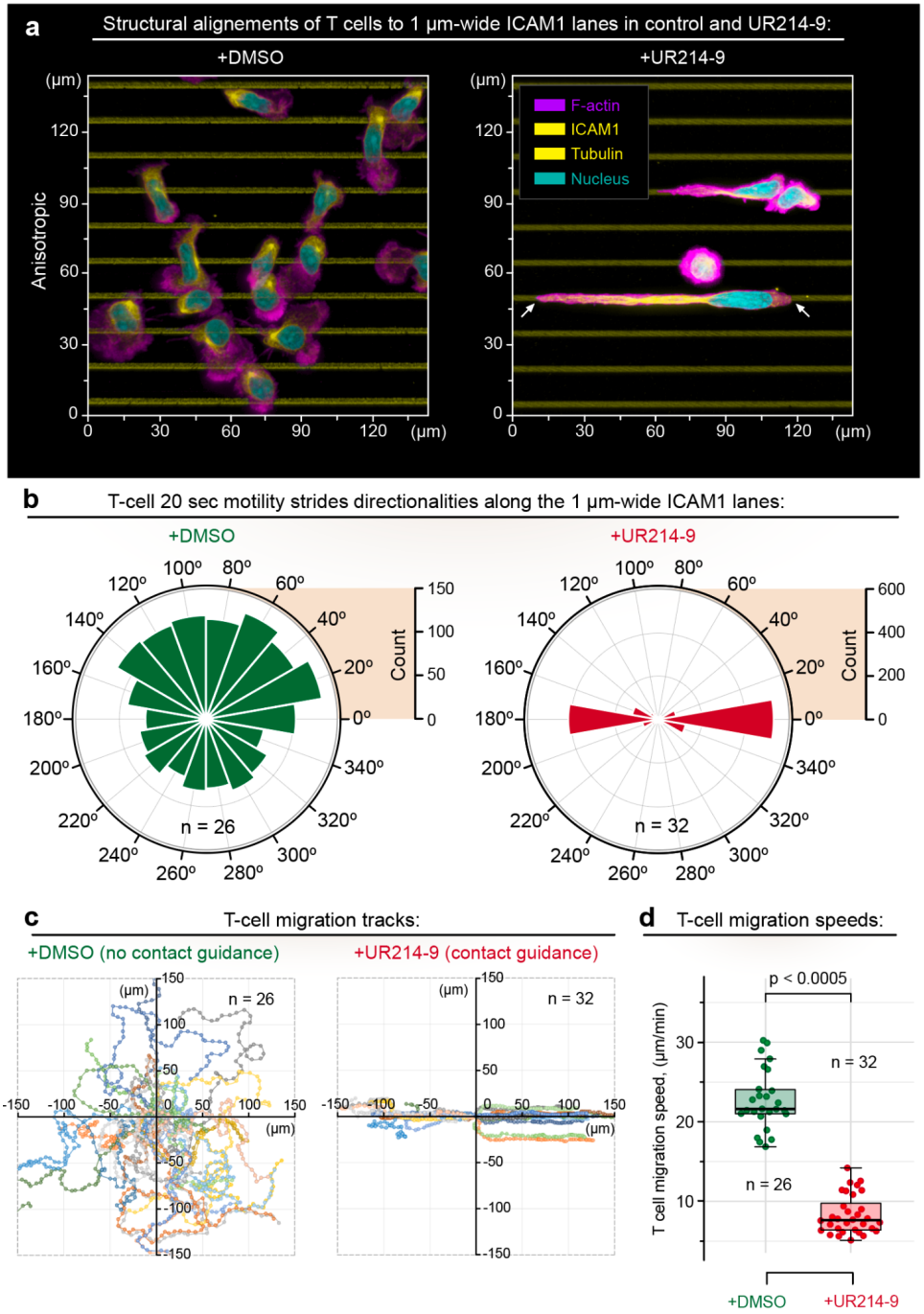


**Figure 5. Acute inactivation of septins induces amoeboid-to-mesenchymal-like phenotypic transition characterized by adhesion-guided cell spreading, slow migration mode and mesenchymal-like contact guidance.**

**(a)** hCD4+ T cells in control conditions **(+DMSO)** maintain amoeboid phenotype, featuring neither spreading nor alignment along the adhesion cues (ICAM1 anisotropic parallel lines, see **Movies 4 and 5 (before UR214-9)**). Septin inhibition **(+UR214-9)** induces phenotype transitioning towards mesenchymal-like behavior, which results in the prominent cell adhesion, alignment, and spreading along the ICAM1 lines **(Movies 4 and 5 (after UR214-9), Movie 6)**. Comparative analysis of migratory dynamics in control **(+DMSO)** and septin-inhibited **(+UR214-9)** T cells for: **(b)**

migration directionality, **(c)** individual cell migration tracks, and **(d)** migration speeds, indicates that septins inhibition leads to the transition towards extreme, mesenchymal-like migration and alignment to the contact guidance cues, characterized by high fidelity of the T cell migration tracks to the ICAM1 lines architecture, and accompanied with the significant loss of T cell migration speed, inherent to the mesenchymal migratory dynamics.

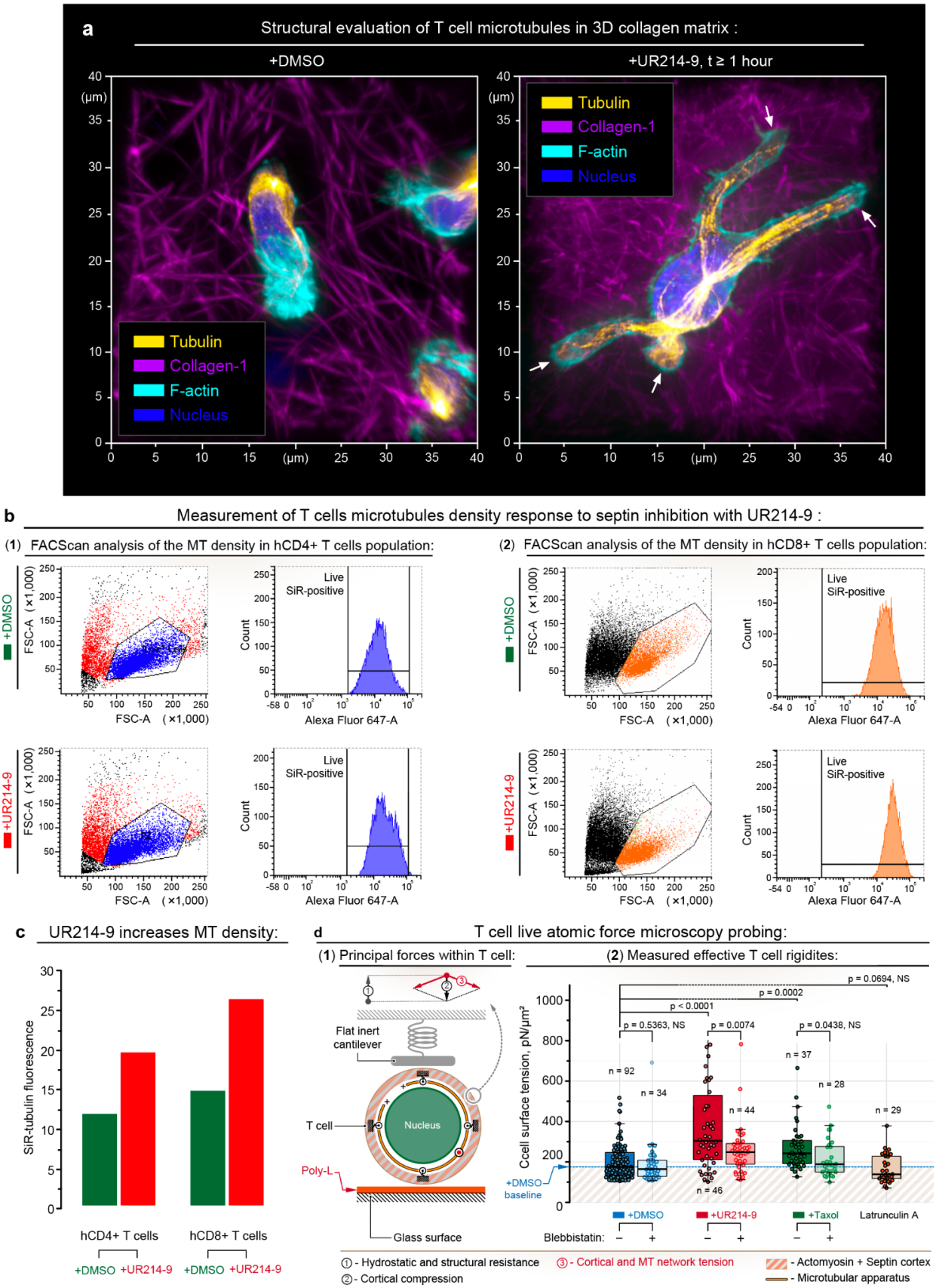
a
Structural evaluation of T cell microtubules in 3D collagen matrix :
+DMSO
+UR214-9, t ≥ 1 hour
Tubulin
Collagen-1
F-actin
Nucleus
(μm)
b
Measurement of T cells microtubules density response to septin inhibition with UR214-9 :
(1) FACScan analysis of the MT density in hCD4+ T cells population:
(2) FACScan analysis of the MT density in hCD8+ T cells population:
+DMSO
+UR214-9
FSC-A (×1,000)
Count
Live
SiR-positive
Alexa Fluor 647-A
c
UR214-9 increases MT density:
SiR-tubulin fluorescence
hCD4+ T cells
hCD8+ T cells
+DMSO +UR214-9
+DMSO +UR214-9
d
T cell live atomic force microscopy probing:
(1) Principal forces within T cell:
(2) Measured effective T cell rigidites:
Flat inert cantilever
T cell
Nucleus
Poly-L
Glass surface
Ccell surface tension, pN/μm²
+DMSO baseline
p = 0.5363, NS
p = 0.0074
p = 0.0438, NS
p < 0.0001
p = 0.0002
p = 0.0694, NS
n = 92
n = 34
n = 46
n = 44
n = 37
n = 28
n = 29
+DMSO
+UR214-9
+Taxol
Latrunculin A
Blebbistatin:
① - Hydrostatic and structural resistance
② - Cortical compression
③ - Cortical and MT network tension
- Actomyosin + Septin cortex
- Microtubular apparatus

**Figure 6. Inhibition of septin's GTPase activity increases the structural density of microtubular apparatus and mechanical rigidity of T cells.**

**(a)** Structural density and length of microtubules are increased (*arrows*) during septins inhibition **(+UR214-9**, t≥1 hour**)** in hCD4+ T cell within a 3D collagen matrix.

**(b)** FACScan flow cytometry analysis of the (**1**) hCD4+ and (**2**) hCD8+ T cells' microtubule density (*per cell*) as measured by the polymerized MT-specific SiR-tubulin live fluorescence (used as per commercial protocol, 1 hour incubation time).

**(c)** Population-wide mean values of MT density in hCD4+ and hCD8+ T cells during septin inhibition **(+UR214-9**, t≥1 hour**)** display 60% (hCD4+) and +90% (hCD8+) more of microtubule filaments per cell in comparison to the control T cells **(+DMSO)**.

**(d)** Atomic force microscopy shows rigidification of CD4+ T cells upon the build-up of microtubules which is induced by UR214-9-mediated septin inhibition. (**1**) - Schematic representation of the experimental settings and basic force configurations for live T cell mechanical probing. (**2**) - Measured T cell mechanical rigidities as the effective cell surface tension. Both UR214-9- and Taxol-induced microtubule stabilization result in the T cell rigidification.

*Note that suppression of actomyosin contractility with Blebbistatin co-treatment during **+UR214-9** or **+Taxol** treatments does not soften T cell down to the baseline level **(+DMSO)**, indicating the T cell rigidification is a combined effect of the cortical contractility and passive mechanical resistance of the enhanced microtubule apparatus. Note also that blebbistatin co-treatments do not result in the statistically significant T cell softening within all ±Blebbistatin co-treatment pairs (i.e. **±Blebbistatin**, **+UR214-9±Blebbistatin**, and **+Taxol±Blebbistatin**) due to the presence of the relatively large, mechanically resistant nuclei (~60-70% of T cell volume), and dense microtubules (**+UR214-9** and **+Taxol** treatments). Similarly, pharmacologically-induced disintegration of the F-actin network **(+Latrunculin A)** shows no statistically significant T cell softening due to the presence of the underlying nucleus.*

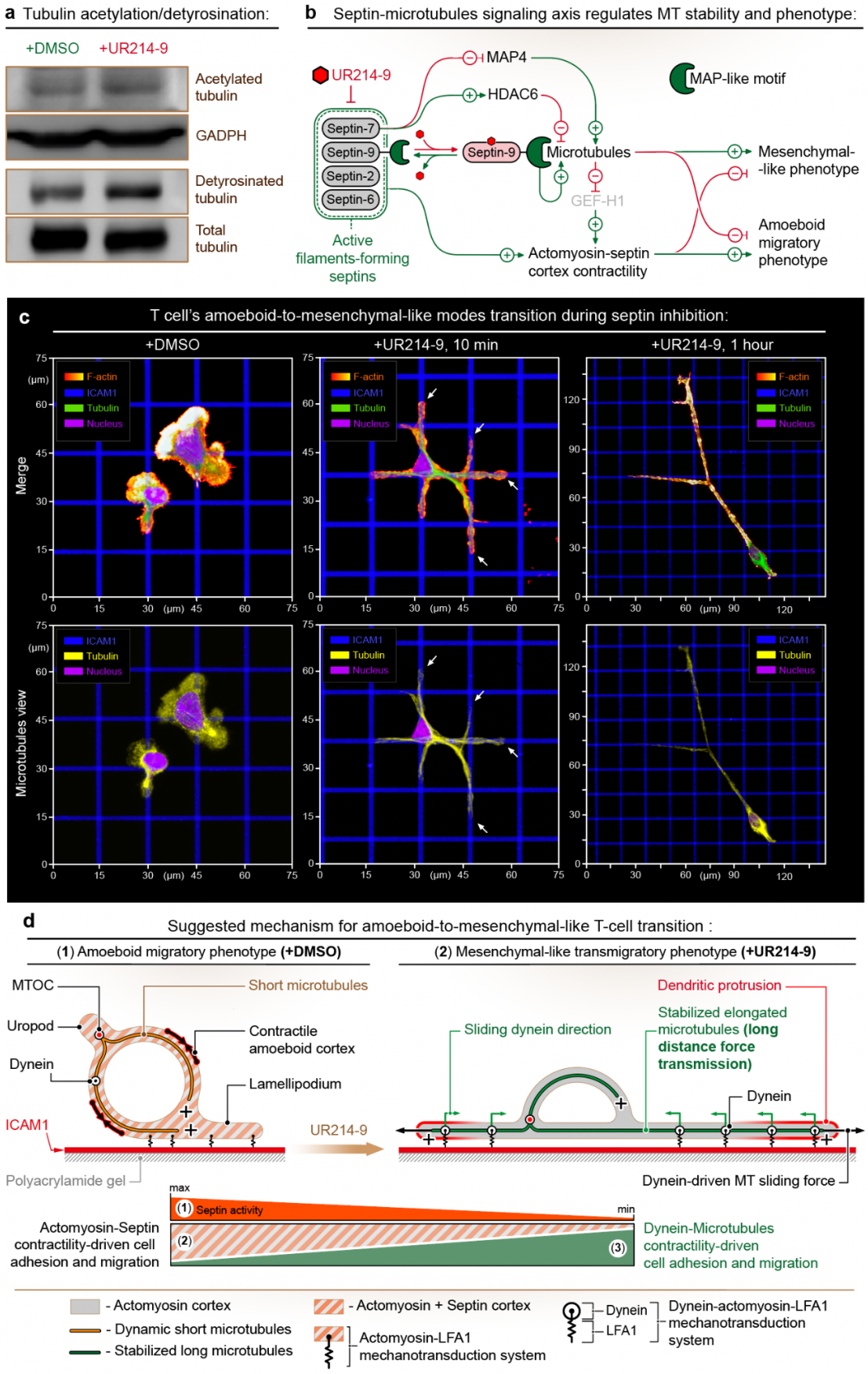
a Tubulin acetylation/detyrosination:
+DMSO
+UR214-9
Acetylated tubulin
GADPH
Detyrosinated tubulin
Total tubulin
b Septin-microtubules signaling axis regulates MT stability and phenotype:
UR214-9
MAP4
HDAC6
MAP-like motif
Septin-7
Septin-9
Septin-2
Septin-6
Septin-9
Microtubules
GEF-H1
Mesenchymal--like phenotype
Amoeboid migratory phenotype
Active filaments-forming septins
Actomyosin-septin cortex contractility
c T cell's amoeboid-to-mesenchymal-like modes transition during septin inhibition:
+DMSO
+UR214-9, 10 min
+UR214-9, 1 hour
Merge
Microtubules view
F-actin
ICAM1
Tubulin
Nucleus
(μm)
d Suggested mechanism for amoeboid-to-mesenchymal-like T-cell transition :
(1) Amoeboid migratory phenotype (+DMSO)
(2) Mesenchymal-like transmigratory phenotype (+UR214-9)
MTOC
Uropod
Dynein
ICAM1
Short microtubules
Contractile amoeboid cortex
Lamellipodium
Polyacrylamide gel
UR214-9
Dendritic protrusion
Sliding dynein direction
Stabilized elongated microtubules (long distance force transmission)
Dynein
Dynein-driven MT sliding force
max
min
(1) Septin activity
(2)
(3)
Actomyosin-Septin contractility-driven cell adhesion and migration
Dynein-Microtubules contractility-driven cell adhesion and migration
- Actomyosin cortex
- Dynamic short microtubules
- Stabilized long microtubules
- Actomyosin + Septin cortex
Actomyosin-LFA1 mechanotransduction system
Dynein
LFA1
Dynein-actomyosin-LFA1 mechanotransduction system

**Figure 7. T cells form multiple dendritic microtubules-rich protrusion and spread along the ICAM1 contact guidance cues during amoeboid-to-mesenchymal-like phenotype transition.**

**(a)** Western blot. Analysis of tubulin acetylation and detyrosination shows a ~20% and ~25-40% increase, respectively, in the level of post-translationally modified tubulin in hCD4+ T cells after the **+UR214-9** treatment.

**(b)** Schematic representation of signaling contours that link septins, microtubules, and actomyosin with the T cell transitioning between amoeboid and mesenchymal-like phenotypes. *Note that during UR214-9-induced suppression of septins' GTPase activity and disassembly of septin filaments, the released SEPT9_i1 (septin-9) acts like a microtubule-associated protein* (*MAP) and stabilizes microtubules.*

**(c)** Confocal microscopy. *Top* - Amoeboid hCD4+ T cells on ICAM1 grid in control conditions **(+DMSO)** have no alignment to the underlying ICAM1 grid **(Movie 7)**. Early after septin inhibition **(+UR214-9**, 10 min**),** hCD4+ T cells acquire dendritic shape and spread along the ICAM1 grid, *i.e.* along the contact guidance cues (*arrows*) **(Movie 8)**. Prolonged septin suppression **(+UR214-9**, 1 hour**)** leads to extreme spreading of T cells along the ICAM1 grid.

*Bottom* - Immunofluorescent visualization of microtubules in the amoeboid **(+DMSO)** and mesenchymal-like **(+UR214-9)** T cells demonstrates the increased density and length of microtubules upon UR214-9 treatment.

**(d)** Schematic representation of the proposed mechanism for T cell transitioning from amoeboid **(+DMSO)** towards mesenchymal-like **(+UR214-9)** phenotype. (1) - amoeboid T cells are largely unresponsive to the guidance cues used in the flat 2D systems because complex shape-changing dynamics of the actomyosin cortex dominates over the 2D adhesion 'footprint'. **(2)** - inhibition of septins activity suppresses dynamics of cortical actomyosin in amoeboid T cells. Simultaneously, released septins, *i.e.* septin-9, translocate onto the microtubules and enhance transmission of dynein-generated forces within microtubule cables which facilitates mesenchymal-like migration.

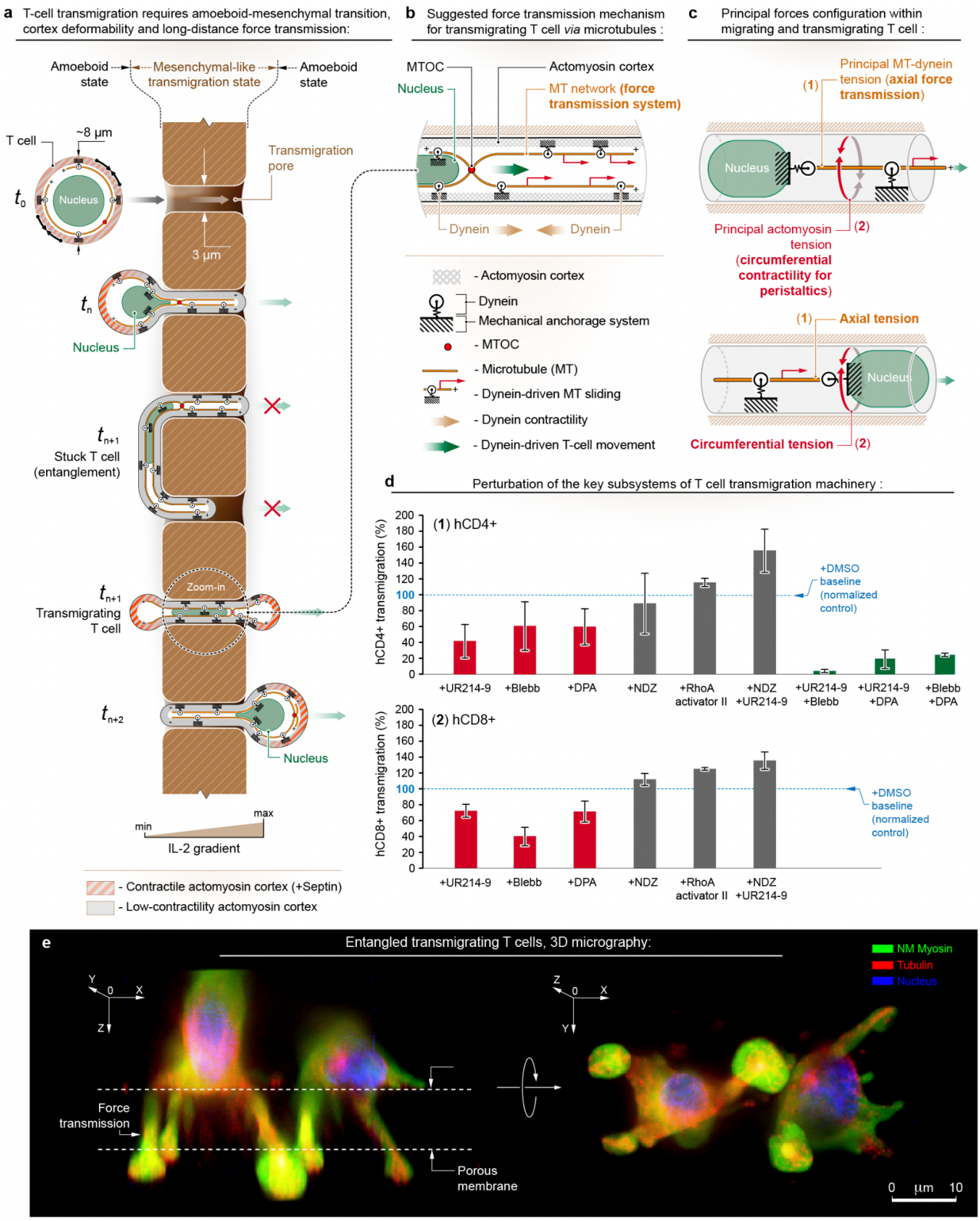
a T-cell transmigration requires amoeboid-mesenchymal transition, cortex deformability and long-distance force transmission:
Amoeboid state
Mesenchymal-like transmigration state
Amoeboid state
T cell
~8 µm
Nucleus
Transmigration pore
3 µm
Nucleus
Stuck T cell (entanglement)
Zoom-in
Transmigrating T cell
Nucleus
min
max
IL-2 gradient
- Contractile actomyosin cortex (+Septin)
- Low-contractility actomyosin cortex
b Suggested force transmission mechanism for transmigrating T cell via microtubules :
MTOC
Actomyosin cortex
Nucleus
MT network (force transmission system)
Dynein
Dynein
- Actomyosin cortex
Dynein
Mechanical anchorage system
- MTOC
- Microtubule (MT)
- Dynein-driven MT sliding
- Dynein contractility
- Dynein-driven T-cell movement
c Principal forces configuration within migrating and transmigrating T cell :
Principal MT-dynein tension (axial force transmission)
(1)
Nucleus
Principal actomyosin tension (circumferential contractility for peristaltics)
(2)
(1) Axial tension
Nucleus
Circumferential tension
(2)
d Perturbation of the key subsystems of T cell transmigration machinery :
(1) hCD4+
hCD4+ transmigration (%)
+DMSO baseline (normalized control)
+UR214-9
+Blebb
+DPA
+NDZ
+RhoA activator II
+NDZ +UR214-9
+UR214-9 +Blebb
+UR214-9 +DPA
+Blebb +DPA
(2) hCD8+
hCD8+ transmigration (%)
+DMSO baseline (normalized control)
+UR214-9
+Blebb
+DPA
+NDZ
+RhoA activator II
+NDZ +UR214-9
e Entangled transmigrating T cells, 3D micrography:
NM Myosin
Tubulin
Nucleus
Force transmission
Porous membrane
0 µm 10

**Figure 8. Transmigration of T cells requires actomyosin- and dynein-generated forces.**

**(a)** To enter and transmigrate through the extremely narrow 3 μm pores, amoeboid T cells must acquire the confinement-induced narrow and elongated cell shape. To prevent overstretching and rupture, while powering the cell body's passage through the pore, T cells require a mechanism for coherent force transmission along the confined cell body. Cortex-bound dynein motors pull the microtubule cables and form a singular mechanical system that facilitates the mechanically and structurally coherent passage of the nucleus between the distant rear and front cell segments.

**(b)** Schematic representation of the transmigrating segment of the T cell. Simplified mechanical system of transmigration-driving force transmission includes: confining pore, actomyosin cortex, microtubules, dynein motors and nucleus.

**(c)** Principal forces within migrating and transmigrating T cell: (**1**) dynein-generated axial forces, transmitted at long distances through microtubules, behaving as cables, and (**2**) actomyosin cortex-generated circumferential tension, structured with multiple cortical rings by septins. Actomyosin circumferential forces predominantly facilitate T cell peristaltic dynamics for the amoeboid propulsion, while dynein-microtubule system-mediated axial forces facilitate a mechanically coherent T cell passage through the confining spaces. The model is equally applicable to the transmigrating T cells that locomote the nucleus as a frontal 'piston', or pull the nucleus at the rear portion of the transmigrating cell.

**(d)** Normalized transmigration efficiency of hCD4+ and hCD8+ T cells during perturbation of the key cytoskeletal subsystems. Inhibition of amoeboid dynamics *via* targeting septins **(+UR214-9)** or actomyosin **(+Blebbistatin)** diminishes transmigration of hCD4+ and hCD8+ T cells. Similarly, suppression of dynein contractility **(+Dynapyrazole A, DPA)** reduces transmigration of hCD4+ and hCD8+ T cells. Disassembly of the microtubules **(+Nocodazole, NDZ)** does not conclusively change transmigration efficiency, as destabilization of microtubules causes opposing effects that mutually compensate for each other, *i.e.* increase of actomyosin contractility *via* MT-GEF-H1 signaling axis and arrest of MT-dependent dynein-generated axial forces. An isolated increase of the actomyosin tension *via* selective RhoA activation **(+RhoA activator II)** increases transmigration of hCD4+ and hCD8+ T cells. Combined suppression of septins and actomyosin **(+UR214-9+Blebbistatin)** or septins and dyneins **(+UR214-9+Dynapyrazole A)** abrogates hCD4+ T cells transmigration. Combined inhibition of dynein- and myosin-generated forces **(+Blebbistatin+Dynapyrazole A)** also suppresses T cell transmigration. *Note that T cells require both actomyosin and dynein-based force production systems for effective transmigration.*

**(e)** Microtubular network, behaving as cables, may hinder T cell transmigration causing the lymphocyte's structural entanglement between several alternative pores (for porous Transwell membranes). As T cell enters multiple pores, the non-stretchable microtubular cables prevent cell from rupturing, while distributing pulling forces between several in-pore T cell protrusions, which captures T cell in an entangled 'tug-of-war' state, stuck between several pores.

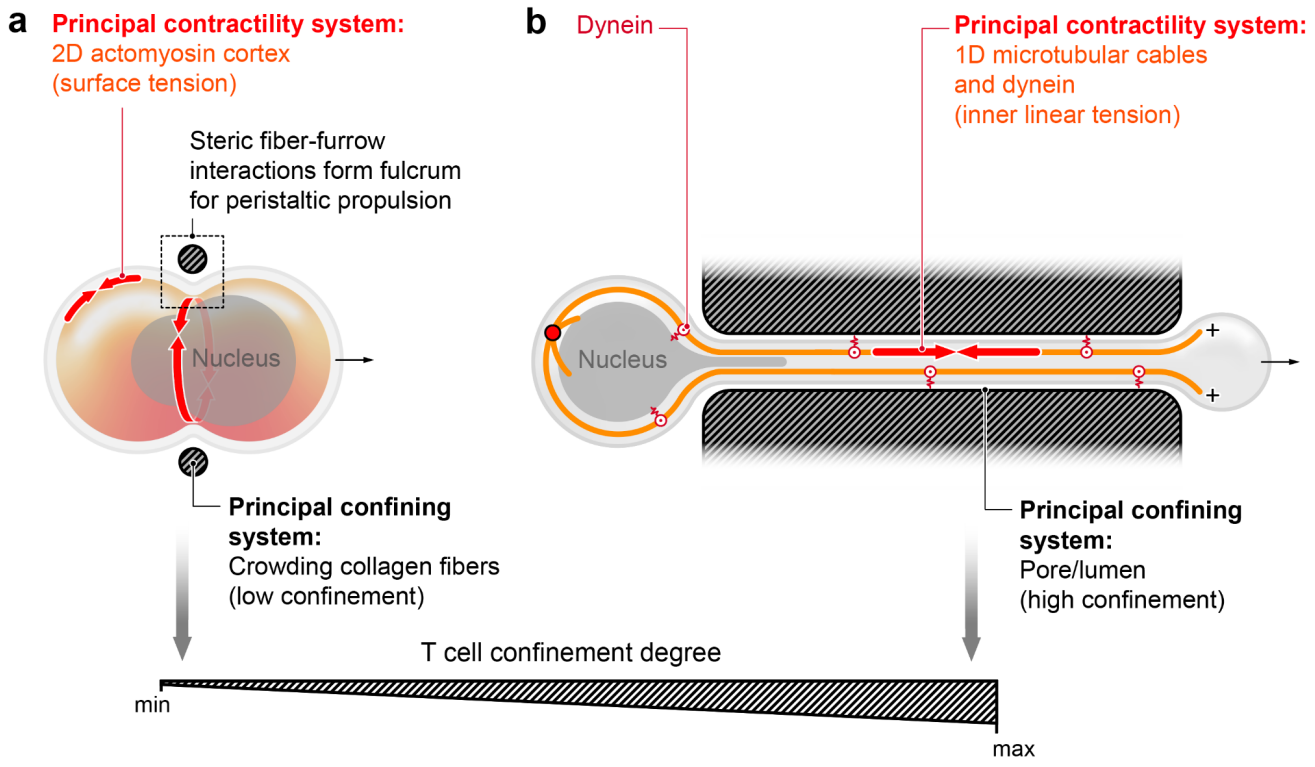


**Figure 9. Model of T cell migration and transmigration in different confinement systems.**

**(a)** Under low confinement, cell surface-indenting steric obstacles (*e.g.* collagen fibers) trigger septin-based compartmentalization of peristaltic actomyosin contractility of the cell cortex. The spatial configuration of adjacent cortical segments provides a transient steric lock onto the confining collagen fibers, rendering the confining obstacles into a mechanical fulcrum for peristaltic lymphocyte's propulsion. The repeated cycles of ECM-guided cortex partitioning mechanically channel T cell migration between the obstacles for adaptive 3D circumnavigation.

**(b)** Under high confinement, microtubule cables provide long-range transmission of mechanical forces across the entire cell body. The long-range transmission of mechanical forces along microtubular cables allows T cells to apply dynein-generated forces for mesenchymal-like transmigration through highly confining spaces (*e.g.* pores).

## SUPPLEMENTARY FIGURES

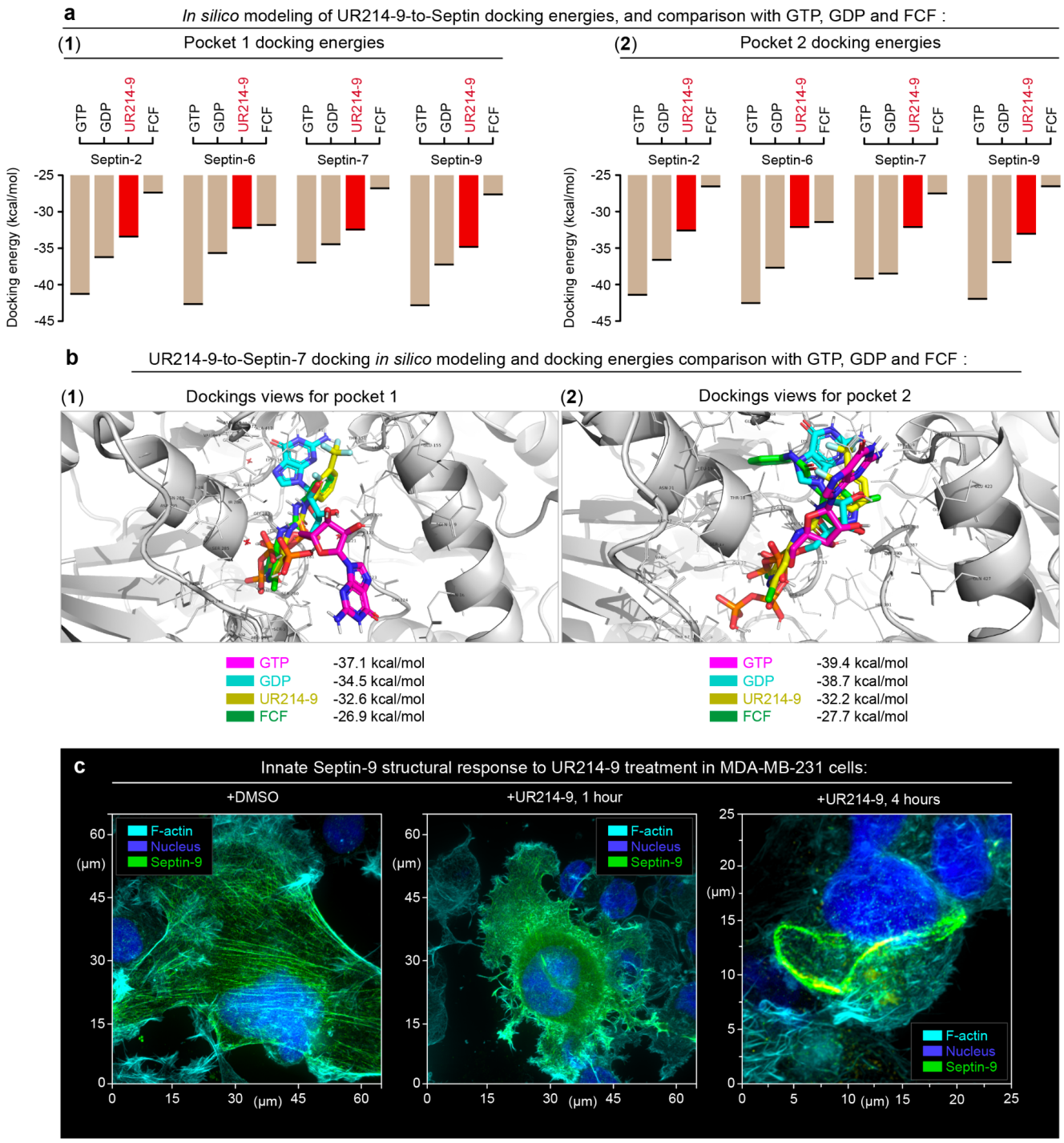


**Supplemental figure SI1. *In silico* molecular docking simulations for the key filaments-related septin isoforms displays a competitive UR214-9-septins interactions energies in comparison to GTP, GDP and FCF**

**(a)** *In silico*-computationally derived energies of GTP, GDP, UR214-9, and FCF docking to pocket-1 and -2 of Septin-7 isoform. Note, that UR214-9-septin docking energy is more optimal, than that of FCF across all key filaments-related septin isoforms.

**(b)** *In silico*-simulated 3D models of molecular docking of GTP, GFP, UR214-9 and FCF to the septin-7's pockets 1 and 2.

**(c)** Septin filaments respond to the UR214-9 treatment in MDA-MB-231 cells, as shown by Septin-9 staining. MDA-MB-231 cells, spread on a glass surface (fibronectin) form stress-fibers (phalloidin) and septin filaments (Septin-9 immunofluorescence) as a single cytoskeletal network **(+DMSO)**. Cells treatment with a mammalian septins inhibitor results in the dissociation of the actin and septin filaments and retraction of cells **(+UR214-9,** 1 hour**)**, progressing into a complete loss of cell spreading and microtubule reorganization into a giant ring **(+UR214-9,** 4 hours**)**. Instant structured illumination microscopy.

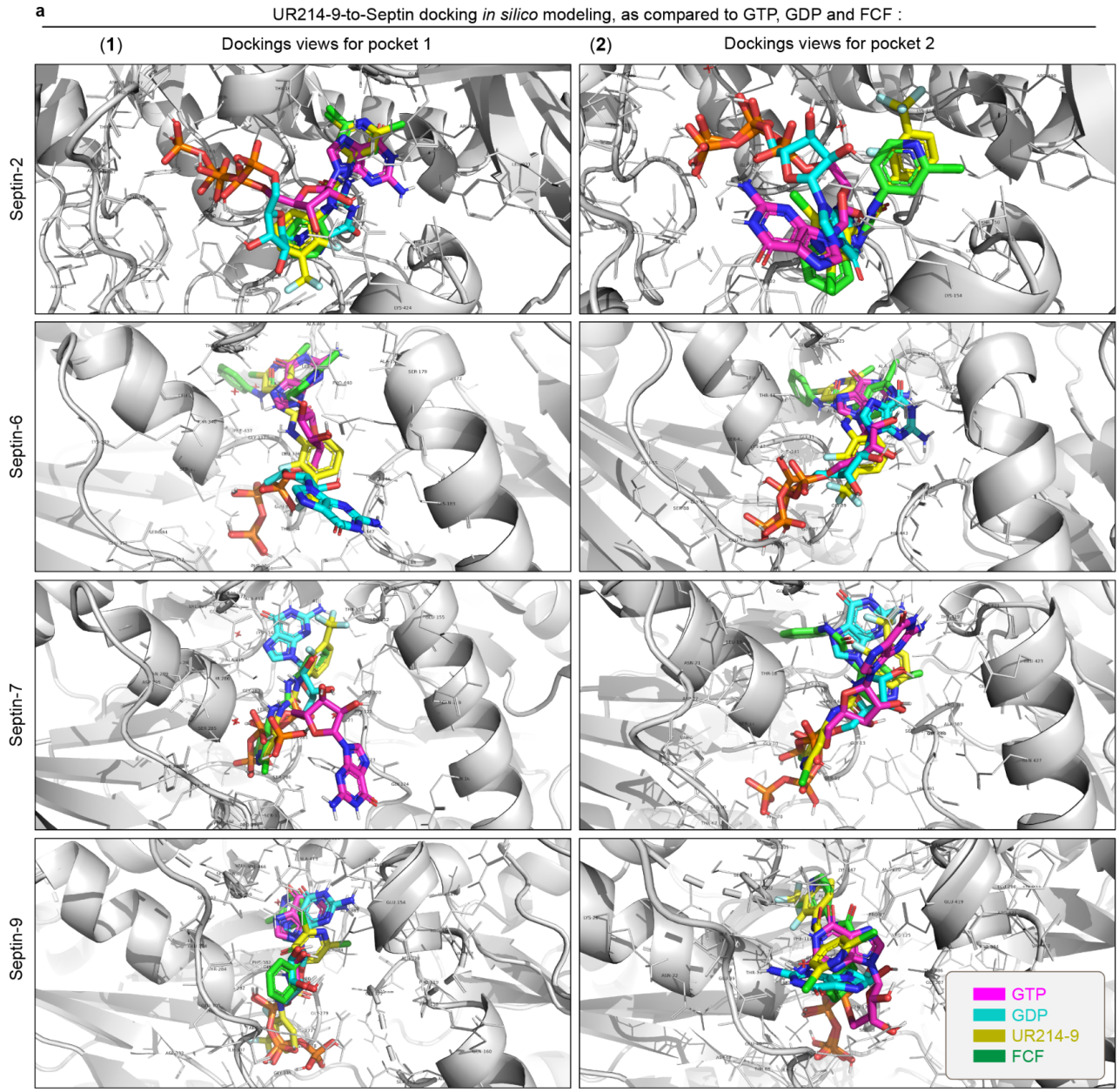


**b** UR214-9-to-Septin docking energy *in silico* modeling, as compared to GTP, GDP and FCF :

(**1**) Table 1

| Ligand | Energy of interactions, pocket 1 (kcal/mol): Septin-2 | Septin-6 | Septin-7 | Septin-9 |
|---|---|---|---|---|
| GTP | -41.4013 | -42.7594 | -37.1021 | -42.9431 |
| GDP | -36.3165 | -35.7889 | -34.5495 | -37.3714 |
| UR214-9 | -33.4929 | -32.3030 | -32.5959 | -34.9654 |
| FCF | -27.4643 | -31.9061 | -26.8665 | -27.6648 |

(**2**) Table 2

| Ligand | Energy of interactions, pocket 2 (kcal/mol): Septin-2 | Septin-6 | Septin-7 | Septin-9 |
|---|---|---|---|---|
| GTP | -41.5791 | -42.7328 | -39.3803 | -42.1438 |
| GDP | -36.7661 | -37.8403 | -38.6942 | -37.0604 |
| UR214-9 | -32.6248 | -32.2466 | -32.2272 | -33.0542 |
| FCF | -26.6455 | -31.5510 | -27.6554 | -26.6600 |

**Supplemental figure SI2. UR214-9-septin *in silico* docking simulations display competitive energies of interactions as compared to FCF, GTP and GDP.**

**(a)** *In silico* computational model for UR214-9 docking to septin-2, -6, -7 and -9's GTPase site at the respective pockets 1 and 2 in septin molecules, as compared to FCF inhibitor and GTP.

**(b)** *In silico*-calculated docking energies for GTP, GDP, UR214-9 and FCF.

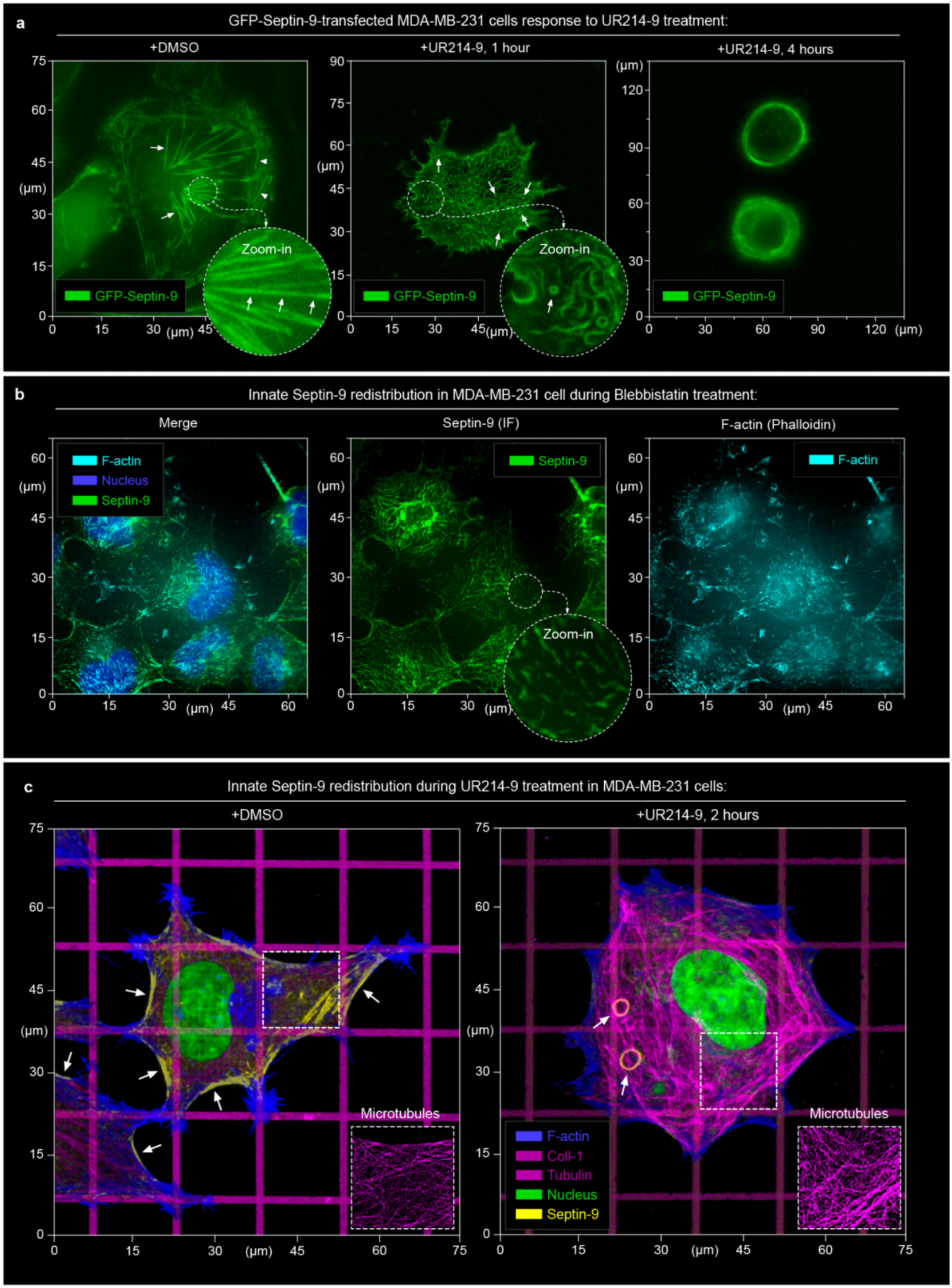
a
GFP-Septin-9-transfected MDA-MB-231 cells response to UR214-9 treatment:
+DMSO
+UR214-9, 1 hour
+UR214-9, 4 hours
Zoom-in
GFP-Septin-9
(µm)
b
Innate Septin-9 redistribution in MDA-MB-231 cell during Blebbistatin treatment:
Merge
Septin-9 (IF)
F-actin (Phalloidin)
F-actin
Nucleus
Septin-9
Zoom-in
c
Innate Septin-9 redistribution during UR214-9 treatment in MDA-MB-231 cells:
+DMSO
+UR214-9, 2 hours
Microtubules
F-actin
Coll-1
Tubulin
Nucleus
Septin-9

**Supplemental figure SI3. Septins (Septin-9 staining) colocalize with tensile actomyosin structures (stress-fibers) that disintegrate both in the presence of septin inhibitor (+UR214-9) and during suppression of actomyosin contractility (+Blebbistatin).**

**(a)** *Left* - GFP-Septin-9 overexpressing and fully spread MDA-MB-231 cells show Septin-9 filaments in radial dorsoventral stress-fibers and within the transverse arcs **(+DMSO)**. C*enter* - septin inhibitor induces septin filaments disintegration **(+UR214-9, 1 hour)**, and (*right*) complete cell detachment upon collapse of cytoskeletal network **(+UR214-9, 4 hours)**.

**(b)** Septins (Septin-9) and F-actin (phalloidin) filaments disintegrate upon inhibition of actomyosin contractility **(+Blebbistatin)**.

**(c)** In control conditions **(+DMSO),** biaxial spreading of cells along the orthogonal collagen-1 grid results with the polygonal cell architecture. Free cell edges feature anisotropy that results with linear alignment of contractile actomyosin filaments, and as a result, these edges feature the highest tension and have the most developed stress-fibers. The tensile cell regions accumulate Septin-9 (white arrows), while UR214-9 induces Septin-9 translocation from actomyosin onto the microtubules. Insets in dashed boxes show the enhanced (deconvoluted) details of the microtubular architectures.

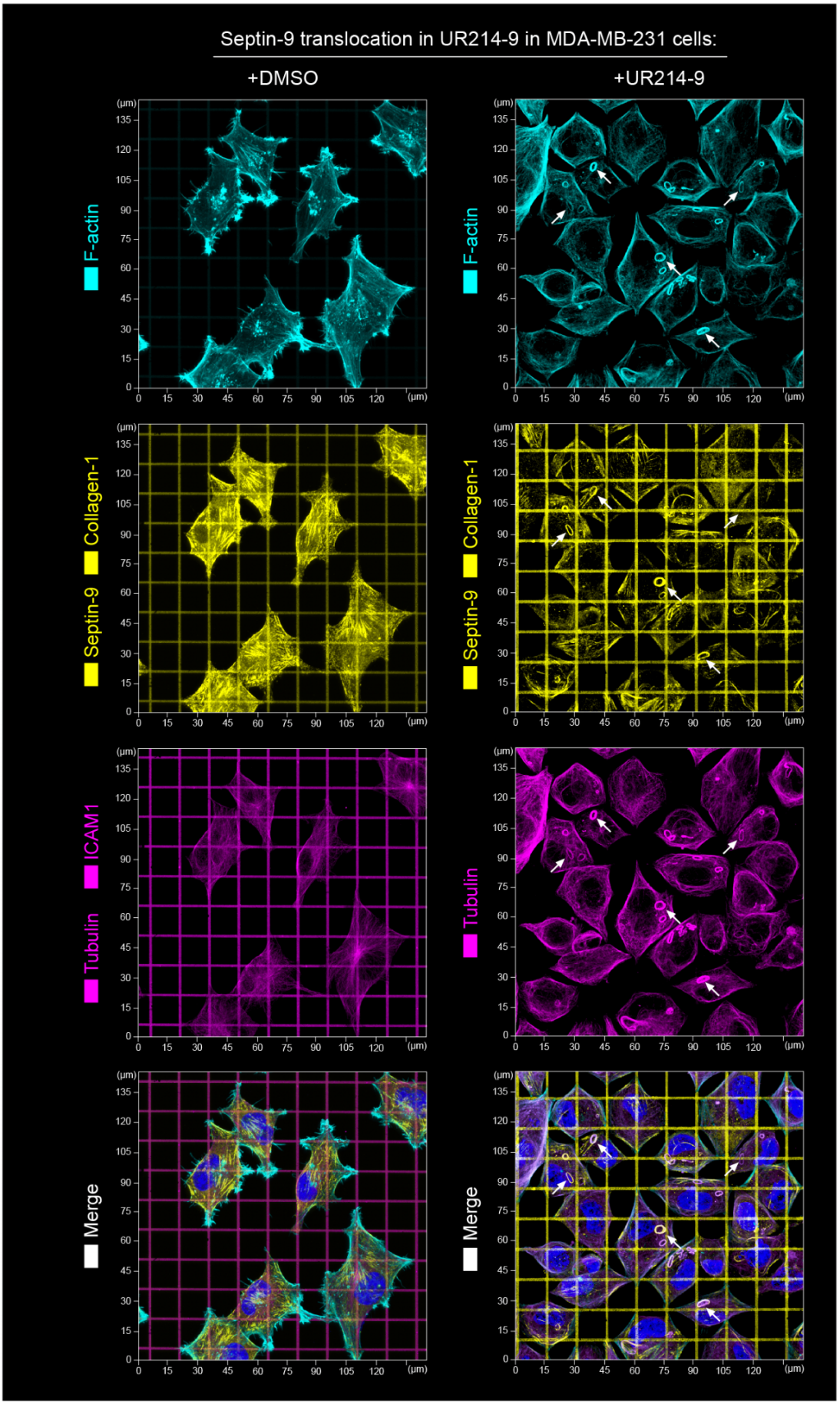
Septin-9 translocation in UR214-9 in MDA-MB-231 cells:
+DMSO
+UR214-9
F-actin
Septin-9
Collagen-1
Tubulin
ICAM1
Merge
(µm)
0
15
30
45
60
75
90
105
120
135

**Supplemental figure SI4. Septins inhibition (+UR214-9) in MDA-MB-231 cells on collagen (type I) grids induces translocation of septin-9 from the stress-fibers onto microtubules.**

*Top* - Septin-9 in vehicle-treated cells **(+DMSO)** colocalizes with linear F-actin structures (stress-fibers).

*Bottom* - Septin-9 translocates onto the microtubules upon suppression of septins GTPase activity **(+UR214-9,** t≥1 hour**)**. Note that GTPase-inactive septin-9 acts as a microtubule-associated protein (MAP), stabilizing microtubules and inducing MT curling into the rings (*arrows*) (Zhovmer et al., 2021).

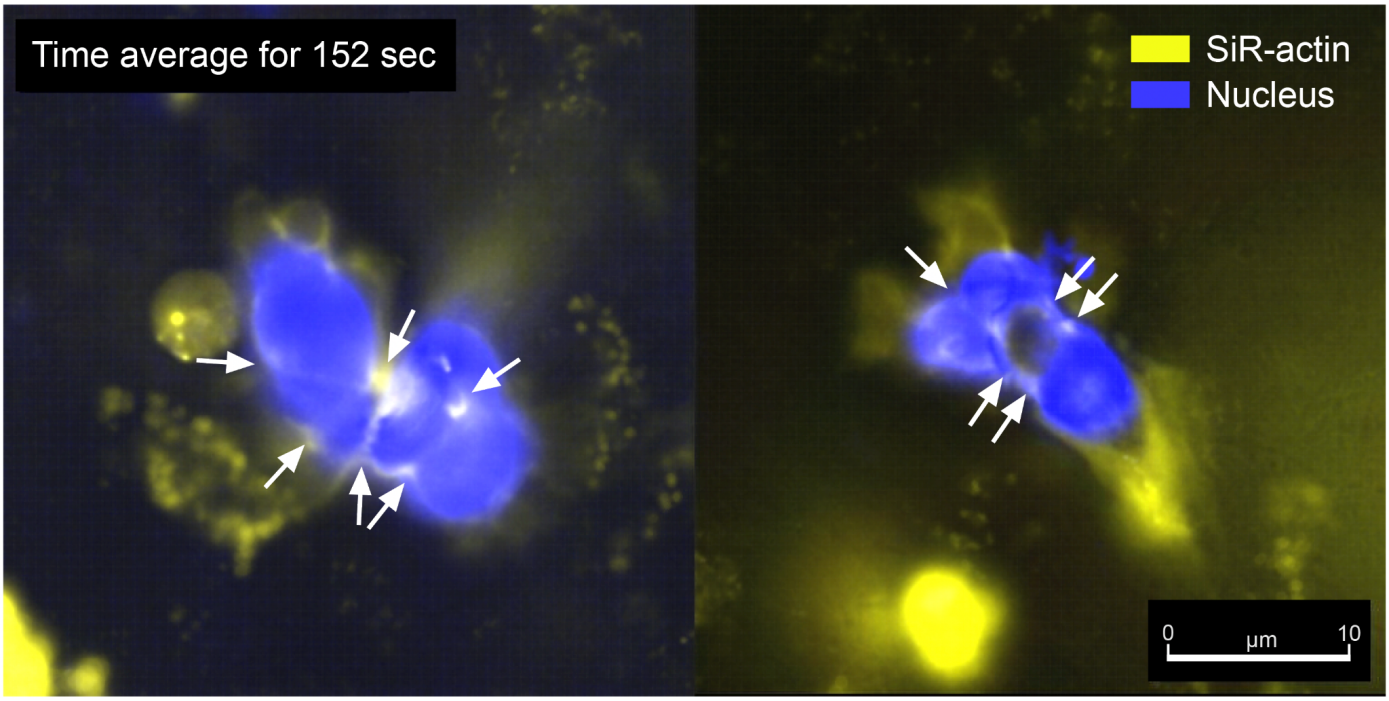


**Supplemental figure SI5. Time average projections of the migrating hCD4+ T cells within the collagen matrix reveal stationary cortical rings and the peristaltic translocation of the nucleus.** F-actin-dense rings (*arrows*, side views, seen as bands, SiR-actin live staining) form a cortical tube that channels the nucleus (blue) *via* peristaltically amoeboid cortex passage. *The shown time average projections correspond to the video sequences in Movie 3.*

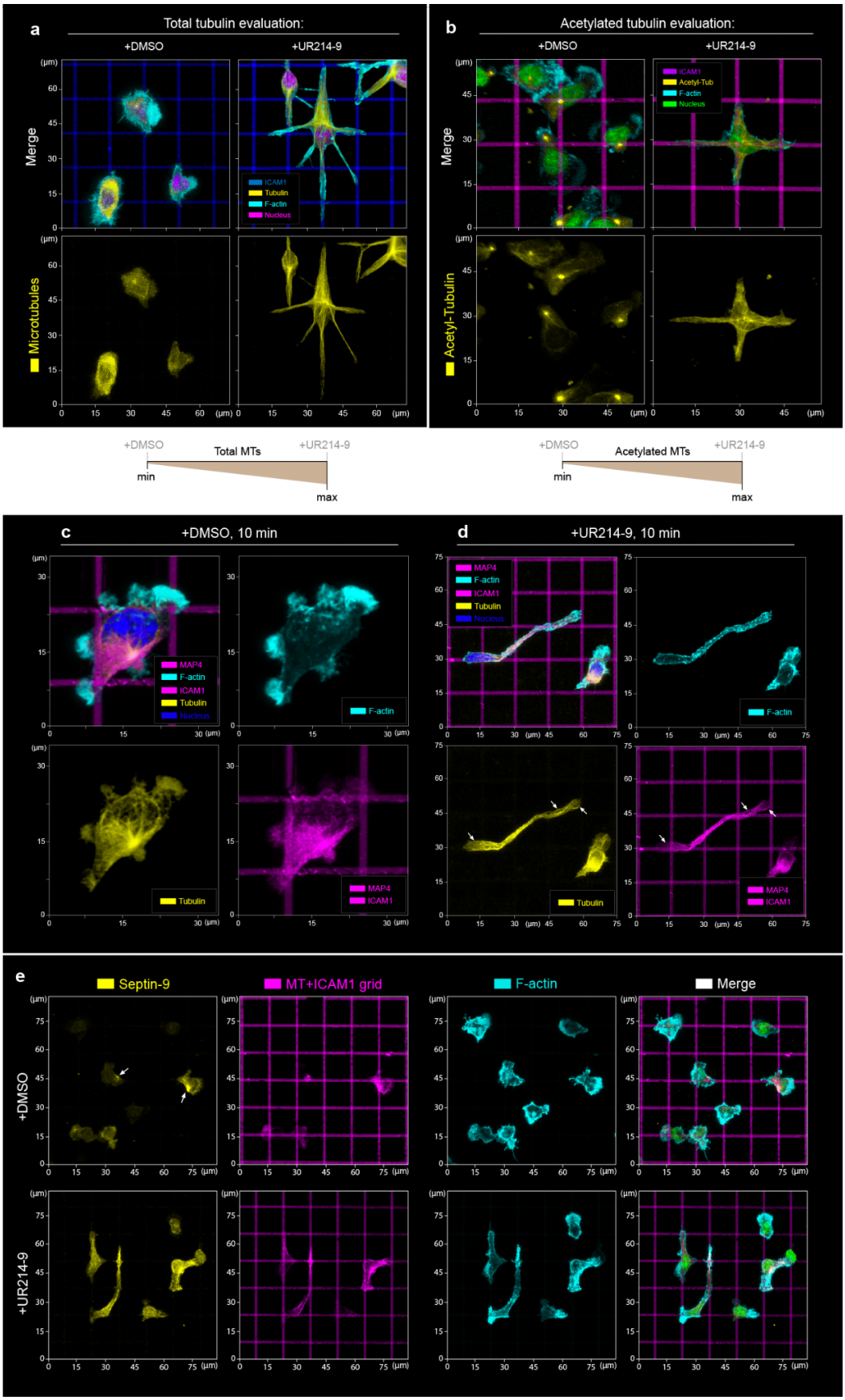
a
Total tubulin evaluation:
+DMSO
+UR214-9
Merge
Microtubules
ICAM1
Tubulin
F-actin
Nucleus
b
Acetylated tubulin evaluation:
+DMSO
+UR214-9
Merge
Acetyl-Tubulin
ICAM1
Acetyl-Tub
F-actin
Nucleus
+DMSO
Total MTs
+UR214-9
min
max
+DMSO
Acetylated MTs
+UR214-9
min
max
c
+DMSO, 10 min
MAP4
F-actin
ICAM1
Tubulin
Nucleus
d
+UR214-9, 10 min
MAP4
F-actin
ICAM1
Tubulin
Nucleus
e
Septin-9
MT+ICAM1 grid
F-actin
Merge
+DMSO
+UR214-9

**Supplemental figure SI6. UR214-9-induced septin inactivation initiates amoeboid-to-mesenchymal-like T cell transition that is accompanied by increased post-translational modifications of microtubules, MAP4-MT adsorption, MTs elongation and densification.**

**(a)** hCD4+ T cells during control treatment **(+DMSO)** maintain diffuse, low density MT architecture and amoeboid phenotype, featuring neither spreading nor alignment along the T cell adhesion cues (ICAM1 anisotropic parallel lines). Septin inhibition **(+UR214-9)** induces dendritic spreading of T cells along the ICAM1 grid and build up of microtubules.

**(b)** Immunofluorescence analysis shows an increased MT acetylation that accompanies MT apparatus build-up during septin inhibition **(+UR214-9)** compared to the control T cells **(+DMSO)**.

**(c-d)** MAP4-MT adsorption analysis across control **(c, +DMSO)** and septin-inhibited **(d, +UR214-9)** T cells indicates that UR214-9 induces MAP4 accumulation (*arrows*) on the structurally densified and elongated microtubules compared to the cytosolic diffuse MAP4 distribution in the control T cells.

**(e)** Septin-9 microtubular translocation, induced by suppression of septins' GTPase activity **(+UR214-9)**.

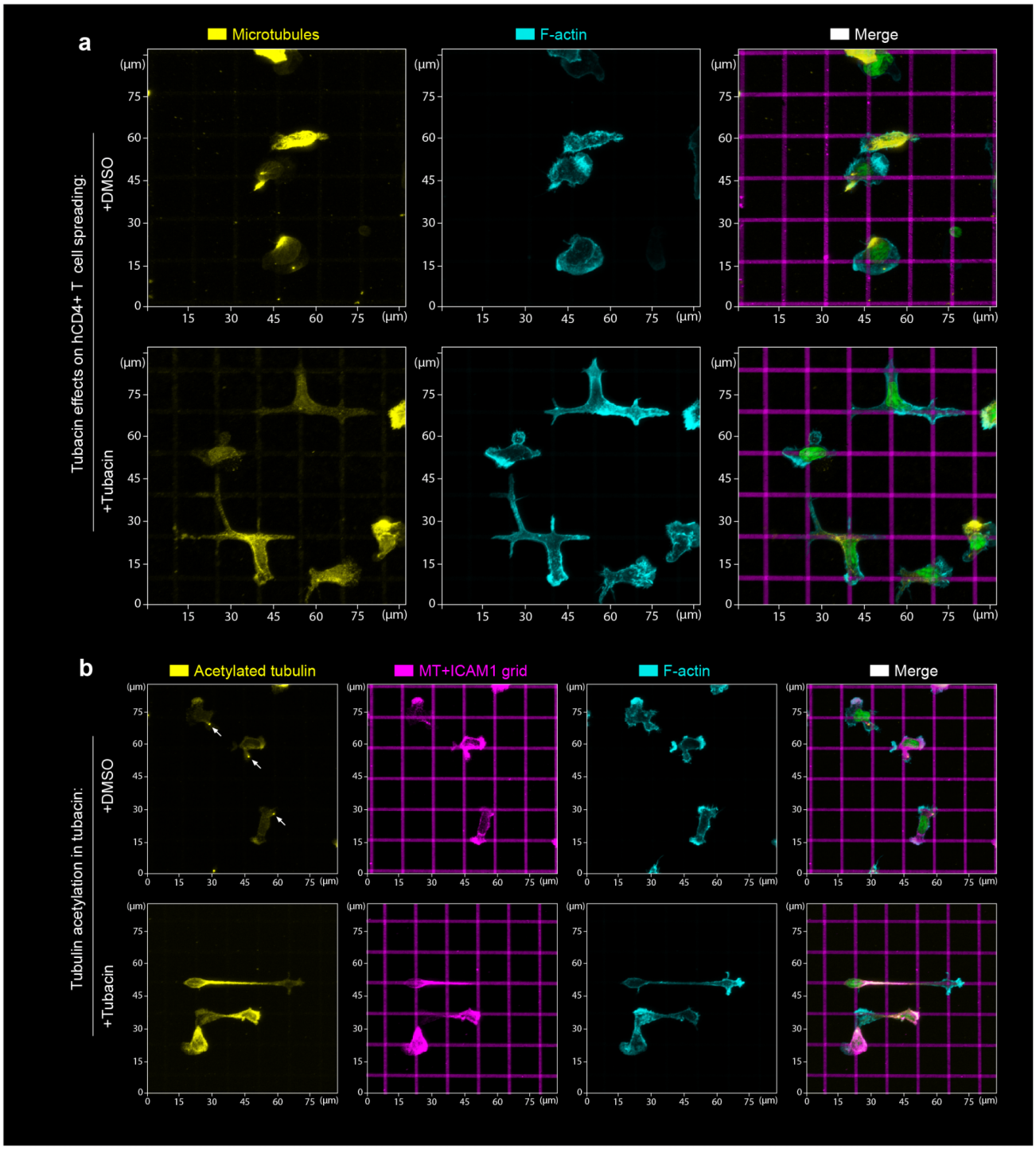


**Supplemental figure SI7. Stabilization of microtubules *via* Tubacin-induced hyperacetylation phenocopies the UR214-9-induced hCD4+ T cell transitioning towards mesenchymal-like dendritic spreading.**

**(a)** hCD4+ T cells during HDAC6 suppression **(+Tubacin,** t≥1 hour**)** display a partial amoeboid-to-mesenchymal-like transitioning, *i.e.* T cell dendritic spreading along the ICAM1 grids.

**(b)** Analysis of MT acetylation in hCD4+ T cells, induced by HDAC6 suppression **(+Tubacin,** t≥1 hour**),** shows an increased acetylation of microtubules compared to the control T cell group **(+DMSO)**. *Identified centrosomes indicated with arrows.*

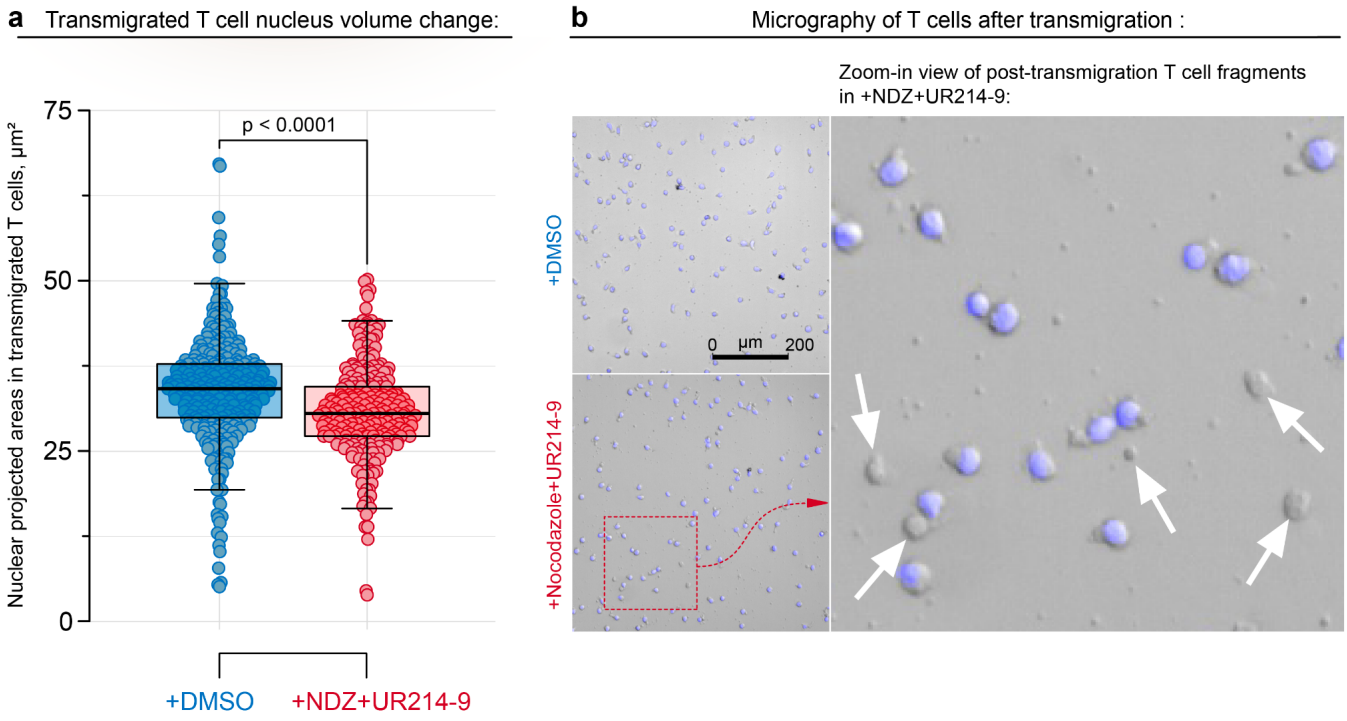


**Supplemental figure SI8. Loss of structural stability in hCD8+ T cells during transmigration enhanced by microtubules destabilization and septins inhibition (+Nocodazole+UR214-9).**

**(a)** Evaluation of the population-wide hCD8+ T cells nuclei sizes (2D projected nucleus areas) after transmigration in control **(+DMSO)** and treated **(+Nocodazole+UR214-9)** T cell groups displays an ~11% loss of the nuclear sizes in the treated cells.

**(b)** Micrography views (brightfield and Hoechst) of post-transmigration T cells. +Nocodazole+UR214-9-treated T cells form numerous enucleated cell fragments in the post-transmigration fraction (*arrows*).

## REFERENCES


Adams, G., Jr, Preciado-Lopez, M., Fischer, R.S., Baird, M.A., Logue, J., and Waterman, C.M. (2018). Functional Behavior of Melanoma Cells Under High Confinement, High Contractility and Low Adhesion Mediating Leader Bleb Based Motility. In MOLECULAR BIOLOGY OF THE CELL, (AMER SOC CELL BIOLOGY 8120 WOODMONT AVE, STE 750, BETHESDA, MD 20814-2755 USA),.

Adams, G., Jr, López, M.P., Cartagena-Rivera, A.X., and Waterman, C.M. (2021). Survey of cancer cell anatomy in nonadhesive confinement reveals a role for filamin-A and fascin-1 in leader bleb-based migration. Mol. Biol. Cell *32*, 1772–1791. .

Ageta-Ishihara, N., Miyata, T., Ohshima, C., Watanabe, M., Sato, Y., Hamamura, Y., Higashiyama, T., Mazitschek, R., Bito, H., and Kinoshita, M. (2013). Septins promote dendrite and axon development by negatively regulating microtubule stability via HDAC6-mediated deacetylation. Nat. Commun. *4*, 1–11. .

Alper, J.D., Decker, F., Agana, B., and Howard, J. (2014). The motility of axonemal dynein is regulated by the tubulin code. Biophys. J. *107*, 2872–2880. .

Aoun, L., Farutin, A., Garcia-Seyda, N., Nègre, P., Rizvi, M.S., Tlili, S., Song, S., Luo, X., Biarnes-Pelicot, M., Galland, R., et al. (2020). Amoeboid Swimming Is Propelled by Molecular Paddling in Lymphocytes. Biophys. J. *119*, 1157–1177. .

Badding, M.A., and Dean, D.A. (2012). Highly acetylated tubulin permits enhanced interactions with and trafficking of plasmids along microtubules. Gene Ther. *20*, 616–624. .

Bai, X., Karasmanis, E.P., and Spiliotis, E.T. (2016). Septin 9 interacts with kinesin KIF17 and interferes with the mechanism of NMDA receptor cargo binding and transport. Mol. Biol. Cell *27*, 897–906. .

Balzer, E.M., Tong, Z., Paul, C.D., Hung, W.-C., Stroka, K.M., Boggs, A.E., Martin, S.S., and Konstantopoulos, K. (2012). Physical confinement alters tumor cell adhesion and migration phenotypes. The FASEB Journal *26*, 4045–4056. .

Beber, A., Taveneau, C., Nania, M., Tsai, F.-C., Di Cicco, A., Bassereau, P., Lévy, D., Cabral, J.T., Isambert, H., Mangenot, S., et al. (2019). Membrane reshaping by micrometric curvature sensitive septin filaments. Nat. Commun. *10*, 420. .

Bridges, A.A., and Gladfelter, A.S. (2015). Septin Form and Function at the Cell Cortex. J. Biol. Chem. *290*, 17173–17180. .

Bustos-Morán, E., Blas-Rus, N., Martin-Cófreces, N.B., and Sánchez-Madrid, F. (2017). Microtubule-associated protein-4 controls nanovesicle dynamics and T cell activation. J. Cell Sci. *130*, 1217–1223. .

Carey, S.P., Rahman, A., Kraning-Rush, C.M., Romero, B., Somasegar, S., Torre, O.M., Williams, R.M., and Reinhart-King, C.A. (2015). Comparative mechanisms of cancer cell migration through 3D matrix and physiological microtracks. Am. J. Physiol. Cell Physiol. *308*, C436–C447. .

Cartagena-Rivera, A.X., Logue, J.S., Waterman, C.M., and Chadwick, R.S. (2016). Actomyosin Cortical Mechanical Properties in Nonadherent Cells Determined by Atomic Force Microscopy. Biophys. J. *110*, 2528–2539. .

Charras, G., and Paluch, E. (2008). Blebs lead the way: how to migrate without lamellipodia. Nat. Rev. Mol. Cell Biol. *9*, 730–736. .

Charras, G.T., Yarrow, J.C., Horton, M.A., Mahadevan, L., and Mitchison, T.J. (2005). Non-equilibration of hydrostatic pressure in blebbing cells. Nature *435*, 365–369. .

Charras, G.T., Hu, C.-K., Coughlin, M., and Mitchison, T.J. (2006). Reassembly of contractile actin cortex in cell blebs. J. Cell Biol. *175*, 477–490. .

Cheffings, T.H., Burroughs, N.J., and Balasubramanian, M.K. (2016). Actomyosin Ring Formation and Tension Generation in Eukaryotic Cytokinesis. Curr. Biol. *26*, R719–R737. .

Chen, W., Lou, J., and Zhu, C. (2010). Forcing Switch from Short- to Intermediate- and Long-lived States of the αA Domain Generates LFA-1/ICAM-1 Catch Bonds *. J. Biol. Chem. *285*, 35967–35978. .

Ding, F., Yin, S., and Dokholyan, N.V. (2010). Rapid flexible docking using a stochastic rotamer library of ligands. J. Chem. Inf. Model. *50*, 1623–1632. .

Dolat, L., Hunyara, J.L., Bowen, J.R., Karasmanis, E.P., Elgawly, M., Galkin, V.E., and Spiliotis, E.T. (2014). Septins promote stress fiber--mediated maturation of focal adhesions and renal epithelial motility. J. Cell Biol. *207*, 225–235. .

Estey, M.P., Di Ciano-Oliveira, C., Froese, C.D., Bejide, M.T., and Trimble, W.S. (2010). Distinct roles of septins in cytokinesis: SEPT9 mediates midbody abscission. J. Cell Biol. *191*, 741–749. .

Filippi, M.-D. (2016). Mechanism of Diapedesis: Importance of the Transcellular Route. Adv. Immunol. *129*, 25–53. .

Fischer, R.S., Myers, K.A., Gardel, M.L., and Waterman, C.M. (2012). Stiffness-controlled three-dimensional extracellular matrices for high-resolution imaging of cell behavior. Nat. Protoc. *7*, 2056–2066. .

Fokin, A.I., David, V., Oguievetskaia, K., Derivery, E., Stone, C.E., Cao, L., Rocques, N., Molinie, N., Henriot, V., Aumont-Nicaise, M., et al. (2021). The Arp1/11 minifilament of dynactin primes the endosomal Arp2/3 complex. Sci Adv *7*. https://doi.org/10.1126/sciadv.abd5956.

Founounou, N., Loyer, N., and Le Borgne, R. (2013). Septins regulate the contractility of the actomyosin ring to enable adherens junction remodeling during cytokinesis of epithelial cells. Dev. Cell *24*, 242–255. .

Fritzsche, M., Lewalle, A., Duke, T., Kruse, K., and Charras, G. (2013). Analysis of turnover dynamics of the submembranous actin cortex. Mol. Biol. Cell *24*, 757–767. .

Füchtbauer, A., Lassen, L.B., Jensen, A.B., Howard, J., Quiroga, A. de S., Warming, S., Sørensen, A.B., Pedersen, F.S., and Füchtbauer, E.-M. (2011). Septin9 is involved in septin filament formation and cellular stability. Biol. Chem. *392*, 769–777. .

Gilden, J.K., Peck, S., Chen, Y.-C.M., and Krummel, M.F. (2012). The septin cytoskeleton facilitates membrane retraction during motility and blebbing. J. Cell Biol. *196*, 103–114. .

van der Gucht, J., Paluch, E., Plastino, J., and Sykes, C. (2005). Stress release drives symmetry breaking for actin-based movement. Proceedings of the National Academy of Sciences *102*, 7847–7852. .

Hammond, T.R., Marsh, S.E., and Stevens, B. (2019). Immune Signaling in Neurodegeneration. Immunity *50*, 955–974. .

Hladyshau, S., Kho, M., Nie, S., and Tsygankov, D. (2021). Spatiotemporal development of coexisting wave domains of Rho activity in the cell cortex. Sci. Rep. *11*, 19512. .

Hu, Q., Nelson, W.J., and Spiliotis, E.T. (2008). Forchlorfenuron alters mammalian septin assembly, organization, and dynamics. J. Biol. Chem. *283*, 29563–29571. .

Hung, W.-C., Chen, S.-H., Paul, C.D., Stroka, K.M., Lo, Y.-C., Yang, J.T., and Konstantopoulos, K. (2013). Distinct signaling mechanisms regulate migration in unconfined versus confined spaces. J. Cell Biol. *202*,

807–824. .

Hynes, R.O. (2002). Integrins: bidirectional, allosteric signaling machines. Cell *110*, 673–687. .

Islam, S.A., and Luster, A.D. (2012). T cell homing to epithelial barriers in allergic disease. Nat. Med. *18*, 705–715. .

Jacobelli, J., Friedman, R.S., Conti, M.A., Lennon-Dumenil, A.-M., Piel, M., Sorensen, C.M., Adelstein, R.S., and Krummel, M.F. (2010). Confinement-optimized three-dimensional T cell amoeboid motility is modulated via myosin IIA-regulated adhesions. Nat. Immunol. *11*, 953–961. .

Jimenez, A.J., Schaeffer, A., De Pascalis, C., Letort, G., Vianay, B., Bornens, M., Piel, M., Blanchoin, L., and Théry, M. (2021). Acto-myosin network geometry defines centrosome position. Curr. Biol. https://doi.org/10.1016/j.cub.2021.01.002.

Kim, D., You, E., and Rhee, S. (2012). Dynein regulates cell migration depending on substrate rigidity. Int. J. Mol. Med. *29*, 440–446. .

Kim, K.K., Singh, R.K., Khazan, N., Kodza, A., Singh, N.A., Jones, A., Sivagnanalingam, U., Towner, M., Itamochi, H., Turner, R., et al. (2020). Development of Potent Forchlorfenuron Analogs and Their Cytotoxic Effect in Cancer Cell Lines. Sci. Rep. *10*, 3241. .

Kim, M.S., Froese, C.D., Estey, M.P., and Trimble, W.S. (2011). SEPT9 occupies the terminal positions in septin octamers and mediates polymerization-dependent functions in abscission. J. Cell Biol. *195*, 815–826. .

Kinoshita, M., Field, C.M., Coughlin, M.L., Straight, A.F., and Mitchison, T.J. (2002). Self- and actin-templated assembly of Mammalian septins. Dev. Cell *3*, 791–802. .

Kopf, A., and Kiermaier, E. (2021). Dynamic Microtubule Arrays in Leukocytes and Their Role in Cell Migration and Immune Synapse Formation. Front Cell Dev Biol *9*, 635511. .

Kopf, A., Renkawitz, J., Hauschild, R., Girkontaite, I., Tedford, K., Merrin, J., Thorn-Seshold, O., Trauner, D., Häcker, H., Fischer, K.-D., et al. (2020). Microtubules control cellular shape and coherence in amoeboid migrating cells. J. Cell Biol. *219*. https://doi.org/10.1083/jcb.201907154.

Kremer, B.E., Haystead, T., and Macara, I.G. (2005). Mammalian Septins Regulate Microtubule Stability through Interaction with the Microtubule-binding Protein MAP4. MBoC *16*, 4648–4659. .

Kremer, B.E., Adang, L.A., and Macara, I.G. (2007). Septins regulate actin organization and cell-cycle arrest through nuclear accumulation of NCK mediated by SOCS7. Cell *130*, 837–850. .

Krendel, M., Zenke, F.T., and Bokoch, G.M. (2002). Nucleotide exchange factor GEF-H1 mediates cross-talk between microtubules and the actin cytoskeleton. Nat. Cell Biol. *4*, 294–301. .

Krummel, M.F., Friedman, R.S., and Jacobelli, J. (2014). Modes and mechanisms of T cell motility: roles for confinement and Myosin-IIA. Curr. Opin. Cell Biol. *30*, 9–16. .

Krummel, M.F., Bartumeus, F., and Gérard, A. (2016). T cell migration, search strategies and mechanisms. Nat. Rev. Immunol. *16*, 193–201. .

Kuzmić, M., Linares, G.C., Fialová, J.L., Iv, F., Salaün, D., Llewellyn, A., Gomes, M., Belhabib, M., Liu, Y., Asano, K., et al. (2021). Septin-microtubule association via a motif unique to the isoform 1 of septin 9 tunes stress fibers. J. Cell Sci. https://doi.org/10.1242/jcs.258850.

Lanitis, E., Dangaj, D., Irving, M., and Coukos, G. (2017). Mechanisms regulating T-cell infiltration and activity in solid tumors. Ann. Oncol. *28*, xii18–xii32. .

Lehtimäki, J.I., Rajakylä, E.K., Tojkander, S., and Lappalainen, P. (2021). Generation of stress fibers through myosin-driven reorganization of the actin cortex. Elife *10*. https://doi.org/10.7554/eLife.60710.

Ley, K., Laudanna, C., Cybulsky, M.I., and Nourshargh, S. (2007). Getting to the site of inflammation: the leukocyte adhesion cascade updated. Nat. Rev. Immunol. *7*, 678–689. .

Liu, Y.-J., Le Berre, M., Lautenschlaeger, F., Maiuri, P., Callan-Jones, A., Heuzé, M., Takaki, T., Voituriez, R., and Piel, M. (2015). Confinement and low adhesion induce fast amoeboid migration of slow mesenchymal cells. Cell *160*, 659–672. .

Logue, J.S., Cartagena-Rivera, A.X., Baird, M.A., Davidson, M.W., Chadwick, R.S., and Waterman, C.M. (2015). Erk regulation of actin capping and bundling by Eps8 promotes cortex tension and leader bleb-based migration. Elife *4*, e08314. .

McEvoy, E., Deshpande, V.S., and McGarry, P. (2017). Free energy analysis of cell spreading. J. Mech. Behav. Biomed. Mater. *74*, 283–295. .

McKenney, R.J., Huynh, W., Vale, R.D., and Sirajuddin, M. (2016). Tyrosination of α-tubulin controls the initiation of processive dynein-dynactin motility. EMBO J. *35*, 1175–1185. .

Mostowy, S., and Cossart, P. (2012). Septins: the fourth component of the cytoskeleton. Nat. Rev. Mol. Cell Biol. *13*, 183–194. .

Nakos, K., Rosenberg, M., and Spiliotis, E.T. (2019). Regulation of microtubule plus end dynamics by septin 9. Cytoskeleton *76*, 83–91. .

Neubauer, K., and Zieger, B. (2017). The Mammalian Septin Interactome. Front Cell Dev Biol *5*, 3. .

Niggli, V. (2003). Microtubule-disruption-induced and chemotactic-peptide-induced migration of human neutrophils: implications for differential sets of signalling pathways. J. Cell Sci. *116*, 813–822. .

Nordenfelt, P., Elliott, H.L., and Springer, T.A. (2016). Coordinated integrin activation by actin-dependent force during T-cell migration. Nat. Commun. *7*, 1–15. .

Odom, T.W., Love, J.C., Wolfe, D.B., Paul, K.E., and Whitesides, G.M. (2002). Improved Pattern Transfer in Soft Lithography Using Composite Stamps. Langmuir *18*, 5314–5320. .

Oh, Y., and Bi, E. (2011). Septin structure and function in yeast and beyond. Trends Cell Biol. *21*, 141–148. .

Overstreet, M.G., Gaylo, A., Angermann, B.R., Hughson, A., Hyun, Y.-M., Lambert, K., Acharya, M., Billroth-Maclurg, A.C., Rosenberg, A.F., Topham, D.J., et al. (2013). Inflammation-induced interstitial migration of effector $CD4^+$ T cells is dependent on integrin αV. Nat. Immunol. *14*, 949–958. .

Paluch, E., Piel, M., Prost, J., Bornens, M., and Sykes, C. (2005). Cortical Actomyosin Breakage Triggers Shape Oscillations in Cells and Cell Fragments. Biophys. J. *89*, 724–733. .

Paul, C.D., Mistriotis, P., and Konstantopoulos, K. (2017). Cancer cell motility: lessons from migration in confined spaces. Nat. Rev. Cancer *17*, 131–140. .

Permana, S., Hisanaga, S.-I., Nagatomo, Y., Iida, J., Hotani, H., and Itoh, T.J. (2005). Truncation of the projection domain of MAP4 (microtubule-associated protein 4) leads to attenuation of microtubule dynamic instability. Cell Struct. Funct. *29*, 147–157. .

Plotnikov, S.V., Sabass, B., Schwarz, U.S., and Waterman, C.M. (2014a). High-resolution traction force microscopy. Methods Cell Biol. *123*, 367–394. .

Plotnikov, S.V., Sabass, B., Schwarz, U.S., and Waterman, C.M. (2014b). High-resolution traction force

microscopy. Methods Cell Biol. *123*, 367–394. .

Ramachandran, S., Kota, P., Ding, F., and Dokholyan, N.V. (2011). Automated minimization of steric clashes in protein structures. Proteins *79*, 261–270. .

Raman, P.S., Paul, C.D., Stroka, K.M., and Konstantopoulos, K. (2013). Probing cell traction forces in confined microenvironments. Lab Chip *13*, 4599–4607. .

Renkawitz, J., and Sixt, M. (2010). Mechanisms of force generation and force transmission during interstitial leukocyte migration. EMBO Rep. *11*, 744–750. .

Renkawitz, J., Schumann, K., Weber, M., Lämmermann, T., Pflicke, H., Piel, M., Polleux, J., Spatz, J.P., and Sixt, M. (2009). Adaptive force transmission in amoeboid cell migration. Nat. Cell Biol. *11*, 1438–1443. .

Renkawitz, J., Kopf, A., Stopp, J., de Vries, I., Driscoll, M.K., Merrin, J., Hauschild, R., Welf, E.S., Danuser, G., Fiolka, R., et al. (2019). Nuclear positioning facilitates amoeboid migration along the path of least resistance. Nature *568*, 546–550. .

Reversat, A., Gaertner, F., Merrin, J., Stopp, J., Tasciyan, S., Aguilera, J., de Vries, I., Hauschild, R., Hons, M., Piel, M., et al. (2020). Cellular locomotion using environmental topography. Nature *582*, 582–585. .

Rhee, S., Jiang, H., Ho, C.-H., and Grinnell, F. (2007). Microtubule function in fibroblast spreading is modulated according to the tension state of cell--matrix interactions. Proceedings of the National Academy of Sciences *104*, 5425–5430. .

Rolli, C.G., Seufferlein, T., Kemkemer, R., and Spatz, J.P. (2010). Impact of tumor cell cytoskeleton organization on invasiveness and migration: a microchannel-based approach. PLoS One *5*, e8726. .

Ruprecht, V., Wieser, S., Callan-Jones, A., Smutny, M., Morita, H., Sako, K., Barone, V., Ritsch-Marte, M., Sixt, M., Voituriez, R., et al. (2015). Cortical contractility triggers a stochastic switch to fast amoeboid cell motility. Cell *160*, 673–685. .

Sadjadi, Z., Zhao, R., Hoth, M., Qu, B., and Rieger, H. (2020). Migration of Cytotoxic T Lymphocytes in 3D Collagen Matrices. Biophys. J. *119*, 2141–2152. .

Salameh, J., Cantaloube, I., Benoit, B., Poüs, C., and Baillet, A. (2021). Cdc42 and its BORG2 and BORG3 effectors control the subcellular localization of septins between actin stress fibers and microtubules. Curr. Biol. https://doi.org/10.1016/j.cub.2021.07.004.

Schmid, H., and Michel, B. (2000). Siloxane Polymers for High-Resolution, High-Accuracy Soft Lithography. Macromolecules *33*, 3042–3049. .

Schmidt, K., and Nichols, B.J. (2004). Functional interdependence between septin and actin cytoskeleton. BMC Cell Biol. *5*, 43. .

Schwede, T., Kopp, J., Guex, N., and Peitsch, M.C. (2003). SWISS-MODEL: An automated protein homology-modeling server. Nucleic Acids Res. *31*, 3381–3385. .

Shakiba, D., Alisafaei, F., Savadipour, A., Rowe, R.A., Liu, Z., Pryse, K.M., Shenoy, V.B., Elson, E.L., and Genin, G.M. (2020). The Balance between Actomyosin Contractility and Microtubule Polymerization Regulates Hierarchical Protrusions That Govern Efficient Fibroblast–Collagen Interactions. ACS Nano *14*, 7868–7879. .

Singh, R.K., Kim, K.K., Khazan, N., Rowswell-Turner, R.B., Laggner, C., Jones, A., Srivastava, P., Hovanesian, V., Lamere, L., Conley, T., et al. (2020). Septins disruption controls tumor growth and enhances efficacy of Herceptin.

Spiliotis, E.T. (2018). Spatial effects − site-specific regulation of actin and microtubule organization by septin GTPases. J. Cell Sci. *131*, jcs207555. .

Spiliotis, E.T., and Nakos, K. (2021). Cellular functions of actin- and microtubule-associated septins. Curr. Biol. *31*, R651–R666. .

Stroka, K.M., Jiang, H., Chen, S.-H., Tong, Z., Wirtz, D., Sun, S.X., and Konstantopoulos, K. (2014). Water Permeation Drives Tumor Cell Migration in Confined Microenvironments. Cell *157*, 611–623. .

Tabdanov, E., Gondarenko, S., Kumari, S., Liapis, A., Dustin, M.L., Sheetz, M.P., Kam, L.C., and Iskratsch, T. (2015). Micropatterning of TCR and LFA-1 ligands reveals complementary effects on cytoskeleton mechanics in T cells. Integr. Biol. *7*, 1272–1284. .

Tabdanov, E.D., Puram, V.V., Win, Z., Alamgir, A., Alford, P.W., and Provenzano, P.P. (2018a). Bimodal sensing of guidance cues in mechanically distinct microenvironments. Nat. Commun. *9*, 4891. .

Tabdanov, E.D., Puram, V., Zhovmer, A., and Provenzano, P.P. (2018b). Microtubule-Actomyosin Mechanical Cooperation during Contact Guidance Sensing. Cell Rep. *25*, 328–338.e5. .

Tabdanov, E.D., Zhovmer, A.S., Puram, V., and Provenzano, P.P. (2020). Engineering Elastic Nano-and Micro-Patterns and Textures for Directed Cell Motility. STAR Protocols.

Tabdanov, E.D., Rodríguez-Merced, N.J., Cartagena-Rivera, A.X., Puram, V.V., Callaway, M.K., Ensminger, E.A., Pomeroy, E.J., Yamamoto, K., Lahr, W.S., Webber, B.R., et al. (2021). Engineering T cells to enhance 3D migration through structurally and mechanically complex tumor microenvironments. Nat. Commun. *12*, 2815. .

Takesono, A., Heasman, S.J., Wojciak-Stothard, B., Garg, R., and Ridley, A.J. (2010). Microtubules regulate migratory polarity through Rho/ROCK signaling in T cells. PLoS One *5*, e8774. .

Théry, M., Pépin, A., Dressaire, E., Chen, Y., and Bornens, M. (2006). Cell distribution of stress fibres in response to the geometry of the adhesive environment. Cell Motil. Cytoskeleton *63*, 341–355. .

Tooley, A.J., Gilden, J., Jacobelli, J., Beemiller, P., Trimble, W.S., Kinoshita, M., and Krummel, M.F. (2009). Amoeboid T lymphocytes require the septin cytoskeleton for cortical integrity and persistent motility. Nat. Cell Biol. *11*, 17–26. .

Tsygankov, D., Bilancia, C.G., Vitriol, E.A., Hahn, K.M., Peifer, M., and Elston, T.C. (2014). CellGeo: a computational platform for the analysis of shape changes in cells with complex geometries. J. Cell Biol. *204*, 443–460. .

Vasiliev, J.M., Gelfand, I.M., Domnina, L.V., Ivanova, O.Y., Komm, S.G., and Olshevskaja, L.V. (1970). Effect of colcemid on the locomotory behaviour of fibroblasts. J. Embryol. Exp. Morphol. *24*, 625–640. .

Vestweber, D. (2015). How leukocytes cross the vascular endothelium. Nat. Rev. Immunol. *15*, 692–704. .

Vignaud, T., Copos, C., Leterrier, C., Toro-Nahuelpan, M., Tseng, Q., Mahamid, J., Blanchoin, L., Mogilner, A., Théry, M., and Kurzawa, L. (2021). Stress fibres are embedded in a contractile cortical network. Nat. Mater. *20*, 410–420. .

Wang, J., and Dokholyan, N.V. (2019). MedusaDock 2.0: Efficient and Accurate Protein–Ligand Docking With Constraints. J. Chem. Inf. Model. *59*, 2509–2515. .

Wiendl, M., Becker, E., Müller, T.M., Voskens, C.J., Neurath, M.F., and Zundler, S. (2021). Targeting Immune Cell Trafficking - Insights From Research Models and Implications for Future IBD Therapy. Front. Immunol. *12*, 656452. .

Wolf, K., Müller, R., Borgmann, S., Bröcker, E.-B., and Friedl, P. (2003). Amoeboid shape change and contact guidance: T-lymphocyte crawling through fibrillar collagen is independent of matrix remodeling by MMPs and other proteases. Blood *102*, 3262–3269. .

Woods, B.L., and Gladfelter, A.S. (2021). The state of the septin cytoskeleton from assembly to function. Curr. Opin. Cell Biol. *68*, 105–112. .

Yadav, S.K., Stojkov, D., Feigelson, S.W., Roncato, F., Simon, H.-U., Yousefi, S., and Alon, R. (2019). Chemokine-triggered microtubule polymerization promotes neutrophil chemotaxis and invasion but not transendothelial migration. J. Leukoc. Biol. *105*, 755–766. .

Yin, S., Biedermannova, L., Vondrasek, J., and Dokholyan, N.V. (2008). MedusaScore: an accurate force field-based scoring function for virtual drug screening. J. Chem. Inf. Model. *48*, 1656–1662. .

Zhovmer, A.S., Manning, A., Smith, C., Hayes, J.B., Burnette, D.T., Wang, J., Cartagena-Rivera, A.X., Dokholyan, N.V., Singh, R.K., and Tabdanov, E.D. (2021). Mechanical Counterbalance of Kinesin and Dynein Motors in a Microtubular Network Regulates Cell Mechanics, 3D Architecture, and Mechanosensing. ACS Nano https://doi.org/10.1021/acsnano.1c04435.